



Physik

*Spatial characterisation of a 36-fold
segmented AGATA detector via a novel
scanning system*

Vom Fachbereich Physik
der Technischen Universität Darmstadt

zur Erlangung des Grades
eines Doktors der Naturwissenschaften

genehmigte Dissertation von
Namita Goel
M. Sc Physics
aus Delhi, Indien

Referent: Prof. Dr. Norbert Pietralla
Koreferent: Prof. Dr. Thomas Aumann
Externer Betreuer: Dr. Jürgen Gerl

Darmstadt 2011

D17

Berichterstatter:

Prof. Dr. Norbert Pietralla

Prof. Dr. Thomas Aumann

Tag der Einreichung:

08.04.2011

Tag der mündlichen Prüfung:

06.06.2011

Contents

List of Figures	7
List of Tables	13
. Acknowledgements	15
. List of papers	17
. Abstract	19
. Kurzfassung	21
1. Introduction	23
2. Fundamentals of γ-ray detection	32
2.1. Photon interactions in matter	32
2.1.1. Photo-electric absorption	33
2.1.2. Compton scattering	34
2.1.3. Pair production	34
2.2. Gamma detectors	35
2.2.1. Scintillation detectors	37
2.2.2. Semiconductor detectors	39
2.2.3. High purity germanium detectors	43
2.3. Pulse shape analysis	44
2.3.1. Pulse formation in germanium detectors	45
2.3.2. PSA in a planar HPGe detector	48
2.3.3. PSA in a coaxial HPGe detector	49
3. Scanner for gamma-ray detectors	52
3.1. Conventional scanning principle	52
3.2. Pulse shape comparison principle	54
3.3. Positron annihilation correlation	54
3.4. Combination of PSC and PAC	56
3.5. Optimisation of scanner performance	57
3.6. Layout of the scanning table	59
3.7. Expected limitations	60

4. Gamma Camera	63
4.1. Principle	63
4.2. Choice of the scintillation-crystal material	64
4.3. Position sensitive photomultiplier tube (PSPMT)	65
4.4. Mechanics of the gamma camera	67
4.5. Electronics and data acquisition system used for the performance tests of the Gamma camera	67
4.6. Anode gain calibration	69
4.7. Experimental set up for position reconstruction studies	70
4.8. Measured light distribution	70
4.9. Position determination	72
4.10. Enhanced Field of view	76
4.11. Resolution and efficiency of the gamma camera	77
4.12. Position calibration using imaging techniques	78
4.12.1. Gamma ray imaging and position calibration	79
4.12.2. Position Calibration for different points in space	83
5. Position response of a planar germanium detector	86
5.1. Experimental setup and the concept of scanning	86
5.2. Gamma ray imaging	88
5.3. Electric field inhomogeneity	90
5.4. T90 distribution plots	90
5.5. Validation measurements with a conventional scanning system	97
5.6. Conclusions	99
6. Position response of a segmented AGATA germanium detector	101
6.1. Physical Details of AGATA	101
6.2. Electrical details	103
6.3. Scan set-up	103
6.4. Intensity maps	104
6.5. Pre-processing of data	106
6.6. Supertrace	107
6.7. Radial distribution of pulses	107
6.8. Pulse shape comparison scan	109
6.9. Image charge asymmetry	112
6.10. Multi Geometry Simulation, MGS	113
6.11. Risetime distribution plots	115
6.12. Effective segmentation	119
6.13. Rise-time behaviour as a function of depth	121
7. Conclusion and Outlook	125
A. Appendix	128
A.1. Electric field in a planar germanium detector	128

A.2. Electric field in a coaxial germanium detector	130
. Erklärung zur Eigenständigkeit	138

List of Figures

1.1.	The schematic diagram of an escape suppressed Ge detector	24
1.2.	Spectra obtained using a ^{137}Cs source for all gamma-rays detected in the germanium detector and for the Compton suppressed spectrum using the shield	24
1.3.	Total photopeak efficiency as a function of the number of detectors . . .	25
1.4.	Doppler Effect	26
1.5.	Schematic diagram (side view cross section) of a cluster of 7 HPGe detectors surrounded by their BGO Compton suppressor.	26
1.6.	Spectra of part of ^{149}Gd in Eurogam Phase I and II.	28
1.7.	Pictorial representation of series of interaction points for a photon entering in a detector volume	28
1.8.	Capability of Doppler correction of PSA	30
1.9.	The diagrammatic representation of the division of the work	31
2.1.	Photon interaction cross-section in Germanium.	32
2.2.	Illustration of the photoelectric effect.	33
2.3.	Illustration of Compton effect.	35
2.4.	Energy resolution of NaI(Tl), CdTe and HPGe detector as a function of gamma ray energy [20].	36
2.5.	Energy spectrum of ^{241}Am obtained with a HPGe and a NaI(Tl) detector [20].	36
2.6.	Energy band structure of an activated scintillator [19].	37
2.7.	Schematic diagram of the interior of a photomultiplier tube.	39
2.8.	Crossed anode wire structure of Hamamatsu H3292 position sensitive photomultiplier tube.	40
2.9.	Representation of donor and acceptor energy levels created in between the band-gap in a n type and p type doped semiconductor material. . .	41
2.10.	Schematic diagram of a pn junction.	42
2.11.	Reverse biased pn junction.	43
2.12.	Planar HPGe detector configuration.	44
2.13.	Coaxial HPGe detector configuration.	45
2.14.	Drift velocity as a function of electric field for electrons and holes [23]. .	46
2.15.	Variation of drift mobility of electron and holes as a function of the impurity concentration in an n-type germanium material at 300 K [24].	46
2.16.	Pulses for a planar germanium detector	48

2.17. Charge pulses for a coaxial detector for three interaction points along the radial line.	49
2.18. Variation in the transient signal amplitude as the distance of the interaction point changes from the segment boundary. The distribution of interaction points in the hit segment is shown schematically in the right part of the figure. The arrow indicates the neighbouring segment. The transient signals in this segment for the corresponding positions (shown in color) are shown (left). The amplitude of the mirror charge is maximum (violet) for the interaction position located closest to the neighbouring segment.	50
2.19. Experimental pulse shapes from an AGATA crystal. The highlighted area shows the positive rising pulse from the segment which host the photon interaction (shown shaded in the right sketch), the other three negative pulses are from neighbouring segments.	51
3.1. The schematic diagram of a conventional scanning system	53
3.2. Schematic diagram showing the pulse shape comparison technique	54
3.3. Schematics of a β^+ decay and positron annihilation	55
3.4. Pulse shape comparison scan of germanium. Pulse shapes recorded for the collimation lines coming inside the coincidence cone of PSD and germanium for position A. Source and PSD moved together by an angle of 90° to be at position B and again a data set of pulse shapes is measured.	56
3.5. Maximum solid angle coverage.	58
3.6. The pile up of charge pulses.	59
3.7. ^{22}Na source between two tungsten shields.	60
3.8. Scanning table with germanium and position sensitive detector facing each other.	60
3.9. Variation of the mean free path in germanium as a function of gamma ray energy.	61
3.10. Sequence of interactions of intermediate energy photons in a HPGe detector.	62
4.1. Spectral response of various scintillators [41].	64
4.2. Crossed anode wire structure of the Hamamatsu R2486 position sensitive photomultiplier tube.	66
4.3. (Top) Block diagram of the electronics employed for reading the 32 anodes of PSPMT. (Bottom) Electronics block diagram showing the trigger gate signal formation for the QDC.	68
4.4. (Top) raw QDC pulse height spectra from the 16 Y anodes. (Bottom) Calibrated pulse height spectra.	70
4.5. Experimental setup for position reconstruction measurements.	71

4.6.	Pattern of the positions where the measurement is done with the collimated source (observe the closer spacing at the edges). The Solid circle indicates the minimum size of photocathode and the dashed circle represents the extended anode grid.	71
4.7.	The charge distribution profile for X and Y anodes for an interaction position close to the center (a) and a position close to the edges of the crystal (b).	72
4.8.	Charge distribution of X anodes (a) and Y anodes (b) for an event at the centre of the photocathode. The shaded distribution in panel (c) represents an event occurring close to the edge of the photocathode. A fit of Gaussian function (dashed line) and the formula of Lerche (solid line) is shown.	73
4.9.	An example showing the position determination using the pattern fitting approach. The measured charge profile is shown in black while the average pattern for the centre is shown in red. (Top) Charge profile for an event near the border of the photocathode. (Bottom) The relative position of the average pattern is varied till it matches the measured charge profile.	75
4.10.	Two dimensional histograms showing reconstructed position variables (x,y) for the scanned positions indicated in Fig. 24. (a) Centroiding approach (b) Gaussian fitting approach (c) Pattern position fitting approach.	76
4.11.	Pictorial representation of an event occurring outside the photocathode surface. The light cone of scintillation still reaches partly the anode grid making it possible to reconstruct these events using the pattern position fitting approach.	77
4.12.	(a) Position resolution on X and Y anodes for a 1mm collimated source placed at the center of the photocathode (b) Spatial resolution (FWHM) measured for X axis positions (black squares) and Y axis positions (red circles).	78
4.13.	The Gamma camera mounted on the scanning mechanics.	80
4.14.	(11 x 11) cm ² steel grid in front of the ²² Na source.	81
4.15.	Setup for the imaging of the grid. NaI(Tl) detectors are placed at sideward angles to register the gammas scattered off the steel grid.	82
4.16.	Image of the grid obtained with the position sensitive detector using the pattern fit algorithm.	82
4.17.	Reconstruction of measured positions by applying two-dimensional functions.	83
4.18.	Multiple planes inside the detector volume. Position calibration was done for several planes.	84
4.19.	Image of the grid when it is rotated by 40°, obtained with the position sensitive detector using the pattern fit algorithm.	85
4.20.	Reconstruction of measured positions by applying two-dimensional functions.	85

5.1. Scanner	87
5.2. Schematic diagram of a planar germanium detector	89
5.3. Coincidence pulse height spectrum of planar germanium detector	89
5.4. Front and side view images of germanium detector for Compton and photopeak events in the pulse height spectrum	89
5.5. Front and side view images reconstructed for photopeak events. The pulses in the respective graphical cuts are shown in the bottom panel of the figure	91
5.6. Front and side view images reconstructed for incomplete charge collection events	92
5.7. Projection of the 2D image	92
5.8. Pictorial representation of the trajectory selection in the front and side view projections of the PSD for a particular interaction position inside the germanium volume.	93
5.9. Graphical representation of the trajectories passing through the germanium volume in two orthogonal directions.	93
5.10. The distribution of Δ^2 values for the comparison of pulses in the selected graphical cuts of side and front view.	94
5.11. The 2D representation of pulses which are in the selected Δ^2 range.	94
5.12. Distribution of pulses along the thickness of the detector.	95
5.13. T90 rise time distribution plot in ns for a slice at half thickness of the detector.	95
5.14. T90 rise time distribution plot in ns for a slice at 1.6 cm away from the central axis of the detector.	96
5.15. T90 rise time distribution plot in ns for a slice at 1.6 cm away from the central axis of the detector in opposite direction as compared to the previous case.	96
5.16. Scanning system at IPHC Strasbourg.	97
5.17. Comparison of charge pulses for same positions inside the HPGe planar obtained with scanning facility at IPHC Strasbourg and GSI.	98
5.18. Scanning system at IPHC Strasbourg.	99
6.1. AGATA array with 180 highly segmented germanium crystals encapsulated in 60 triple clusters	102
6.2. The schematic diagram of a symmetric prototype AGATA crystal and picture of S001 encapsulated symmetric crystal	102
6.3. The schematic representation of the front hexagonal surface, side projection showing the bore, segmentation pattern and the label convention.	103
6.4. Agata S001 detector mounted in the scanning system.	104
6.5. Intensity maps for different rings for full energy photopeak events in individual segments.	105
6.6. Signals of all the 36 segments for a full energy event in segment C4.	106
6.7. Normalised time aligned traces for full energy 511 keV events in a segment.	107

6.8.	Truncated supertrace for an interaction in segment F3.	108
6.9.	Traces for interaction points radially distributed along a trajectory in segment A2.	109
6.10.	Average pulse shapes of the hit segment and a nearest neighbour by demanding different amplitudes of the transient charge signal.	110
6.11.	Truncated supertrace for interactions at 12 mm and 30 mm radius.	111
6.12.	Truncated supertrace for interactions at 28 mm radius for azimuthal angle 30° and 90°.	111
6.13.	Asymmetry between segment A3 and E3.	112
6.14.	The simulated drift velocity of electrons in xz plane.	114
6.15.	The electric field vectors in S001 crystal.	114
6.16.	Schematic representation of the selected interaction points in ring 1, 2, 3 and 4.	115
6.17.	T30 and T90 curves for two segments F1 and F2 corresponding to rings 1 and 2 respectively.	116
6.18.	T30 and T90 values for two segments F3 and F4 corresponding to rings 3 and 4 respectively.	117
6.19.	T30 and T90 rise time distribution for segment F3 in ring 2.	118
6.20.	The intensity distribution plots for segment F1, F2 and F3.	119
6.21.	The intensity distribution plot for segment F3, F2 and F1 and segmentation pattern given by MGS.	120
6.22.	Δ^2 values in ring 2.	121
6.23.	Experimental and simulated T90 distribution plots for section F, from the front of the detector till ring 3.	122
6.24.	Difference in the theoretical and experimental risetime values.	122
6.25.	Difference in the theoretical and experimental risetime values.	123

List of Tables

1.1. Arrays of segmented detectors.	29
4.1. Properties of scintillator material useful for gamma ray detection at 511 keV.	65
6.1. Parameters used for the S001 AGATA geometry for the MGS simulation.	113
6.2. Two different sets of impurity charge concentration parameters used for S001 AGATA geometry for MGS simulation.	123

Acknowledgements

This work would not have been imaginable without the help and support of many people who also might not be mentioned directly by their names at this place by me. I would like to express my deep and sincere gratitude to Dr. Jürgen Gerl for the supervision of my work. His broad knowledge, help and suggestions were highly important for me and absolutely crucial in bringing this thesis to completion.

I would like to thank Prof. Dr. Norbert Pietralla who kindly accepted me in his group in Institut für Kernphysik (IKP) at Technische Universität Darmstadt. His support throughout the period of the thesis is highly appreciated.

Further on I would like to thank my second supervisor Dr. Cesar Domingo Pardo for his continuous support, numerous discussions, and fruitful suggestions.

I am very grateful to my colleagues Dr. Tobias Engert, Tobias Habermann and Samuel Lago for their invaluable help in many stages of the thesis. The extensive discussions and suggestions given by them during the writing phase were extremely helpful. In addition their friendly behaviour provided a very nice and comfortable working environment. Furthermore the support of all the members of the gamma spectroscopy group at GSI is unforgettable.

I wish my warm thanks to all my friends who have always been there to encourage me. Finally I would like to express my deep gratitude to my parents and brother for their invaluable support, love and understanding.

Darmstadt, April 2011
Namita Goel

List of papers

This thesis is based on the following papers:

1. N. Goel, C. Domingo-Pardo, T. Engert, J. Gerl, I. Kojouharov, N. Pietralla and H. Schaffner, “*Spatial calibration via imaging techniques of a novel scanning system for the pulse shape characterisation of position sensitive HPGe detectors*”, Nuclear Instruments and Methods in Physics Research A, Jan 2011, doi:10.1016/j.nima.2011.01.146.
2. N. Goel, C. Domingo-Pardo, T. Engert, J. Gerl, I. Kojouharov, N. Pietralla and H. Schaffner, “*Study of planar germanium detector response using the γ -ray imaging techniques*”, submitted to NIM A, December 2010.
3. N. Goel, T. Habermann, C. Domingo-Pardo, T. Engert, J. Gerl, I. Kojouharov, J. Maruhn, N. Pietralla, H. Schaffner, “*Characterisation of a symmetric AGATA detector using a novel scanning system*”, in preparation.
4. C. Domingo-Pardo, N. Goel, T. Engert, J. Gerl, I. Kojouharov and H. Schaffner, “*A novel method for the pulse-shape depiction of position sensitive semiconductor γ -ray detectors Part I: Characterization tests with a non-segmented planar detector*”, submitted to NIM A, November 2010.
5. C. Domingo-Pardo, N. Goel, T. Engert, J. Gerl, I. Kojouharov and H. Schaffner, “*A position sensitive γ -ray scintillator detector with enhanced resolution, linearity and field of view*”, IEEE Transactions on Medical Imaging, vol. 28, Dec 2009.

Patent

An European patent has been filed in February 2011.

Title: *Gamma Ray Imaging Device*

Patent number: EP11152965.7

Further papers with the author's contribution:

1. N. Al-Dahan et. al., “*Beyond the $N=126$ Closed Neutron Shell: Isomeric States in ^{208}Hg and ^{209}Tl* ”, Physical Review Letters, Dec. 2009.
2. R. Wadsworth et. al., “*The Northwest Frontier: Spectroscopy of NZ Nuclei Below Mass 100*”, Acta Physica Polonica B40, pp. 611-620, 2009.
3. N. Al-Dahan et. al., “*Isomeric States in ^{208}Hg and ^{209}Tl Populated in Fragmentation of ^{208}U* ”, Acta Physica Polonica B40, pp. 871-874, 2009.

4. A. M. Denis Bacelar et. al., “*Angular Momentum Population in Fragmentation Reactions*”, Acta Physica Polonica B40, pp. 889-892, 2009.
5. T. S. Brocketal et. al., “*Observation of a new high-spin isomer in ^{94}Pd* ”, Physics Review C, vol. 82, issue 6, 2010.
6. A. Jungclaus et. al., “*Evidence for reduced collectivity around the neutron mid-shell in the stable even-mass Sn isotopes from new lifetime measurements*”, Physics Letters B, vol. 695, Issues 1-4, pp. 110-114, Jan 2011.

Abstract

The core principle of segmented gamma-tracking germanium detector arrays like AGATA and GRETA, that will be used in future for 4π gamma detection, is the application of pulse shape analysis (PSA). The 3D position sensitivity of the HPGe detectors is based on differences in the shape of the charge pulses associated with different interaction points inside the whole volume. It is therefore necessary for this analysis to have a data base containing pulses for all the interaction points inside the detector volume. A full 3D scanning of the detectors, which experimentally determines pulse shapes for each position inside the active volume, is therefore needed. In this thesis, a novel scanning system is presented to determine the HPGe detector pulse shapes as a function of the γ -ray interaction position inside the detector. The device is based on a pulse shape comparison scan (PSCS) and the positron annihilation correlation (PAC) method which makes it about 100 times faster than the conventional coincidence based scanners.

The performance and efficiency of the system is superior because of using a position sensitive detector (PSD)/gamma camera. It consists of a LYSO scintillating crystal optically coupled to a position sensitive photomultiplier tube. The individual multi-anode readout (IMAR) approach is used to achieve a spatial resolution of ≈ 1 mm and to optimize its field of view to ≈ 28 cm². A Compton scattering imaging technique is implemented to perform an accurate position calibration of the gamma camera. The employment of PSD yields an added advantage of imaging capability which allows to study e.g. the details of the inner structure of HPGe detectors and electric field anisotropy effects.

The position response of a planar HPGe detector is obtained using the apparatus and the risetime distribution plots are compared with those obtained via a conventional scanning system. However, to validate the aforementioned scanning principle, an AGATA symmetric detector is tested. The risetime values are measured as a function of the interaction position in both the coaxial and quasi-planar region of the detector. Furthermore, the Multi Geometry Simulation (MGS) code is used to generate theoretical distribution plots for comparison. The transition in charge carrier transport behaviour as a function of the depth is studied for the region of the complex electric field. Systematic deviations between simulation and measurement are observed for the critical front part of the AGATA detector. They are interpolated as due to a non-linear impurity concentration profile of the germanium crystal, asking for rigorous scanning of all detectors in the future.

Kurzfassung

Pulsformanalyse spielt eine wesentliche Rolle für die Funktionsweise von kommenden Detektorarrays für Gammaspektroskopie (AGATA, GRETA). Durch Segmentierung der einzelnen Kristalle aus hochreinem Germanium (HPGe) wird eine Ortsauflösung entsprechend der Segmentgrösse erreicht. Der eindeutige Zusammenhang zwischen dem Wechselwirkungsort im Detektor und der Signalform erlaubt, durch Pulsformanalyse die Ortsauflösung deutlich zu verbessern. Voraussetzung für PSA Algorithmen ist die genaue Kenntnis der Pulsformen im gesamten Detektorvolumen. Zu diesem Zweck wurde ein neuartiges Scansystem zur Bestimmung von Pulsformen als Funktion des Wechselwirkungsortes in HPGe Detektoren entwickelt und implementiert. Der Apparat basiert auf der Kombination von PSCS (pulse shape comparison scan) und PAC (positron annihilation correlation), wodurch die Methode ca. 100-mal schneller ist als herkömmliche Systeme.

Durch den Einsatz eines positionsempfindlichen Detektors konnte die Effizienz entscheidend verbessert werden. Dieser besteht aus einem LYSO Szintillatorkristall, optisch gekoppelt an eine positionssensitive Photomultiplier-Röhre. Es konnte eine Ortsauflösung von $\approx 1\text{mm}$ erreicht werden und das effektive Messfeld erstreckt sich über $\approx 19\text{cm}^2$.

Zuerst wurde das Verfahren an einem planaren HPGe Detektor angewandt und die Ergebnisse mit denen eines konventionellen Scan-Verfahren verglichen. Zur Validierung wurde das neuartige Scan-Prinzip außerdem an einem symmetrischen AGATA Kristall angewandt. Die Anstiegszeiten der Signale als Funktion des Wechselwirkungsortes wurden in verschiedenen Regionen des Detektors vermessen. Ausserdem wurde das Simulationspaket MGS (Multi Geometry Simulation) benutzt, um die gemessenen Werte mit den Ergebnissen der Simulation zu vergleichen. Vor allem wurde der Übergang vom koaxialen zum quasi-planaren Bereich des Detektors anhand der Anstiegszeiten untersucht. In diesem Bereich wurden systematische Abweichungen beobachtet. Diese wurden auf nicht-lineare Verteilungen der Verunreinigungskonzentration des Ge-Kristalls zurück geführt und machen eine rigorose Vermessung aller AGATA Detektoren notwendig.

1. Introduction

The nucleus is a quantum mechanical system of nucleons with various excitation modes. The latter are achieved by a variety of reaction techniques, for example, fragmentation, deep inelastic and fusion evaporation reactions. The decay of nuclei from a finite excitation energy state to the ground state is characterised by the emission of a certain number of gamma-rays. These gamma-rays can be detected and provide information about the nuclear energy levels [1, 2, 3]. The energy and intensity of the emitted gamma-quanta determine the position of the levels in the level scheme of a nucleus. Furthermore the knowledge of emission times of the photons provide an indication of the life time of levels. Electromagnetic properties like spin, magnetic moments, quadrupole moments are explored by studying the angular distributions and correlations of the emitted gamma quanta. The study of nuclear excitations via high precision gamma-ray spectroscopy is a powerful tool in nuclear physics to study the most exciting features of the nucleus.

The emission of photons from the nuclear level of interest takes place in cascades. These gamma-rays can have very similar energies in addition to the fact that the states of interest can be very weakly populated, overwhelmed by a huge background of unwanted gamma-rays produced in the same nuclear reaction. In order to isolate the cascades of interest, the energy peaks in the spectrum should stand above the background and the number of counts in the peak must be statistically significant. The gamma detectors thus have the requirement [4] of superior energy resolution and photopeak efficiency to build unambiguous nuclear level schemes.

A revolution in the field of gamma-ray spectroscopy came with the introduction of high energy resolution germanium (Ge) semiconductor materials [5] in the early 1960s. They provide the best compromise between energy resolution (2 keV for 1 MeV gamma-rays) and efficiency in the energy range 0.1 MeV - 20 MeV among other available detection materials. Nevertheless the efficiency achieved with these detectors is still limited. Even with large germanium detectors of about 7 cm diameter and 8 cm length, only 20% of the 1 MeV photons deposit their full energy in the active volume. In the remaining cases, the photons escape the detector after Compton scattering. This results in a significant Compton background in the spectra at lower energies. The ratio of full energy events to the Compton scattered events is quantified as peak-to-total ratio. The peak-to-total ratio and hence the spectrum quality can be improved by surrounding the germanium detector with secondary detectors acting as anti-coincidence suppression shields. The purpose of these shields is to detect the gamma-rays scattered out of the germanium and to reject the coincident events between them and germanium. The combination of germanium and shield is termed as escape-suppressed spectrometer

(ESS), [6]. The schematic diagram of an ESS is shown in Fig. 1.1. The improvement in the spectrum quality using ESS is demonstrated in Fig. 1.2.

Furthermore, if many gamma-rays are emitted in an event, e.g. up to 30, called as multiplicity of an event, it is needed to detect each one of them in separate detectors to avoid losing information on single gamma-ray energy. Therefore the detection system should consist of an array of detectors to achieve the required high granularity. The operation of multiple gamma detectors in coincidence mode made feasible the identification of gamma-rays belonging to the same cascade from one event through their time correlation. The latter is done by extracting a timing signal from each detector in coincidence and applying fast electronics.

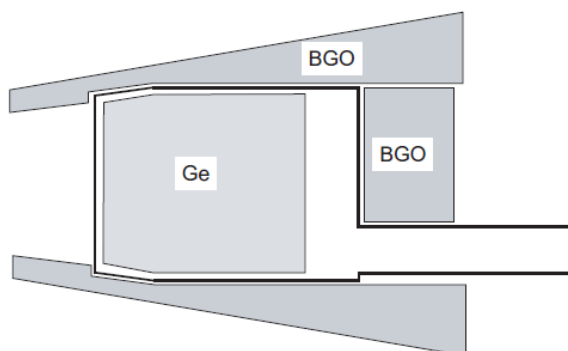


Figure 1.1.: The schematic diagram of an escape suppressed Ge detector [7].

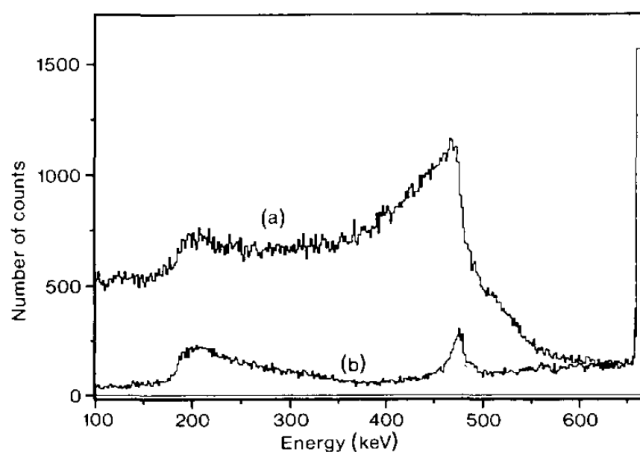


Figure 1.2.: Energy spectra of a ^{137}Cs source, (a) for all the gamma-rays detected in the Ge detector, (b) the Compton suppressed spectrum [8].

The very first high energy resolution array, called the escape suppressed spectrometer array (TESSA0) [8] was built in 1980 by the Niels Bohr Institute and Liverpool University collaboration. It consisted of 5 lithium drifted germanium (Ge(Li)) detectors

surrounded by Thallium doped sodium iodide, (NaI(Tl)) Compton suppressing scintillating shields.

During the last two decades, there has been an unprecedented development in the field of germanium detector arrays which is driven both by the amazing achievements in nuclear physics due to these arrays and technological advancements in detector development. The NaI(Tl) suppression shields were replaced by denser scintillators for example, bismuth germanate (BGO). The size of the suppression shield could be decreased which provided more space and the possibility of increasing the number of detectors around the target. Lithium drifted germanium detectors were replaced by high purity germanium (HPGe) detectors. These detectors have faster production process, better energy resolution and the possibility of manufacturing in large sizes. After the advent of BGO suppressors, a vast variety of arrays, for example TESSA3(UK), HERA(USA), OSIRIS(Germany), GASP(Italy), Eurogam(UK), GAMMASPHERE(USA) [9] were constructed around the world, having photopeak efficiencies of $\approx 0.5\%$ - 1% . The reader is encouraged to read the review articles [6, 7, 10] which give an overview of the developments in gamma-ray detector arrays.

The use of multiple (15-30) HPGe detectors in these arrays increased the coincidence efficiency and the escape suppression shields enhanced the peak to total ratio significantly to $\approx 50\%$.

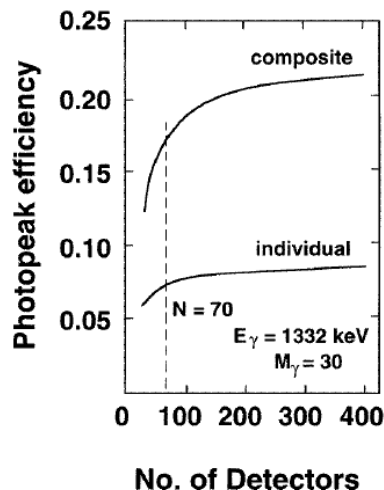


Figure 1.3.: The total photopeak efficiency as a function of the number of detectors in an individual Ge crystals based array and a Composite Ge detector array [10].

The designs of all the aforementioned arrays are based on close packing of large volume escape suppressed Ge crystals. The total photopeak efficiency is limited by the size of the detectors, the effective solid angle coverage by germanium due to the presence of individual detector shields and cost. Figure 1.3 shows the efficiency as a function of the number of detectors. The efficiency increases as expected but it reaches a

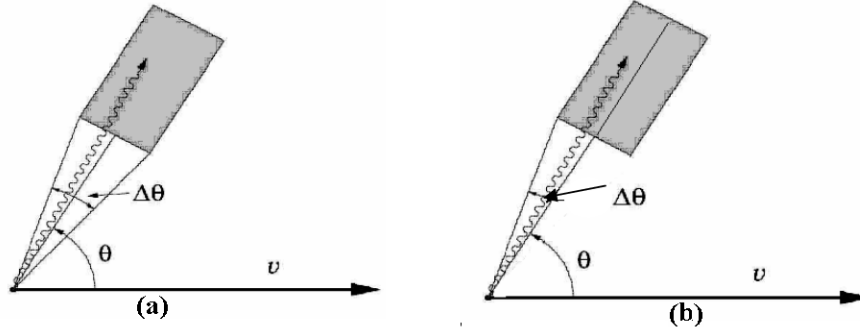


Figure 1.4.: Solid angle ($\Delta\theta$) subtended by a segmented Ge detector (b) is smaller than that subtended by a single crystal (a).

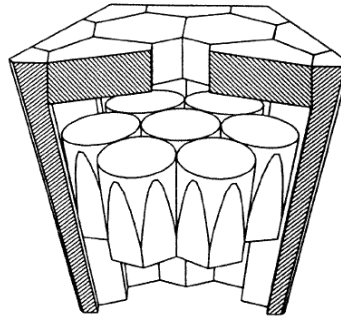


Figure 1.5.: Schematic diagram (side view cross section) of a cluster of 7 HPGe detectors surrounded by their BGO Compton suppressor [7].

saturation value for ≈ 100 detectors. A further limitation of the conventional arrays is the Doppler broadening of the spectral lines that occurs in the experiments where the gamma-ray emitting nucleus has a large velocity during the decay, [11]. The Doppler broadening in the energy resolution for relativistic beams is directly proportional to sine of the angle θ made by the velocity vector of the beam with the axis of the detector and also to the solid angle $\Delta\theta$ subtended by the detector at the position of the gamma emitting nucleus,

$$\frac{\Delta E}{E} \propto \sin \theta \Delta\theta \quad (1.1)$$

The Doppler shifted energies can be corrected if the emission direction with respect to the velocity vector is known. For conventional arrays this precision is limited by the large size of the individual detector as shown in Fig. 1.4(a). Therefore even though the large detectors are closely packed to achieve high photopeak efficiency, the spectrum quality still has the scope to be improved for high velocity photons. Ideally, large detectors with high granularity are needed, which will decrease the solid angle

subtended by individual detectors at the target position and the Doppler broadening in energy resolution, 1.4(b).

The next phase of gamma arrays consisted of composite detectors, for example, EUROBALL [12] and Eurogam II [10]. The aim was to have an ultimate array with nearly 4π solid angle coverage around the target. They consist of approximately 100 composite or segmented HPGe detectors, increasing the granularity of the arrays, having a photo-peak efficiency of the order of 10% (Fig. 1.3) and a peak-to-total ratio of the order of 50% for a gamma-ray energy of 1.3 MeV. The composite germanium detectors used in EUROBALL, are Clusters of germanium crystals in a tight geometry surrounded by common BGO Compton suppression shields, (Fig. 1.5). Using this arrangement, the Compton scattered events between the adjacent segments are reconstructed. The full energy is obtained by summing the energies deposited in adjacent crystals, which is called add-back mode of operation. In this way a large detector is created which has high photopeak efficiency, resolution and granularity as compared to conventional arrays using the same number of detectors. The improvement in the energy resolution in the Eurogam phase II array consisting of Clover composite detectors as compared to the Eurogam phase I array having 45 escape suppressed Ge detectors is seen in Fig. 1.6. In Clover geometry, four germanium crystals are packed in a leaf like configuration.

Unfortunately, for high multiplicity events, if several gamma-rays interact in the same cluster of detectors, the advantage offered by the possibility of adding-back the energies from the neighbouring detectors diminishes since discrimination between the Compton interactions induced by one single incident gamma-ray and the interactions produced by different incident gamma-ray in the same cluster is not possible. Therefore, the add-back procedure will lead to a wrong summing of the energies of different incident gamma-rays and hence to a degraded photopeak efficiency and peak-to-total ratio. The suppression shields also reject a large portion of the gamma-rays.

The nuclear structure physics that has been done in the last decade is attributed to the spark in detector developments. However, the escape suppressed spectrometers have reached their ultimate limit and there is a need for new ideas for the next generation gamma arrays. The recent advances in crystal segmentation technology and digital signal processing, make possible the operation of large volume germanium detectors in a 3D position sensitive mode. The new generation of 4π arrays for high precision gamma-ray spectroscopy will consist of high-fold segmented germanium crystals [17], [30]. Table 1.1 lists arrays of segmented Ge detectors that are constructed in Europe and USA. AGATA and Greta are the first arrays with not only horizontal segmentation like their predecessors but also with segmentation in depth. These arrays are based on the concepts of pulse shape analysis (PSA) [32] and gamma-ray tracking [31].

The goal of pulse shape analysis and gamma-ray tracking is the reconstruction of paths taken by the photons interacting with a detector on an event-by-event basis. For gamma-ray energies typical for nuclear physics (≈ 100 keV - 2 MeV), the tracks will consist of several Compton scattering points and the final photo-absorption. The

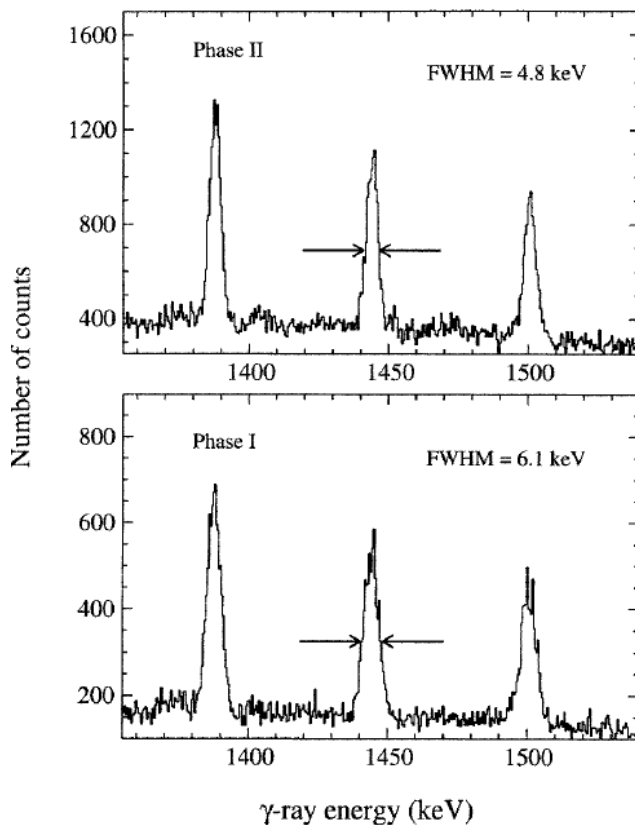


Figure 1.6.: Spectra of ^{149}Gd in the Eurogam Phase I and II. The reaction was: $^{30}\text{Si} + ^{124}\text{Sn} \rightarrow ^{149}\text{Gd} + 5\text{n}$, at $E_{\text{beam}} = 158\text{MeV}$, $\beta_{\text{recoil}} = 2.1\%$. The resolution of the 1450 keV transition reduces from 6.1 keV in Eurogam I to 4.8 keV in Eurogam II [10].

series of Compton interactions constitute a track of point-like energy deposits, as shown in Fig. 1.7.

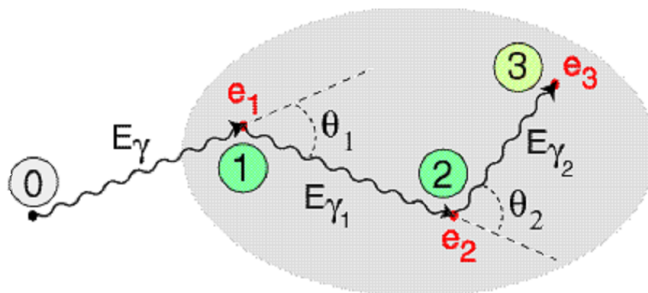


Figure 1.7.: Pictorial representation of series of interaction points for a photon entering in a detector volume.

The task of determining the track of a gamma-ray is divided into two distinct problems. The first is to find the points within the detector where the energy has been deposited. This is accomplished by PSA algorithms. These algorithms utilize the in-

Table 1.1.: Arrays of segmented detectors.

Name	No. of crystals	Shape	No. of segments/crystal	Status
EXOGRAM [13]	64	Square	4 x 1	Operational
TIGRESS[14]	48	Square	4 x 2	Operational
MINIBALL[15]	24	Reg.hexagon	6 x 1	Operational
SeGA[10]	18	Cylinder	4 x 8	Operational
GRETA[16]	120	Irr. hexagons	6 x 6	Prototype
AGATA[17]	120	Irr. hexagons	6 x 6	Prototype

formation gained from the pulse shapes of the hit segment and also the mirror charge signals. The latter are the signals seen in the neighbouring segments of the net charge collecting segment. This gives a fingerprint of the position in three dimensions. The second problem is to determine the order of the points found by PSA, and in more complex cases with many interaction photons to find which interactions belong to the track of a given photon and which do not. The tracking algorithms are based on the Compton scattering formula, due to its ability to relate the geometrical locations of the interactions to the deposited energy. If the deposited energy and the coordinates of each interaction point are known, the path of the gamma-ray photon inside the detector (or adjacent detectors) can be traced. The high granularity of segmented detectors will already substantially reduce the value of solid angle, $\Delta\theta$ subtended at the target position. The key feature of using segmented detectors with an application of gamma-ray tracking and pulse shape analysis is to determine the emission direction of all detected gamma-quanta with an opening angle of the order of 1-2 degrees. The effective granularity is thus even smaller than the size of individual segment. This will allow to perform a finer Doppler correction for the shift in the energy for relativistic beams. It is predicted that an energy resolution better than 2 keV can be achieved for gamma-rays emitted by nuclei at velocities up to $v/c = 50\%$.

The accuracy of gamma-ray tracking algorithms depends on the precision with which the interaction points and the corresponding energy deposited are determined in the detectors. The pulse shapes for gamma interaction events in a detector are compared to a database of measured pulse shapes from the same detector. This database contains the signal shapes for corresponding interaction positions.

It can be experimentally obtained by placing a collimated source in front of the detector which defines the (x,y) coordinates of the interaction points. In order to find the depth, the detector is surrounded by secondary detectors which are in coincidence with it for the Compton scattered events out of the volume of the detector. This is an extremely lengthy measurement to be performed on all the detectors of the array. At the moment, the pulse shape analysis on segmented germanium detector arrays is done using a database of calculated pulse shapes. Using the parameterisations of the electric field and drift velocity of charge carriers, the signal shapes for charges in each point of the detector is calculated. For example, the PSA is applied to a triple cluster of 36 fold segmented AGATA detectors in an in-beam test using the calculated

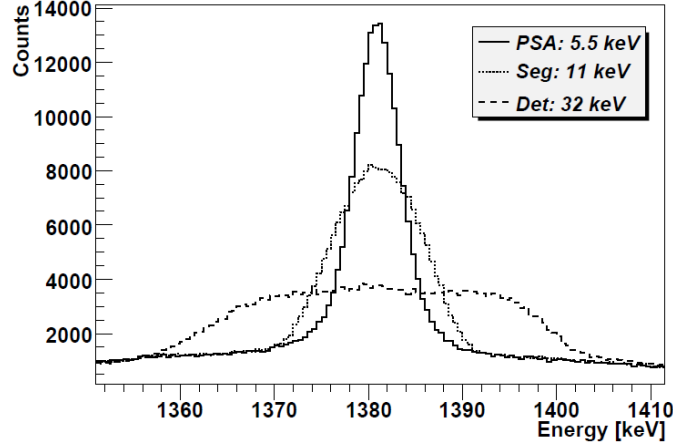


Figure 1.8.: Capability of Doppler correction of PSA: comparison between the energy resolution obtainable using as first interaction point the center of the 36 fold segmented AGATA detector, the center of the firing segment and the position given by PSA, [18]

pulse shapes obtained via multi geometry simulation (MGS). The Doppler correction is performed assuming 3 different positions for the first interaction, namely the center of the detector, the center of the firing segment and the position of interaction given by PSA. The comparison between the energy resolution obtainable for the three cases is shown in Fig. 1.8.

However, there are some regions in the detector where the electric field is not calculated accurately, producing inaccurate pulse shapes. Also the assignment of positions is based on the assumption that the crystal is perfectly centered in its respective cryostat which might not be the case. The effect of the electronics, the crosstalk between the segments and several other features have to be added in the simulation model to develop a realistic database. To gain confidence in the electric field calculations, the theoretical pulse shapes need to be validated with the real pulse shapes taken experimentally for several interaction points in the detector. A full 3D characterisation of detectors is thus to be performed before using them in arrays. The proposed device must be accurate, time and cost efficient.

In this work, a novel technique to measure the high purity germanium detector (HPGe) pulse shapes as a function of gamma-ray interaction position inside the detector volume is presented. The technique is implemented in a system developed for the scanning of germanium detectors. This device is considerably faster as compared to the conventional coincidence based detector scanners.

After giving an introduction to the subject of gamma ray detection, gamma ray tracking and pulse shape analysis in chapter 2, the principle of scanner operation and the associated mechanics are explained in chapter 3. A position sensitive detector is developed and is employed in the device. It is in fact one of the key element of the whole apparatus. The various tests that were performed during the developmental stages are presented in chapter 4. In chapter 5, the position response of an n type planar HPGe detector acquired with the device is shown. The results are compared with

those obtained from a coincidence based scanner. Although the system is devoted to the pulse shape characterisation of HPGe detectors, in addition, it has an inherent advantage of having imaging capability. The imaging application allows to study the details of the inner structure of the detector, the exact location and orientation of the crystal inside the cryostat and also the electric field anisotropy effects. These are some of the parameters which are critical to build a database of charge signal shapes. The spatial response of a 36-fold segmented AGATA prototype detector is successfully obtained with the new scanning approach and is reported in chapter 6. The experimentally measured pulse shapes are compared with the theoretical shapes obtained using multi-geometry simulation (MGS).

Figure 1.9 represents diagrammatically the advancement of the work from basic principles of gamma detection till the operational phase of the scanning device.

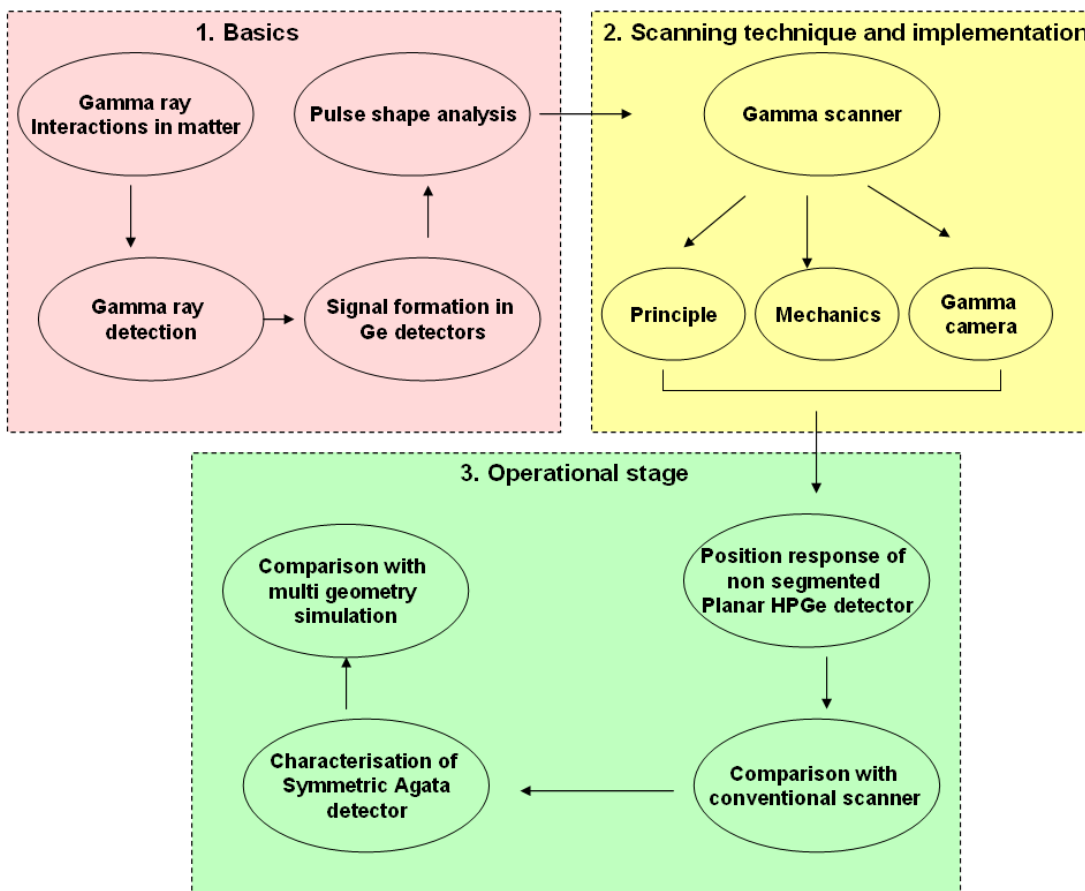


Figure 1.9.: The diagrammatic representation of the division of the work.

2. Fundamentals of γ -ray detection

The work presented in this thesis involves extensive working with semiconductor and scintillator detectors. The basics of photon interaction with matter and the general working principles of γ -ray detectors is therefore described in the following. Common methods for the determination of the γ -ray hit location using a position sensitive photomultiplier tube (PSPMT) are presented.

2.1. Photon interactions in matter

In general, γ rays have different interaction mechanisms in matter. Three possibilities play a major role in radiation measurements namely, photoelectric absorption, Compton scattering, and pair production. The relative probability of the possible interactions in germanium as a function of γ -ray energy is presented in Fig. 2.1. For γ -rays in the energy range 100 keV - 2 MeV, Compton scattering and photoelectric absorption are the two dominant modes of interaction. The majority of interactions consist of a series of scattering followed by final photoelectric absorption. These mechanisms are described in detail in [19], however for the completeness of the work, in the following sections, they are briefly discussed.

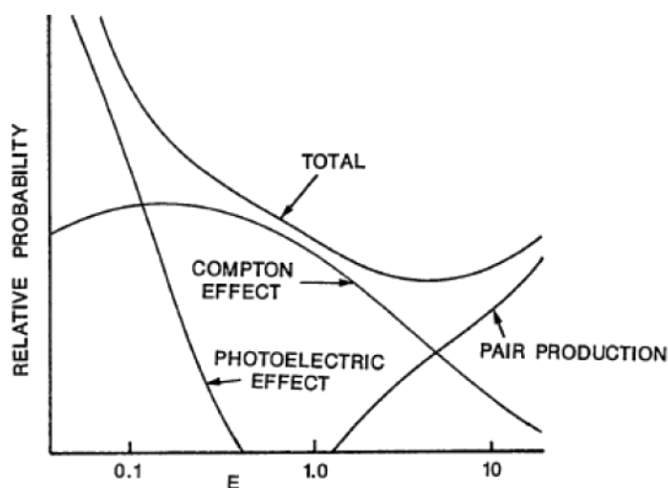


Figure 2.1.: Photon interaction cross-section in Germanium.

2.1.1. Photo-electric absorption

In the photoelectric absorption process, an incoming gamma ray completely disappears after it underwent an interaction with an absorber atom (see Fig. 2.2). In its place, an energetic photoelectron is ejected by the atom from one of its bound shells. Since the electrons are initially bound, a part of the photon energy is spent to free the electron and the rest is transferred to the electron as kinetic energy. If E_{bind} is the binding energy and $h\nu$ is the energy of the photon, then the photoelectron appears with an energy E_{kin} given by

$$E_{kin} = h\nu - E_{bind}. \quad (2.1)$$

For conservation of the momentum, the nucleus takes over most of the momentum. Therefore, the γ -quanta are predominantly absorbed by K and L electrons. Part of the binding energy E_{bind} is transferred to X-rays emitted from the atom when the vacancy left by the first photoelectron is filled by a less-bound electron. For gamma rays interacting only photo-electrically with the detector, no tracking is needed, since the whole energy of the photon is released at one position. However, the interaction position has to be determined. The estimation of the initial direction of the gamma ray is possible only by assuming an emission from a known source.

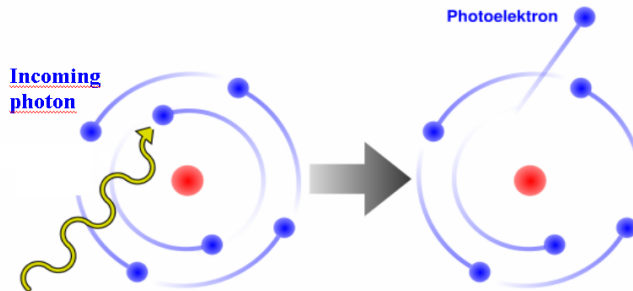


Figure 2.2.: Illustration of the photoelectric effect.

For gamma rays of relatively low energy, the photoelectric process is the predominant mode of interaction. The process is also enhanced for absorber materials of high atomic number Z . A rough approximation of the relation between the photoelectric cross-section σ , E_γ (energy of photon) and Z is

$$\sigma \propto const. \times \frac{Z^n}{E_\gamma^3} \quad (2.2)$$

where the exponent n varies between 4 and 5 over the gamma ray energy region of interest.

2.1.2. Compton scattering

Compton scattering is the dominant mode of interaction for photons in germanium for energies between ≈ 150 keV and 5-6 MeV. It is an inelastic scattering process in which the incoming gamma ray is scattered by an angle θ with respect to its original direction. A part of the energy of the photon is transferred to an electron, which is then known as a recoil electron. Because all angles of scattering are possible, the energy transferred to the electron can vary from zero to a large fraction of the gamma ray energy. By applying the conservation of energy and momentum, a relation between the energy transfer and the scattering angle for any interaction can be derived. Using the symbols defined in Fig. 2.3, it can be shown [19] that

$$h\nu' = \frac{h\nu}{1 + \frac{h\nu(1-\cos\theta)}{m_0c^2}} \quad (2.3)$$

where m_0c^2 is the rest mass energy of the electron (0.511 MeV). The energy transfer to the electron increases with the scattering angle θ , and is largest in the case of backscattering ($\theta = 180^\circ$). A photon undergoes Compton scattering several times until its energy is reduced sufficiently for photo-absorption to become the more likely interaction. The angular distribution of scattered gamma rays is predicted by the Klein-Nishina formula for the differential scattering cross section $d\sigma/d\Omega$:

$$\frac{d\sigma}{d\Omega} = r_0^2 \left[\frac{1}{1 + \alpha(1 - \cos\theta)} \right]^3 \left[\frac{1 + \cos^2\theta}{2} \right] \left[1 + \frac{\alpha^2(1 - \cos\theta)^2}{(1 + \cos^2\theta)(1 + \alpha(1 - \cos\theta))} \right] \quad (2.4)$$

where $\alpha = h\nu/m_0c^2$ and r_0 is the classical electron radius. Compton scattering plays an important role in γ -ray tracking. Using the Compton scattering and Klein-Nishina formulae, it is possible to reconstruct the scattering sequence of an incident γ -ray if all the positions and energies of the interaction are known. Moreover, using the Compton scattering formula it is possible to predict the direction of an incident γ -ray up to the surface of the cone made by the angle of the first Compton interaction.

2.1.3. Pair production

Although the production of electron-positron pairs is possible in the electrostatic field of the nuclei for γ -rays with energies exceeding twice the rest mass of the electron (1.02 MeV), a significant cross section for this interaction mechanism takes place only above 4-5 MeV in germanium. In pair production, the energy of the γ -ray is used to create an $e^+ - e^-$ pair, the remaining momentum is transferred to the nucleus. After losing its energy in the detector material through ionisation, the positron annihilates

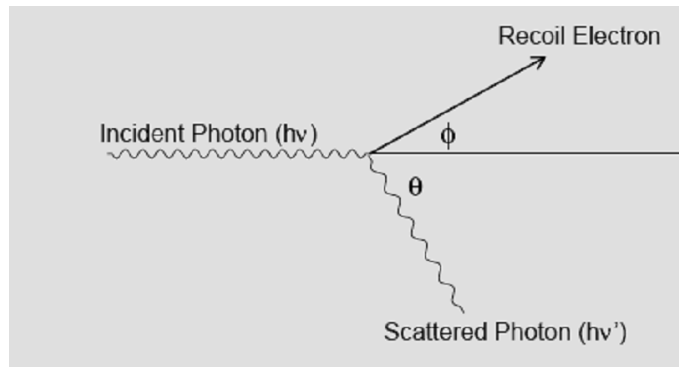


Figure 2.3.: Illustration of Compton effect.

with another electron of the material, giving rise to two 511 keV annihilation gamma-quanta.

2.2. Gamma detectors

When a photon enters the sensitive volume of a gamma-ray detector, it undergoes interaction through one of the above mentioned mechanisms. The form in which the photon energy appears is converted in an electric signal depends on the type of detector. In majority of detectors, the net result of the primary γ -ray interaction is the creation of an electric charge within the detector volume. This charge ionises and excites the detector atoms.

Gaseous detectors are designed to directly collect the electrons to form an electric current signal. Another category of detectors, namely, solid state detectors are classified either as scintillators or as semiconductor detectors. In the case of scintillators, the photon energy is collected indirectly. The electrons emitted by photon interactions in the scintillator crystal, interact with the crystal and emit photons in the visible frequency region (see section 2.2.1). These lower energy photons are subsequently collected by light detectors. The operating principle of semiconductor detectors is analogous to gas ionization devices. Instead of gas, the interacting medium is now a solid semiconductor material. The passage of ionising radiation creates electron hole pairs, which are then collected in the electrodes by an externally applied electric field. The energy resolution of a detector is inversely proportional to the square root of the number of charge carriers produced in an interaction. It is desirable to have a large number of charge carriers to reduce the statistical fluctuations and hence an improved resolution. Solid detection medium is of great advantage for high resolution gamma ray spectroscopy. The detector dimensions can be kept much smaller than the equivalent gas filled detector because solid densities are about 1000 times greater than for a gas. Moreover, the average energy required to create an electron-hole pair is about 10 times smaller than that required for gas ionization, thus providing much better energy resolution.

Scintillator detectors have good detection efficiency but they require higher energy of about 100 eV to produce charge carriers. On the contrary semiconductor detectors need much lower energy (≈ 3 eV) to produce charge carriers. Figure 2.4 shows the comparison of energy resolution of NaI(Tl) scintillator with CdTe and HPGe semiconductor detectors, as a function energy. The resolution of HPGe detectors is a factor of 30-50 better than the scintillators. The energy spectrum of a ^{241}Am source obtained with a NaI(Tl) scintillator detector and a HPGe detector shown in Fig. 2.5 demonstrates that germanium detectors are a better choice for high resolution spectroscopy.

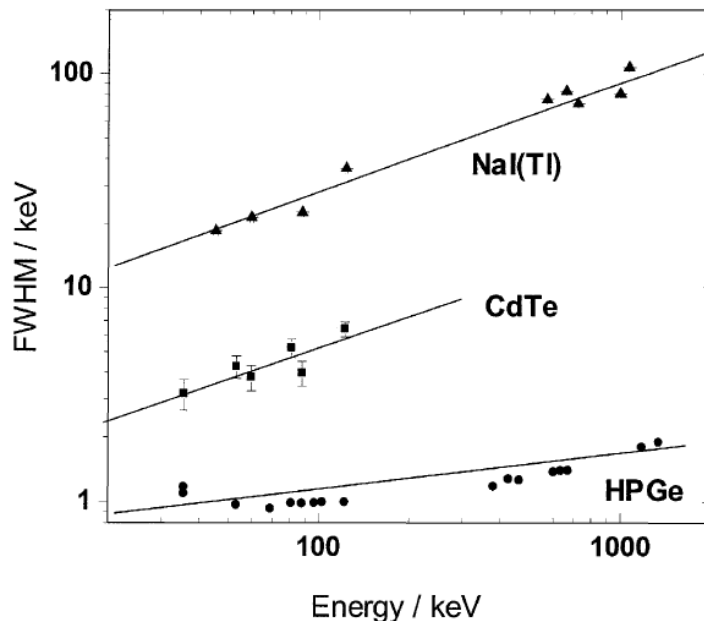


Figure 2.4.: Energy resolution of NaI(Tl), CdTe and HPGe detector as a function of gamma ray energy [20].

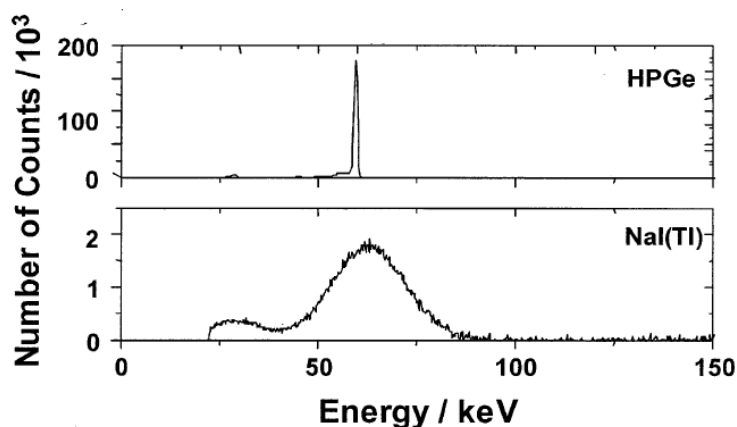


Figure 2.5.: Energy spectrum of ^{241}Am obtained with a HPGe and a NaI(Tl) detector [20].

2.2.1. Scintillation detectors

A short discussion about the scintillator detectors is presented here as they are used in our system, which is described in chapter 3 and 4.

Scintillator

When an ionizing radiation falls on a scintillating material, the material can emit light via any of the three basic interaction mechanisms described before depending on its energy. As radiation passes through the scintillator, it excites the atoms and molecules, which emit light when de-exciting. Scintillators are classified as organic and inorganic scintillators. The organic scintillators are hydrocarbon compounds containing linked or condensed benzene ring structures. The light in organic scintillators arises from the transitions in the energy level structure of single molecules. Their most distinguishing feature is a very rapid decay time on the order of a few nanoseconds. These detectors are used as mixtures of one or more compounds in liquid solutions or in a solid plastic solvent.

The inorganic scintillators are mainly the crystals of alkali halides. The scintillation mechanism in organic materials is molecular in nature, whereas in inorganic scintillators, it is a characteristic of the electronic band structure found in solids. The incident energy of photons is absorbed by the electrons in the valence band and they are excited to the conduction band. The return of the electron to its normal state in the valence band results in the emission of a photon. This photon has too high energy to be in the visible region. In order to increase the probability of visible photon emission, some activators are added to scintillators. These activators create energy states between the valence and conduction band, Fig. 2.6. The de-excitation from these intermediate energy levels give rise to visible photons. The most widely used inorganic scintillators are NaI(Tl) (sodium iodide doped with thallium), CsI(Tl), CsI(Na), CsF. Some non-alkali crystals include BaF₂, ZnS(Ag), CdWO₄, YAG(Ce) (Y₃Al₅O₁₂(Ce)), GSO, LSO, LYSO.

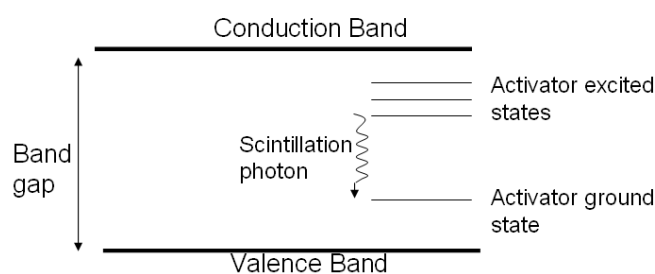


Figure 2.6.: Energy band structure of an activated scintillator [19].

A disadvantage of inorganic crystals is the hygroscopy of some of them, e.g. NaI, a property which requires them to be housed in an air-tight enclosure to protect them from moisture. CsI(Tl) and BaF₂ are only slightly hygroscopic and usually do

not need protection. CsF, NaI(Tl) are hygroscopic, while BGO, CaF₂(Eu), LYSO (Lu_{1.8}Y_{0.2}SiO₅(Ce)), and YAG(Ce) are not. Inorganic crystals have higher stopping power due to higher density and higher atomic number. Because of the higher light output, they have better energy resolution as compared to organic scintillators.

A scintillation detector consists of a scintillating material, which is optically coupled to photomultiplier tube (PMT) or a photodiode. If the emission of light in atomic de-excitation occurs prompt, i.e. within the $\approx 10^{-8}$ seconds, the process is called fluorescence. Sometimes, the excited state is metastable, so the de-excitation is delayed. The process then corresponds to either phosphorescence, with longer wavelength light or delayed fluorescence with longer emission time. The light detectors absorb this light and re-emit the corresponding energy in the form of electrons. In the case of photomultiplier tubes, light in a certain wavelength range is transformed by the photocathode into photo-electrons. Using a chain of dynodes at different potentials, the original/initial photo-electrons are multiplied, typically up to a pulse of 10^7 - 10^{10} electrons. A brief discussion about PMTs is given in later sections. There are two general designs for Photodiodes. Conventional photodiodes have no internal gain and operate by directly converting the photons from the scintillation detector to electrons that are simply collected. Avalanche photodiodes have an internal gain through the use of higher electric fields that increase the number of charge carriers that are collected. In summary, an effective scintillation detector should possess the following properties :

1. High scintillation efficiency
2. Light yield proportional to the deposited energy
3. Good light collection, the medium should be transparent to the wavelength of its own emission
4. In order to have an efficient coupling of the scintillation light to a photo-detector, the refractive index of the materials should be similar to each other
5. The decay time should be short for fast signal generation.

Light readout from a scintillator using photomultiplier tubes A photomultiplier is a fast amplifier, which is optically glued to a scintillator to collect the light emitted from it. It transforms the visible light into an electric current and amplifies it by a factor of 10^6 or more. It consists of an evacuated glass tube with a photocathode at its entrance and several dynodes in the interior (Fig. 2.7). The photons produced in the scintillator hit the photocathode, which is made of a material that emits photoelectrons when photons strike it. With the help of an electric field created by the applied high voltage, the electrons are guided towards the first dynode. The energy deposited by the incident electron on the dynode can result in the reemission of more than one electron. It depends on the material of the dynode and also on the kinetic energy of the electron. The kinetic energy of electrons is a sensitive function of the applied accelerating voltage. The secondary electrons emitted by the first dynode move towards the second dynode, from there towards the third, and so on. The production of secondary electrons results in a final amplification of the number of

electrons. The amplification of a PMT thus depends on the number of dynode stages and on the applied high voltage. The anode, located at the end of the dynode series serves as the collector of electrons.

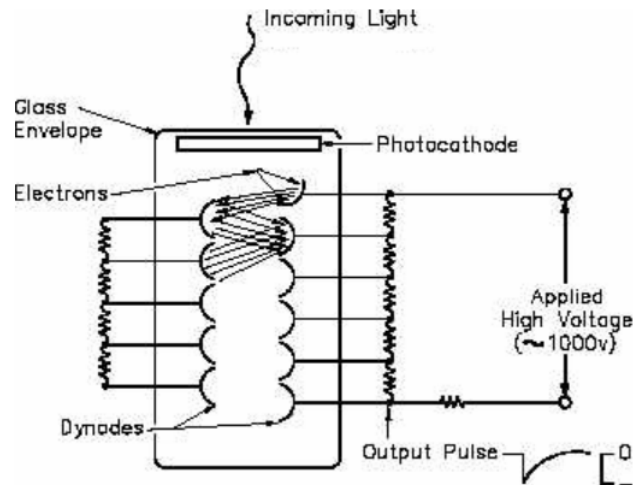


Figure 2.7.: Schematic diagram of the interior of a photomultiplier tube.

Since the light falling on the surface of photocathode is spread over it uniformly, the information about the point of interaction within the photocathode is not available. However, in some applications this information is required. This led to the development of position sensitive photomultiplier tubes (PSPMT). A typical PSPMT consists of a photocathode sensitive to the scintillation light wavelength, multiple dynodes for photo-electron multiplication, and multi-anode wires crossing each other in X and Y directions. For example, H3292 [21] is a PSPMT from the company Hamamatsu having 28 anodes in X direction and 28 anodes in Y direction (Fig. 2.8). A simplified anode readout uses an interconnected chain of resistors, both ends of each chain being terminated by a resistor that converts the collected photocurrent into a voltage. When an electron is produced by the photocathode it creates an electron shower that is spread over a number of anode wires. By calculating the "centre of gravity" one can determine the origin of the incident photon with very good position resolution. Chapter 4 gives an elaborate explanation of PSPMTs.

2.2.2. Semiconductor detectors

As the name implies, a semiconductor detector is a device which uses a semiconductor to detect photons. The charge carriers in the case of semiconductors are electrons and holes. Silicon and germanium are the most commonly used semiconductors for such detectors. Some of the most important advantages of this category of detectors are excellent energy resolution, higher efficiency for a given size, availability in special

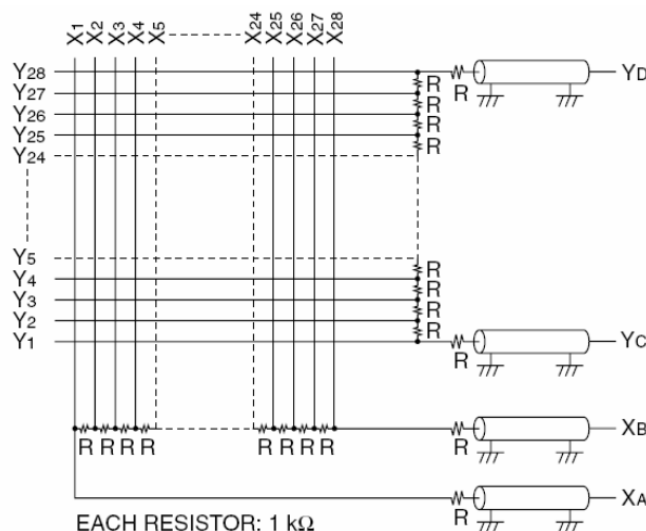


Figure 2.8.: Crossed anode wire structure of Hamamatsu H3292 position sensitive photomultiplier tube.

geometrical shapes and fast pulse rise times. The reader is encouraged to read Ref.[19] to have a detail description of this category of detectors.

Principle of operation

The crystal lattice structure of a semiconductor can be explained by energy bands, where the electrons are located. The energy bands in a semiconductor are classified as valence and conduction band, separated typically by a band gap of about 1 eV. The electrons in a valence band are bound to the atomic nucleus. Only the electrons, which move freely in the crystal, can contribute to electrical conductivity. These freely moving electrons are available when they jump from the valence band to the conduction band passing the band gap. When an energetic particle strikes a semiconductor, bound electrons in the valence band gain energy via one of the interaction mechanisms like, photoelectric effect, Compton scattering of photon or pair production. If the energy gained by the electron is higher than the band-gap, they move to the conduction band. During this process, they leave vacancies behind which are called holes. In a semiconductor detector, when a voltage is applied to opposite electrodes, the free electron-hole pairs feel the electrostatic force of the applied field. They start to drift towards the contacts and induce an electric signal at the corresponding electrode.

The addition of a small percentage of foreign atoms in the regular crystal lattice of silicon or germanium produces dramatic changes in their electrical properties, producing n-type and p-type semiconductors. A doped semiconductor is also called an extrinsic semiconductor.

n-Type Semiconductor:

The addition of pentavalent impurities, called donors, such as antimony, arsenic or phosphorus contributes free electrons, greatly increasing the conductivity of an in-

intrinsic semiconductor. The conduction electrons are the majority charge carriers and holes are minority charge carriers.

p-Type semiconductor:

The addition of trivalent impurities, called acceptors, such as boron, aluminium or gallium to an intrinsic semiconductor creates holes. Here holes are the majority charge carriers.

The electrical properties of a doped semiconductor material are determined by the majority charge carriers. The free electrons and holes created by the impurity atoms lie in discrete energy levels, called donor and acceptor levels for n type and p type semiconductors respectively. In the case of n-type semiconductor these energy levels lie extremely close to the conduction band (Fig. 2.9) being separated by 0.01 eV in germanium and 0.05 eV in silicon. At room temperature, therefore, the extra electron is easily excited into the conduction band where it will enhance the conductivity of the semiconductor. Similarly in the case of p-type semiconductor material the additional energy state is created close to the valence band, Fig. 2.9. Electrons in the valence band are then easily excited into this extra level, leaving extra holes behind.

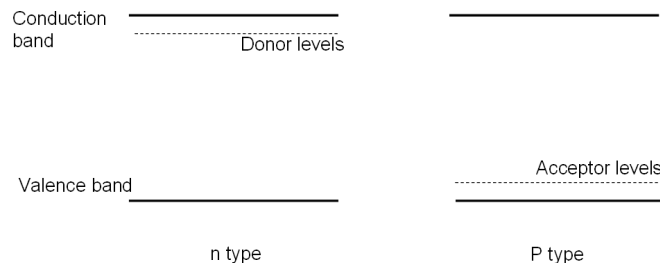


Figure 2.9.: Representation of donor and acceptor energy levels created in between the band-gap in a n type and p type doped semiconductor material.

The pn semiconductor junction A pn junction is formed when a p-type semiconductor makes a good thermal contact with an n-type semiconductor material. The formation of a pn junction creates a special zone at the interface between the two regions. There is diffusion of electrons and holes between the junction because of difference in the impurity concentration of electrons and holes for the two materials. As a consequence, the diffusing electrons fill up holes in the p-region while the diffusing holes capture electrons on the n side. This recombination of electrons and holes causes a charge build-up on both sides of the junction. This is illustrated in Fig. 2.10. This creates an electric field gradient across the junction which eventually halts the diffusion process leaving a region of immobile space charge. Because of the electric field there is a potential difference across the junction. This is known as the contact potential generally being of the order of 1 V.

The region of immobile charge is known as depletion zone or space charge region. The volume of this zone can be used to detect γ interactions. The width of the depletion zone depends on the impurity concentration and is given by :

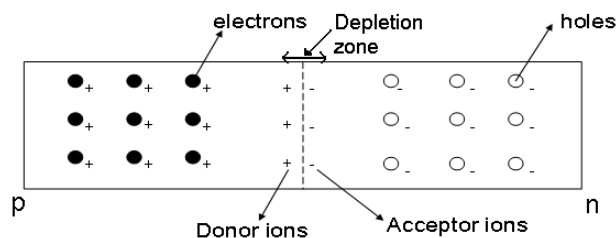


Figure 2.10.: Schematic diagram of a pn junction.

$$d = \left[\frac{2\epsilon V_0 (N_A + N_D)}{e N_A N_D} \right]^{1/2} \quad (2.5)$$

where ϵ is the dielectric constant, e is the electron charge and N_D and N_A are the donor and acceptor impurity concentrations. V_0 is the built-in potential. The magnitude of the electric potential inside the depletion region can be calculated using the Poisson equation,

$$\frac{d^2 V_0}{dx^2} = -\frac{\rho(x)}{\epsilon} \quad (2.6)$$

where ρ is the net charge density. Having calculated the potential map in the detector, the electrostatic field can then be found as :

$$E(x) = -\frac{dV_0}{dx} \quad (2.7)$$

The photon interaction results in the formation of electron hole pairs. The electric field of the unbiased depletion zone is not strong enough and recombination can occur.

Reverse biased junctions In order to use a semiconductor as a detector, a reverse bias voltage has to be applied to the depletion zone so that an enlarged effective detection area and a strong electric field is achieved. This is done by applying a negative voltage to the p-side as compared to the n-side as shown in Fig. 2.11. This increases the width of the depletion region. Semiconductor detectors are usually biased at a depletion voltage which is high enough to fully deplete the crystal volume and to ensure strong electric field for complete collection of charge carriers.

Typical bias voltages are 500-4000 V depending on the impurity concentration and on the semiconductor size. If the n-side doping level is much higher than the p-side, so that $N_D \gg N_A$, the space charge extends much farther into the p side than the n side. Then using equation (2.5) the depletion width is given by :

$$d = \left[\frac{2\epsilon V}{e N_A} \right] \quad (2.8)$$

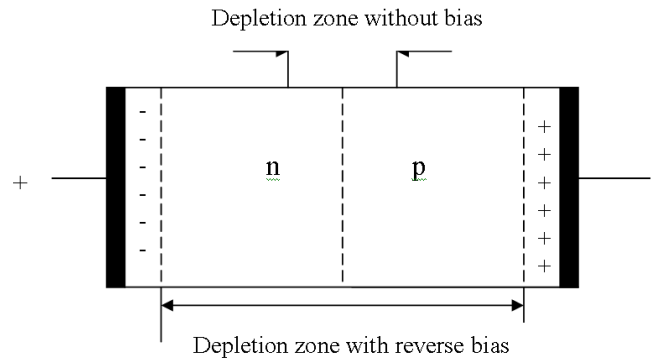


Figure 2.11.: Reverse biased pn junction.

where V is the applied reverse bias. Similarly if the p-side doping level is much higher than the n-side, so that $N_A \gg N_D$, the space charge extends much farther into the n side than the p-side. So N_A will be replaced by N_D in equation (2.8) for the depletion depth. A generalized solution for the depletion depth in a reverse biased junction is therefore given by :

$$d = \left[\frac{2\epsilon V}{eN} \right] \quad (2.9)$$

N now represents the dopant concentration (either donors or acceptors).

2.2.3. High purity germanium detectors

Germanium semiconductor material has atomic number 32 as compared to 14 for silicon. It thus has a higher attenuation coefficient for high energy gamma rays. In addition it has a density of 5.33 g/cm^3 , more than 2 times higher than of silicon, which results in generation of more charge carriers for the same energy gamma ray and hence better energy resolution. For high resolution gamma-ray spectroscopy, germanium is therefore preferred over silicon. From equation (2.9), it is clear that for a given applied voltage, greater depletion depth and hence greater active detection volume can only be achieved by lowering the value of the dopant concentration N . The refining techniques available are capable of reducing the impurity concentration to approximately 10^{10} atoms/cm³ in the case of germanium. At this impurity level in germanium, equation (2.9) predicts that a depletion depth of 10 mm can be achieved using a reverse bias of less than 1000 V. Detectors that are manufactured from this ultra pure germanium are usually called intrinsic germanium or high-purity germanium (HPGe) detectors and they have become available with depletion depth of several centimeters. The ultra pure germanium is produced by processing a bulk germanium using the technique of zone refining several times. If the remaining low level impurities in the processed germanium are acceptors (or donors), the electrical properties of the semiconductor crystal grown from this material will be p-type (or n-type).

Configurations of HPGe detectors

(A) Planar configuration

Figure 2.12 shows a planar HPGe detector fabricated from p-type germanium. In this configuration, the n^+ and p^+ electrical contacts are provided on the two flat sides of the germanium disk. To reverse bias the detector, positive voltage is applied to the n^+ contact with respect to the p^+ surface. The depletion region begins at the n^+ edge and extends deeper into the p region. The voltage is increased until the detector is fully depleted.

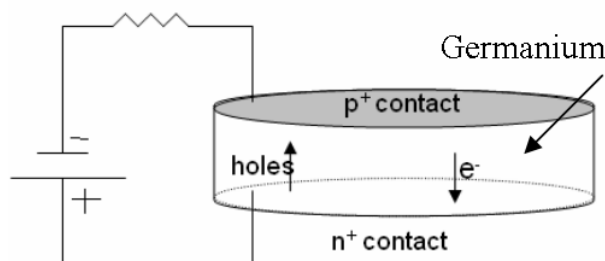


Figure 2.12.: Planar HPGe detector configuration.

(B) Coaxial configuration

In the coaxial configuration (Fig. 2.13), the detector is constructed in a cylindrical geometry. One electrode is fabricated at the outer cylindrical surface of a long cylindrical germanium crystal. A second cylindrical contact is provided by removing the core of the crystal and placing a contact over the inner cylindrical surface. Much larger active volume is available in this geometry as compared to the planar design. If the core extends along the entire length of the axis, the configuration is then known as a true coaxial or open-ended coaxial detector. To increase the sensitive volume even further, the outer electrode can be extended over one flat end of the cylindrical crystal and only a part of the central core is removed. These are known as closed-end coaxial detectors.

2.3. Pulse shape analysis

When a γ -ray interaction takes place inside the volume of a fully depleted HPGe detector, it results in the formation of electron-hole pairs. These charge carriers start to move towards the opposite p^+ and n^+ contacts under the influence of applied bias voltage and establishes an induced charge at the electrodes. The preamplified charge signals for the interaction positions constrained inside the germanium are digitised by the digitisers. These charge signals can be utilized to obtain the energy deposits and the interaction positions. This is known as pulse shape analysis (PSA).

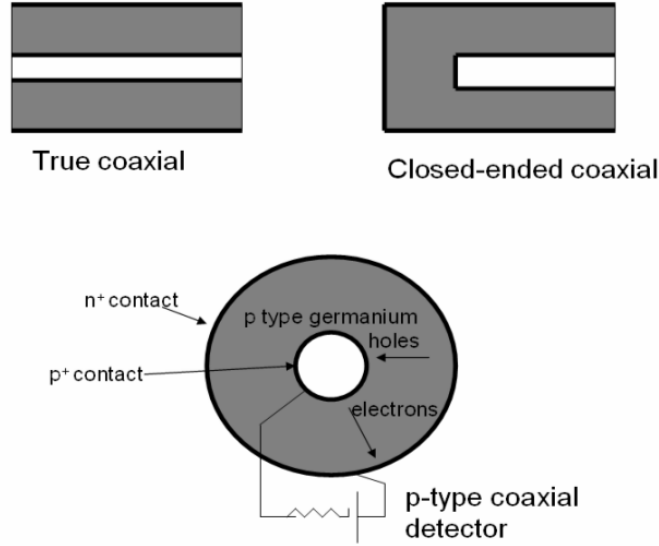


Figure 2.13.: Coaxial HPGe detector configuration.

2.3.1. Pulse formation in germanium detectors

At low-to-moderate values of the electric field intensity at a position r in the detector, the drift velocity $\nu_{e,h}(r)$ of either the electron or the hole is approximately proportional to the electric field, $E(r)$. The corresponding proportionality factor is defined as a quantity called mobility of the charge carrier.

$$\nu_{e,h}(r) = \mu_{e,h}E(r) \quad (2.10)$$

At higher electric field values, the drift velocity increases more slowly with the field. Eventually, a saturation velocity is reached which becomes independent of further increase in the electric field. Figure 2.14 shows the dependence of the drift velocity of electrons and holes on the field magnitude for germanium. The variation of the drift mobility for the electrons and holes in an n-type germanium material is shown in Fig. 2.15. Mobility decreases with increasing doping, since the increased ionized impurities enhance the scattering of charge carriers leading to lower mobilities. To determine the drift velocities, the electrostatic field has to be first calculated. The value of potential at any point inside a detector of defined geometry is found by solving the Poisson equation:

$$\nabla^2\phi(r) = -\frac{\rho(r)}{\epsilon} \quad (2.11)$$

where $\rho(r) = en$, is the space charge density, e is the electron charge and $\epsilon = \epsilon_0\epsilon_r$ is the dielectric constant with $\epsilon_r = 16$ for a germanium detector. n is the impurity concentration defined as the difference between the density of donors N_D and the

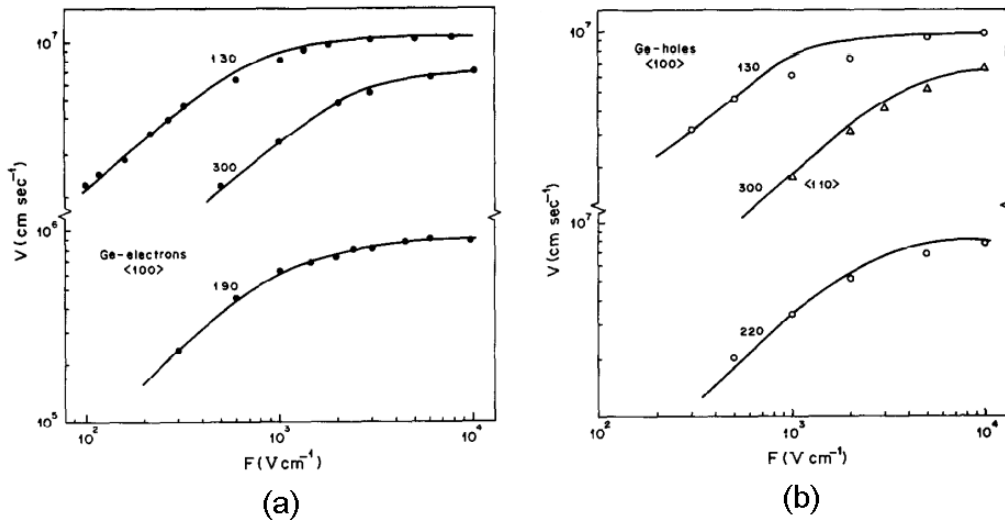


Figure 2.14.: Drift velocity as a function of electric field for electrons and holes in germanium [23].

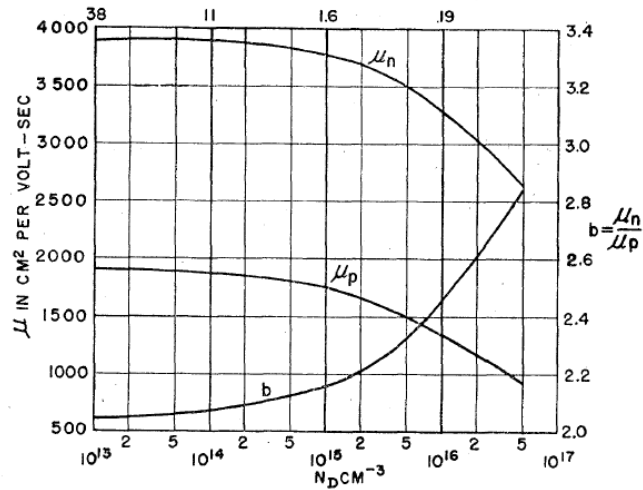


Figure 2.15.: Variation of drift mobility of electron and holes as a function of the impurity concentration in an n-type germanium material at 300 K [24].

density of acceptors N_A . After calculating the potential map in the detector, the electrostatic field can then be found using:

$$E(r) = -\nabla\phi(r) \quad (2.12)$$

For a p type planar germanium detector of thickness d and an applied voltage of V volts, the electric field at a distance x from the p^+ contact is given by,

$$E(x) = -\frac{V}{d} - \frac{\rho}{\epsilon} \left[\frac{d}{2} - x \right] \quad (2.13)$$

For a simple coaxial germanium detector with inner and outer radii of r_1 and r_2 , the electric field is given by:

$$E(r) = \frac{\rho r}{2\epsilon} - \frac{1}{r} \left[\frac{V + \frac{\rho}{4\epsilon}(r_2^2 - r_1^2)}{\ln \frac{r_2}{r_1}} \right] \quad (2.14)$$

where V is the applied reverse voltage (See Appendix for the derivation of equations 2.13 and 2.14).

A current $I(t)$ is induced inside the detector because of the drift of electrons and holes towards the electrodes. This induced current is determined by the charge amplitude Q_0 , the weighting field $E_w(r)$, and the charge drift velocity $v_{e,h}(r) = dr/dt$:

$$I(t) = Q_0 E_w(r) \frac{dr}{dt} \quad (2.15)$$

The weighting field E_w of an electrode is defined as the electric field calculated by solving the Poisson equation 2.12, taking a potential of 1 Volt on the considered electrode and zero on all the other electrodes. Using equation 2.13 (or 2.14), which gives the electric field at a position x (or r), for the charges induced in either electrode (external or internal electrode) of a planar (or coaxial detector), the induced current $I(t)$ can be calculated. The spatial charge density ρ should be assumed zero here, since this field represents the capacitive coupling between the electrode and the moving charge. When this induced current is integrated over the long time constant of the measuring circuit, it gives the corresponding induced charge $Q(t)$.

For a planar geometry with electric field given by equation (2.13), the induced charge is

$$Q(t) = \frac{Q_0}{d} [\nu_e t_e + \nu_h t_h] [19] \quad (2.16)$$

where t_e and t_h are the electron and hole collection times respectively. The instantaneous charge reaches its maximum value Q_0 when both the electrons and holes are collected at their respective electrodes.

For a coaxial geometry with electric field given by equation (2.14), the induced charge is,

$$Q(t) = \frac{Q_0}{\ln \frac{r_2}{r_1}} \left[\ln \left(1 + \frac{\nu_e t}{r_0} \right) - \ln \left(1 - \frac{\nu_h t}{r_0} \right) \right] [19] \quad (2.17)$$

where r_0 is the position where the charges are created.

The induced charge is thus a function of both the electron and hole mobility which implies that the signal has two components, one corresponding to the drift of electrons and the other related to the drift of holes. This feature is exploited by the PSA algorithms in order to determine the location of the γ -ray hit. The amplitude of a pulse corresponding to a particular interaction point is proportional to the energy absorbed at that point.

2.3.2. PSA in a planar HPGe detector

For different distances from the electrodes, there exists a characteristic signal shape behaviour and the drift of both the electrons and holes has an interplay in that, (see equation 2.16). Figure 2.16(a) shows a schematic diagram of a p type planar germanium detector with four different γ -ray interaction positions along its thickness and the corresponding charge pulses in panel (b). The amplitude indicates the charge $Q(t)$ collected at the electrodes due to the motion of the charge carriers.

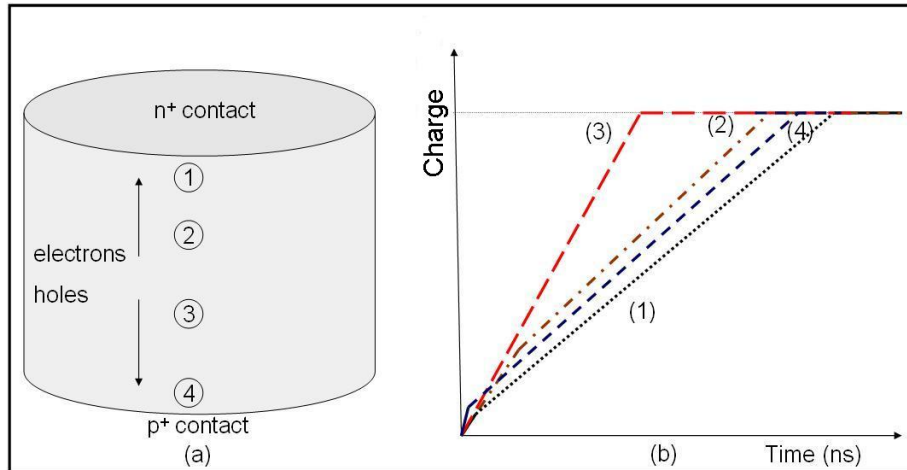


Figure 2.16.: (a) Schematic diagram of a planar germanium detector showing four different γ -ray interaction positions (b) The expected behaviour of pulse shapes at the mentioned interaction points, [19].

The electrons in germanium semiconductor material have higher mobility as compared to the holes. For the interaction at position (1), the electrons are collected very fast at the n^+ contact while the holes have to travel the distance over the thickness of detector to reach the p^+ layer. The shape of the charge pulse for this interaction point is thus dominated by the slow motion of holes. The opposite explanation is true for the interaction (4) close to p^+ contact, when the holes are collected very fast but electrons have to reach to the n^+ layer. For an interaction point away from the contacts, the motion of both the electrons and the holes is evident in the shape of the pulse. When an interaction takes place close to the center of the planar detector, both

electrons and holes have to travel the same distance. The signals are fastest for the spatial positions where the collection time of electrons and holes is same. For a uniform electric field distribution inside the planar detector volume, the pulses at same vertical distance from either contact are expected to have the same pulse shape behaviour.

2.3.3. PSA in a coaxial HPGe detector

The shape of the net charge pulse from either of the electrodes in a coaxial germanium detector provides information about the radial interaction position [19, 25]. Figure 2.17 shows an example of three different interaction points labelled as 1, 2 and 3 inside a coaxial HPGe detector. For net charge signals resulting from γ -ray interactions occurring in the vicinity of either of the electrodes, the pulse rises slowly because either the electrons or the holes have to travel a longer distance. Although both the pulses (1) and (3) have long rise time, they have different shapes because of different dominant charge clouds (holes in one case and electrons in the other). When the interaction takes place in the middle of the detector active volume the pulse rises faster as electrons and holes have to travel the same distance. The radial interaction information is thus extracted from the net charge signal.

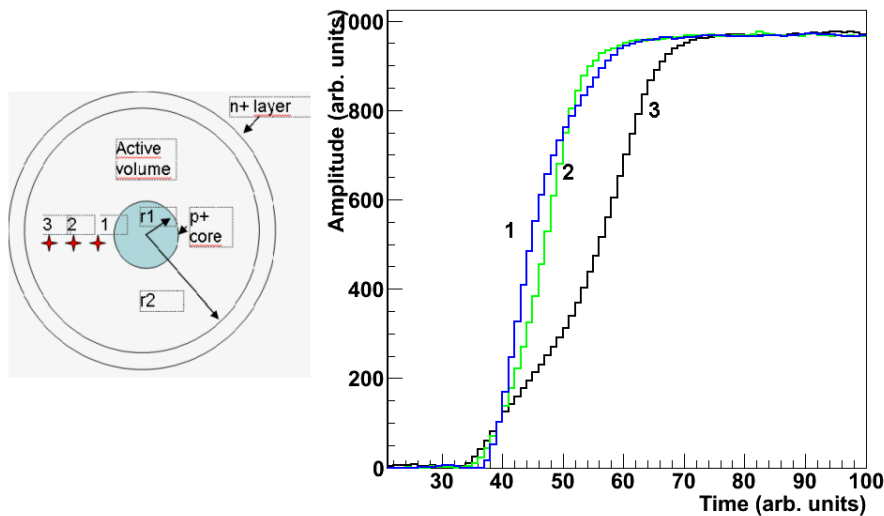


Figure 2.17.: Charge pulses for a coaxial detector for three interaction points along the radial line.

Contact segmentation and azimuthal information

If the electrodes on the germanium detector are segmented, separate pulses are obtained from each segment. The position sensing can be extended beyond just the radial coordinate by comparing the size of the individual electrode signals [7]. For a photon striking a segmented detector, two types of signals are available: (1) the net

charge signal from the segment hit by the γ -ray and (2) the transient induced signals from the neighbouring segments, also called mirror signals. The motion of the charges in the segment hit by the gamma ray induces a charge in the neighbouring segment. The transient signals therefore have non-zero values only for the time when the charge is drifting in the segment hosting the interaction. Transient signals carry azimuthal position information. The mirror charge signal amplitude will be higher if the interaction takes place close to the boundary of two segments and the amplitude decreases as the distance of the interaction point from the segment boundary increases. This is illustrated in Fig. 2.18 for the case of an AGATA crystal, which is a 36 fold segmented germanium detector.

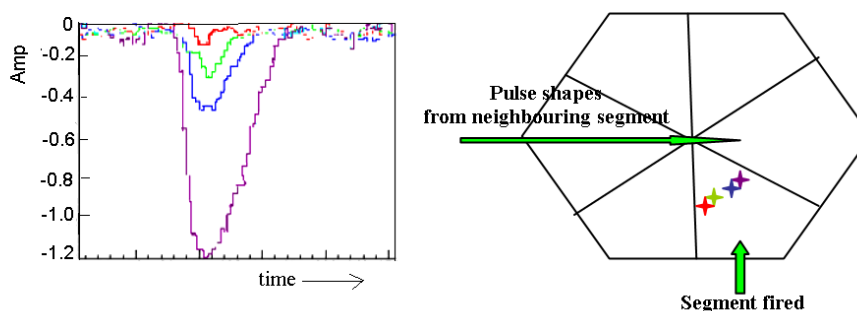


Figure 2.18.: Variation in the transient signal amplitude as the distance of the interaction point changes from the segment boundary. The distribution of interaction points in the hit segment is shown schematically in the right part of the figure. The arrow indicates the neighbouring segment. The transient signals in this segment for the corresponding positions (shown in color) are shown (left). The amplitude of the mirror charge is maximal (violet) for the interaction position located closest to the neighbouring segment.

The determination of the gamma ray hit position in a segmented detector can be very intuitively understood from the example shown in Fig. 2.19. The highlighted circled area shows the main channels contributing to a particular event. The rising charge pulse is from the segment which is fired by the photon while the other three negative pulses are the transient pulses induced in the neighbouring segments.

From the above discussion of the charge pulses from a segmented coaxial detector, it is evident that the rise time and shape of signals from a net charge collecting segment gives information about the radial interaction position, while azimuthal information is given by analysing the transient signals. By means of this information, pulse shape analysis applied to detectors with medium level segmentation of about 20-40 segments, can provide a position accuracy of ≈ 1 -2 mm.

Need to scan segmented detectors

PSA algorithms [26, 27, 28] have been developed in order to reconstruct in an efficient

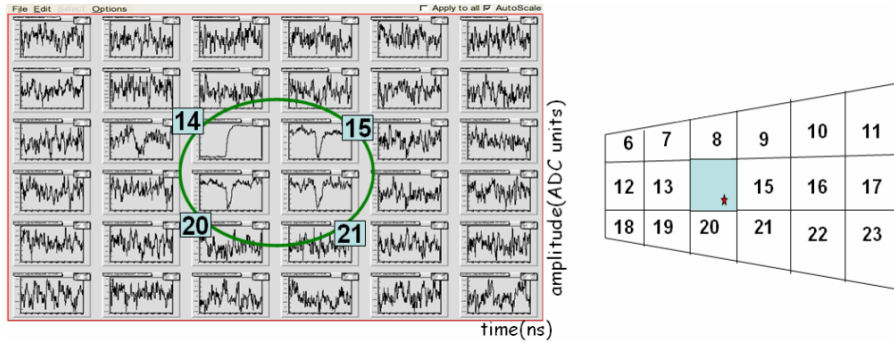


Figure 2.19.: Experimental pulse shapes from an AGATA crystal. The highlighted area shows the positive rising pulse from the segment which hosts the photon interaction (shown shaded in the right sketch), the other three negative pulses are from neighbouring segments.

and reliable way the location of a γ -ray hit inside the active volume of a germanium detector. Such algorithms compare the measured hit-segment and transient charge signals with a database of pulses, which has been previously determined and contains both the pulse-shapes and the corresponding interaction locations.

Such databases can be obtained from mathematical approaches (see Sec. 2.3.1). Due to electric field distortions, defects and other experimental or detector/cryostat related features, it turns out that it is more accurate to determine such database experimentally. For this purpose, we have developed a system to scan and characterise spatially the response function of HPGe detectors. The next chapter explains the principle of the gamma detector scanner at GSI.

3. Scanner for gamma-ray detectors

Many rare and exotic territories of the nuclear chart have been explored using gamma ray spectroscopy with high purity germanium (HPGe) detectors. Over the years, these germanium arrays have been improved from Compton veto systems to the composite germanium detector assembly. The advancement in the field of semiconductor crystal segmentation technology, made feasible the development of 4π germanium arrays like AGATA [17] and GRETA [16]. The germanium crystals used in these arrays are electrically segmented. It is possible to locate an interaction position with a spatial resolution proportional to the size of the segment which is fired in that event. But using the signal information from all the segments and applying the concept of pulse shape analysis to these detectors, a position resolution of smaller than the size of an individual segment can be achieved. A gamma ray tracking algorithm involves measuring the position and energy of each gamma ray interaction inside the detector [30, 31]. The path of a photon inside the detector volume can be reconstructed using this information applied to the Compton scattering formula. The efficiency of the tracking algorithms thus depends on how accurately the position response of a detector is determined. Before installing the segmented germanium detectors in tracking spectrometers, a full 3D scanning of the detectors which experimentally determines the pulse shapes for every given position inside the active volume is therefore needed. As one of the possible ways, we proposed and implemented a first detector scanner based on the principles of pulse shape comparison and positron annihilation correlation. The following sections will explain the principle of the scanning system developed at GSI and the various tests that have been done for its development.

3.1. Conventional scanning principle

The schematic diagram of a conventional scanning system [33] is shown in Fig. 3.1. A collimated monoenergetic photon source, e.g. ^{137}Cs , is placed below the front face of the HPGe detector. In order to have a narrow pencil-like γ -ray beam, the collimator is typically of 1 mm diameter and 10-12 cm length. This source is placed on a high precision x-y positioning/scanning table, which can be moved independently in x-y directions via sliders with typically 100 μm precision. Gamma rays are injected from the source into the detector volume which is to be scanned.

The (x,y) coordinates of the gamma interaction points in the germanium volume are given by the scanning table position. The uncertainty in the determination of these

coordinates is mainly constrained by the beam divergence due to the finite size and length of the collimator and in second order by the resolution of the table itself.

In order to find the depth of interaction points, use of photons which are Compton scattered at around 90° out of the germanium volume is made. These scattered photons have to pass through a gap in the lead collimators surrounding the germanium, and interact with the scatter detectors placed behind them. The height of the center of a collimator gap which is in front of the scatter detector, gives the z coordinate of photon interaction point.

For a 661 keV gamma ray from ^{137}Cs , in order to localise the interaction point, it is required that the photon deposits 373 ± 15 keV in the HPGe detector and 288 ± 15 keV in one of the scatter detector, within a predefined time coincidence window. The solid black line in Fig. 3.1 shows one such track. Charge pulses are collected for each position with enough statistics. A pulse shape obtained from the average of typically 100 pulses is associated with each point.

In order to scan large volume HPGe detectors, the collimated source has to be moved usually in 1-2 mm steps along each x and y direction. This takes a considerable amount of time. For instance, the scan for 1200 positions of a large volume AGATA detector takes more than 2 months. Also, the coincidence count rate in the rear part of large detectors is small as compared to the rates in the front part. It has been observed that for a 920 MBq ^{137}Cs source, the rates are reduced from 40Hz to 1 Hz in the back region of an AGATA detector.

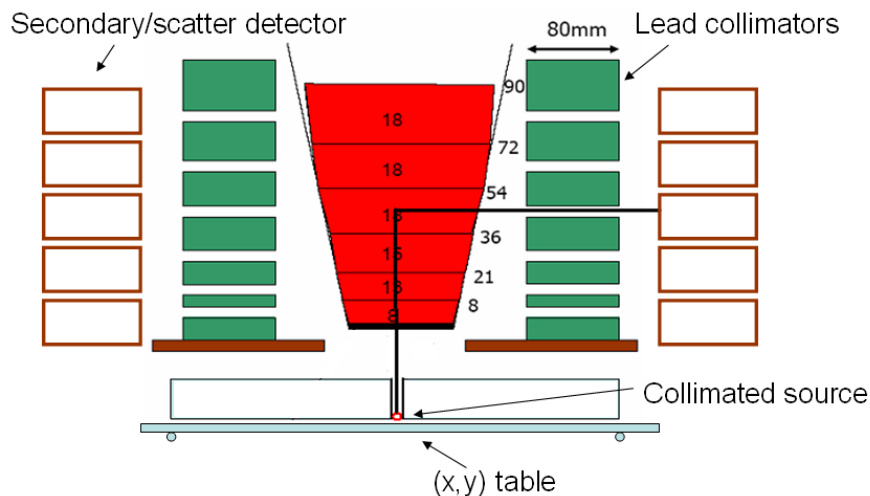


Figure 3.1.: The schematic diagram of a conventional scanning system.

To overcome the aforementioned limitations, we have developed a novel 3D scanner at GSI, which determines the position response of HPGe detectors in a much shorter time as compared to the conventional scanning system. It is based on the principles of pulse shape comparison (PSC) [34] and positron annihilation correlation (PAC)[35, 36] which are explained in sections 3.2 and 3.3, respectively.

3.2. Pulse shape comparison principle

In segmented HPGe detectors like AGATA, two single interaction gamma events give two distinguishable pulse shapes, provided that the interaction points are separated by at least the intrinsic spatial resolution of the HPGe detector, which due to electronic noise is typically of the order of 2 mm. Instead of using the standard coincidence technique (cf section 3.1) one can determine the position response of germanium detectors utilizing the concept of pulse shape comparison. This method is based on the comparison of two independent datasets. Each dataset corresponds to the signal shapes for single interaction events along a specific collimation direction of the gamma ray source. Figure 3.2 shows two orthogonal positions of the collimated source. The crossing point of these two collimation lines provides a well defined interaction point in the HPGe volume. The pulse shape for the crossing point is obtained by comparing the charge pulse shapes along one gamma-ray trajectory with the signal shapes of the orthogonal trajectory. The only case when the two signals match with each other is when they originate from a common point, which in this case is the intersection of the two collimation lines. The comparison of pulses is done on the basis of a χ^2 minimisation test. The advantage of this technique is that it does not require any gamma ray coincidence and the whole scanning procedure is thus much faster.

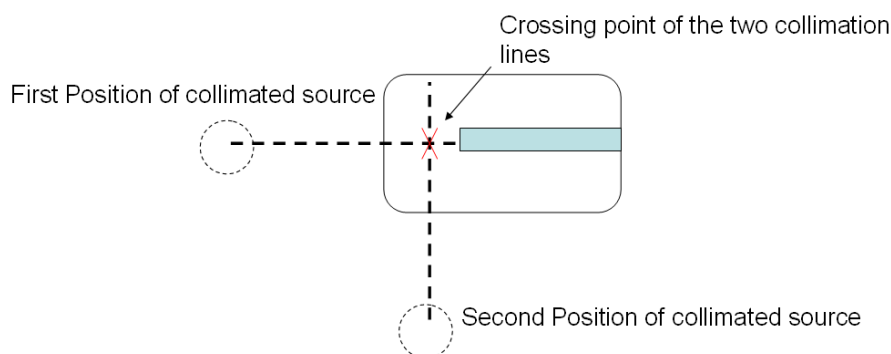


Figure 3.2.: Schematic diagram showing the pulse shape comparison technique. The HPGe is irradiated by a collimated source placed at two orthogonal positions. The intersection of two trajectories defines an interaction point in HPGe volume.

3.3. Positron annihilation correlation

The positron is the antiparticle of the electron. One possible way to obtain it, is from the β^+ decay of some radioactive isotopes, for example ^{22}Na .



As shown in Fig. 3.3, a proton decays to a neutron inside the nucleus and emits a positron and a neutrino. The ${}^{22}\text{Ne}$ is in excited state and a photon of 1274 keV is emitted from its de-excitation.

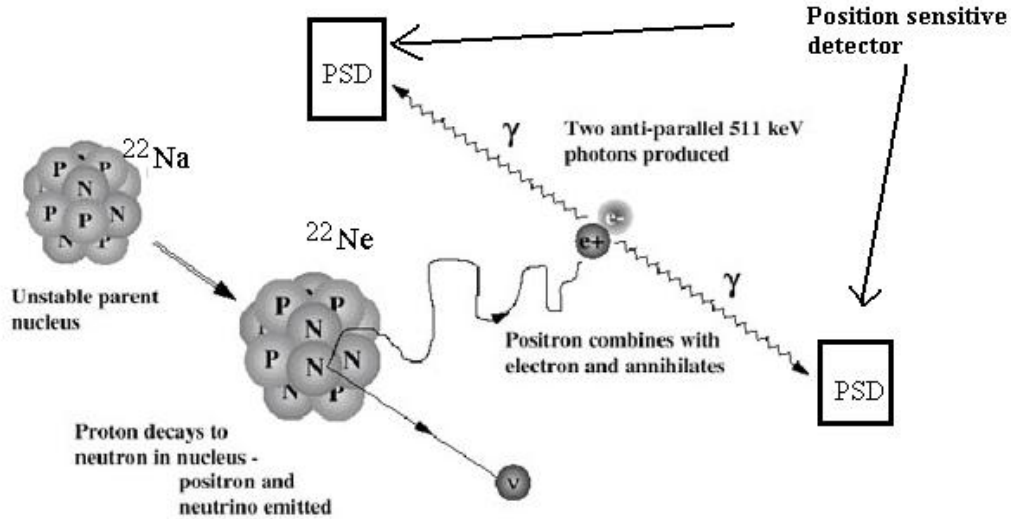


Figure 3.3.: The schematic diagram of β^+ decay, positron annihilation and detection of collinear γ rays by position sensitive detectors placed at 180° to each other.

The positron emitted in this nuclear decay travels a distance of few tenths of millimeters depending on its energy and surrounding material and eventually interacts with an atomic electron resulting in the formation of a short lived bound state called positronium. Positronium has a life time of approximately 0.5 ns. Following the energy conservation law, it annihilates into two or more photons having a total energy of 1.022 keV, as each of the annihilating particle has rest mass energy of 511 keV. The most probable case is the one in which it decays to two photons of 511 keV each. These two photons are directed exactly 180° to each other if the annihilation occurs at rest.

The collinear emission of photons is exploited in radiological imaging methods like SPECT and PET. The 511 keV γ rays emitted in opposite directions from radioactive pharmaceuticals in the human organs are detected by position sensitive detectors. The 3D and 4D images of the tracer are reconstructed to study the functional processes in the body. A proper time coincidence between the position detectors is demanded to distinguish between the γ -rays belonging to the same event and other gamma-rays emitted by the source or by other radiation sources.

3.4. Combination of PSC and PAC

We introduced a novel scanning system which applies the pulse shape comparison scan (PSCS) principle. Instead of using a collimated source to probe the HPGe detector, a point like ^{22}Na positron source is used. A position sensitive detector (PSD) is placed at 180° with respect to the HPGe detector. For a particular event, one $511\text{ keV } \gamma$ ray is registered by the position detector and the other by the HPGe detector. The time coincidence between the two detectors ensures that both gamma-rays come from the same event. The active area of the position sensitive detector and the source-PSD distance defines the opening cone of the $511\text{ keV } \gamma$ rays meant to probe the detector.

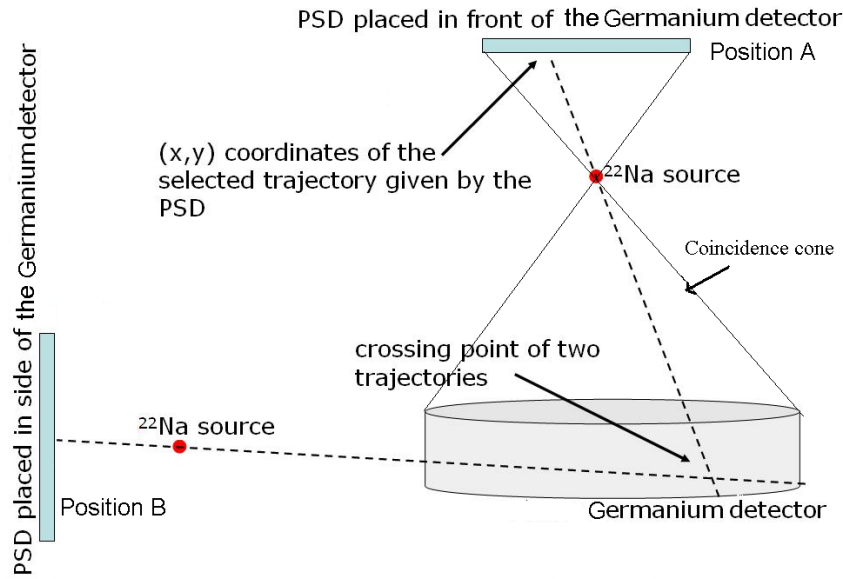


Figure 3.4.: Pulse shape comparison scan of germanium. Pulse shapes recorded for the collimation lines coming inside the coincidence cone of PSD and germanium for position A. Source and PSD moved together by an angle of 90° to be at position B and again a data set of pulse shapes is measured.

In the first measurement, for position A of the source and the PSD, Fig. 3.4, a data set of pulse shapes for all the trajectories coming inside the coincidence cone of the germanium and the PSD is recorded. The complementary data set needed by PSCS is obtained by rotating the PSD and ^{22}Na simultaneously along the axis of the Ge detector. In Fig. 3.4, it is shown that they are rotated by 90° , to be at position B. The pulse shape at a particular position inside the HPGe volume is disentangled in a similar way as in the case of a collimator based PSC scanner, by comparing the data set of pulse shapes along two particular trajectories selected for positions A and B. These two trajectories are chosen by selecting a narrow window in the 2D image of the HPGe detector obtained with the PSD. The use of position sensitive detector

allows creating a “collimation-free” scanner where many lines across the detector or even the whole detector can be scanned simultaneously. Also, since the source is not collimated, the required source activity can be several orders of magnitude smaller than the source activity needed in the case of conventional collimator-based scanners. With a 300 kBq ^{22}Na source, typically 5 days are needed to collect enough statistics for the full scan of one AGATA crystal.

3.5. Optimisation of scanner performance

Spatial Resolution

The efficiency of gamma tracking algorithms and hence the performance of a complete tracking array, depends on the precision with which the position of each interaction within the detector volume has been determined. In the proposed scanning system, the crossing point of the two concomitant trajectories localise the interaction point in the HPGe volume. These trajectories are selected using the 2D image taken with the PSD. The achievable position resolution with the scanner thus strongly depends on the spatial resolution of the PSD.

Additional uncertainty in the determination of interaction point coordinates in HPGe comes from the finite size of the source. The point source which we used is of 1 mm diameter. This introduces an inherent beam spread at the source which cannot be eliminated. However, for the final design of the scanning system, it is foreseen to employ a point-like source with smaller diameter.

Solid angle coverage

The device to obtain the position response of germanium detectors has not only to be precise but also to be time efficient. For the present system, implementation of a point like positron source instead of a collimated source serves to achieve this purpose. However, the source-PSD and source-HPGe distances have to be optimised for maximum exposure of the two detectors. The solid angle subtended by the detector at the point source position depends on the source-detector distance R and the detector radius r , as shown in equation 3.2.

$$\Omega = 2\pi \left[1 - \frac{R}{\sqrt{R^2 + r^2}} \right] \quad (3.2)$$

The solid angle subtended by the HPGe detector at the source should be large enough so that preferably all the germanium volume can be scanned in a single measurement. It is shown schematically in Fig. 3.5(b), when the HPGe detector is too close to the source, the solid angle coverage is small as compared to the case shown in Fig. 3.5(a). For a large volume AGATA detector with 80 mm front face diameter, source-HPGe distance of ≈ 120 -140 mm, corresponds to a solid angle of ≈ 13 -18 degrees. On the other hand, the surface area of the PSD used in the present device is fixed. It has a

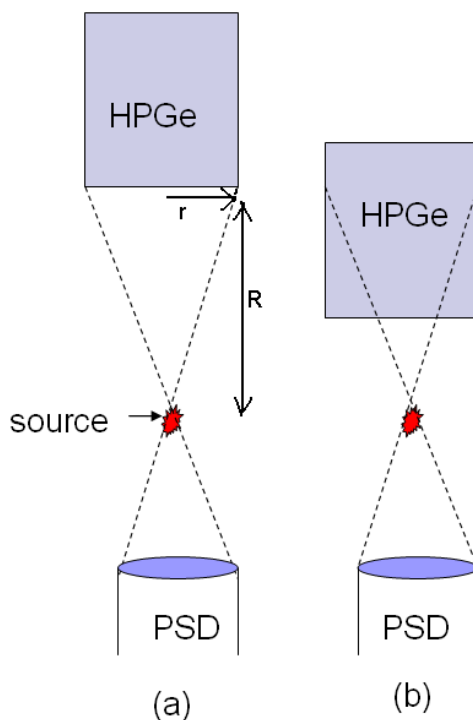


Figure 3.5.: (a) The source is placed at an optimal distance from HPGe detector to have maximum solid angle exposure (b) The HPGe detector is too close to source resulting in limited source exposure.

diameter of 5 cm and the ^{22}Na source is fixed at ≈ 5 cm from the center of its surface to achieve a solid angle of $\approx 26^\circ$.

Pile-up of charge pulses

Another issue which has to be taken care of is the pile-up of events in germanium because of high event rate. It is desirable to use a high activity source for the measurement to have sufficient amount of statistics in short time. However, with high count rate, the charge pulses arrive closer in time as compared to the pulse processing electronics time resolution. The pileup of signal shapes in those cases can be a serious problem. The two charge pulses coming too close in time are recorded as one single event. In Fig. 3.6(a), it is seen that the two pulses 1 and 2 arrive well separated in time. But Fig. 3.6(b) shows that when pulse 2 comes too close in time with pulse 1, it is superimposed on the tail of pulse 1. This leads to wrong amplitude charge pulse. An optimisation has to be made for an acceptable event rate. This depends on the source activity and also on the source germanium distance. A source-HPGe distance of 12-14 cm corresponds to an event rate of 20kHz for a 300 kBq ^{22}Na source for a large volume (60X60) mm² HPGe detector. This event rate is high enough to collect sufficient statistics in short time with only a small fraction of pile-up events.

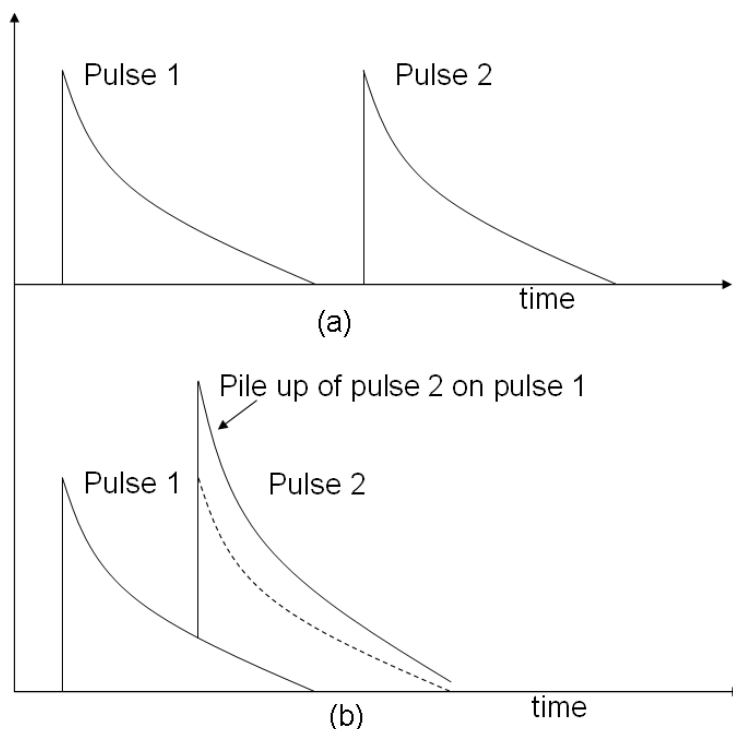


Figure 3.6.: (a) Two charge pulses which are well separated in time, (b) The pile-up from the tail of pulse 1 to pulse 2 when they arrive close in time.

3.6. Layout of the scanning table

A picture of the prototype scanning table is shown in Fig. 3.8. The scanning table has a double disk aluminium rotating ensemble of 40 cm diameter. It has a scale graduated in degrees and it can be rotated by any desired angle with a precision of better than 1 degree. An aluminium cuboid frame (25 cm x 25 cm x 38 cm) is attached to the rotating disk. The PSD and ^{22}Na are mounted on a common aluminium plate which is fixed at one corner of the cuboid frame. The use of the frame allows to lift the scanning system with respect to the ground and hence to reduce the back scatter background events. With the aid of the rotating ensemble, the source and PSD can be rotated simultaneously around the vertical axis of the whole system, where the HPGe detector has to be placed. They can also be moved back and forth via a horizontal slider below the aluminium frame holding them. The 300 kBq ^{22}Na source is placed inside a tungsten cylinder of 5 cm length with a conical hole of 1 mm diameter. This helps to collimate the γ rays in the field of view of both HPGe and PSD and to reduce considerably the background due to γ scattered events. As pointed out in section 3.5, the source is placed at ≈ 5 cm from the center of the PSD surface and ≈ 15 cm from the focal plane of the system to have maximum solid angle coverage.

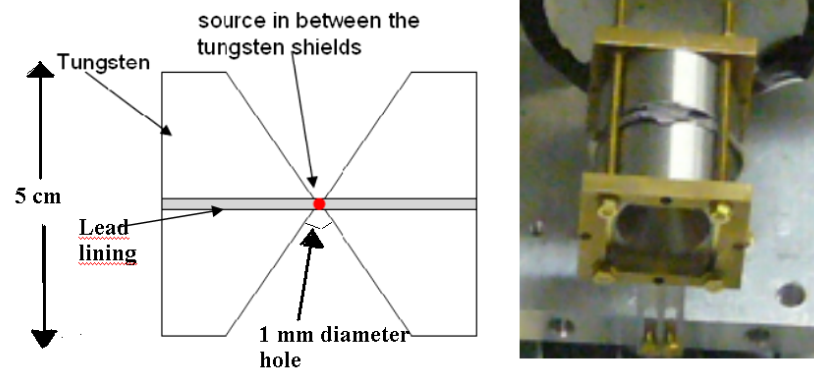


Figure 3.7.: ^{22}Na source between two tungsten shields.

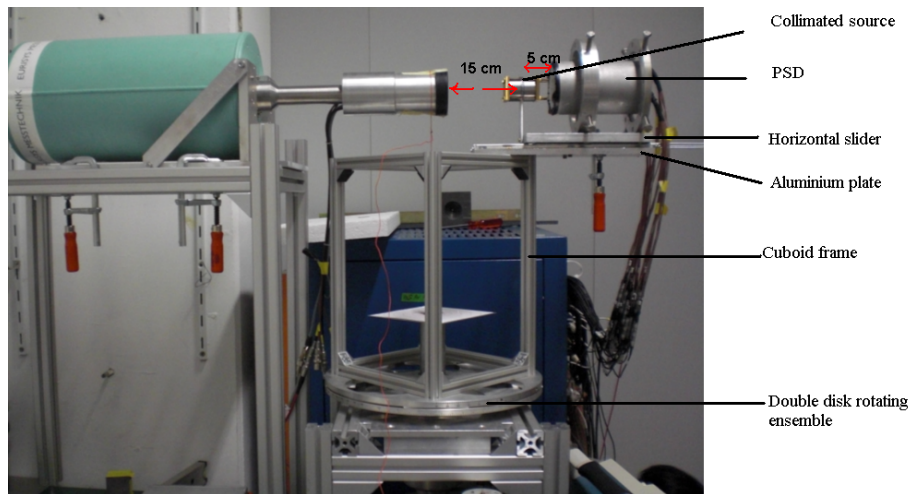


Figure 3.8.: Scanning table with germanium and position sensitive detector facing each other.

3.7. Expected limitations

Attenuation of photons

The intensity of photons, I_0 , entering a semiconductor detector reduces exponentially as :

$$I = I_0 e^{-\mu d}, \quad (3.3)$$

where, I is the intensity after traveling through a detector layer of thickness d and μ is the linear attenuation coefficient. The mean free path is the average distance a photon can travel in the detector before an interaction occurs. It is given by the reciprocal of

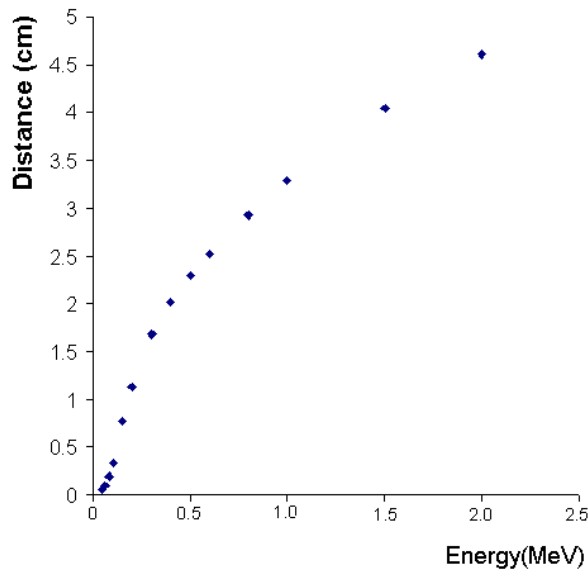


Figure 3.9.: Variation of the mean free path in germanium as a function of gamma ray energy.

the linear attenuation coefficient. The variation of the mean free path in germanium with gamma ray energy is seen in Fig. 3.9. For 511 keV photons, the average distance before the first interaction (Compton scattering) occurs is 2.3 cm. Therefore, if the detector is very long ($\approx 6-8$ cm), the number of photons that can reach the rear part after a number of Compton scatterings reduces considerably, typically by a factor of 40.

Multiple Compton scattering

Another important parameter is the probability of 511 keV photons undergoing two or more interactions due to multiple Compton scattering inside the detector or segment volume. Figure 3.10 shows examples for possible interaction sequences of an intermediate energy (10 keV - 1 MeV) photon inside a germanium detector. At a certain position (highlighted by the red circle), addition of energy from Compton scattered energy of different gamma ray events can appear as fake single interaction event. However, the PSC method effectively filters out most of the pulses arising from the multiple-hit events which lead to a rather particular trace which is composed of several hit contributions.

Background

A real coincident event is the one in which the PSD and germanium detectors are triggered by the 511 keV photons from the same event. A ^{22}Na source also emits 1274 keV gammas in coincidence with 511 keV photons. It is possible that for an event, PSD registers a 511 keV γ ray event and at the same time, the HPGe is triggered by a 1274 keV photon from ^{22}Na source. However, such events can be effectively suppressed by selecting an energy window on the photopeak of the pulse height spectra of both the

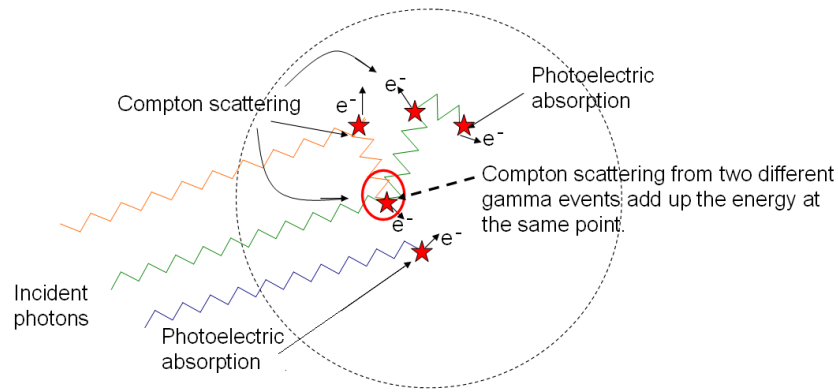


Figure 3.10.: Sequence of interactions of intermediate energy photons in a HPGe detector.

detectors. Still, there is a relatively small chance of random coincidences (within such selected photopeak windows). This contribution can be from other natural or artificial radioactive sources present or from back scattered events from the surrounding matter like walls, supporting structure of scanning table, etc. The Compton scattered events of the 1274 keV state within the HPGe can also add up to the background.

4. Gamma Camera

Position sensitive scintillator detectors/gamma cameras find widespread application in the fields of nuclear medical imaging, atomic and particle physics [37]. Several types of PET (positron emission tomography), SPECT (Single photon emission computed tomography) scanners have been proposed and developed using PSDs [38, 39, 40].

4.1. Principle

Position sensitive scintillation detectors localize the scintillation-light flash created within the crystal. As explained in chapter 2, a scintillation detector consists of a scintillating crystal, which is optically coupled to an electronic light sensor such as a photomultiplier tube (PMT) or a photodiode. Position sensitivity in a scintillation counter can be achieved by coupling either large inorganic continuous scintillator crystal or highly segmented scintillator crystals to the position-sensitive photomultiplier tube (PSPMT). The method is simple to implement because no additional instrumentation is required. The light generated by the gamma interactions in the crystal is sensed by the position sensitive photomultiplier tube. The two dimensional position of each event across the area of the crystal is deduced by an appropriate weighted mean of the individual photo detector signals. The crystal segment size, type of scintillator (section 4.2), structure of photomultiplier (section 4.3), the readout method (section 4.3) and the position reconstruction algorithm (section 4.9) play an important role in determining the spatial resolution of the detector. The resolution achieved at the border of the scintillation crystal is further limited by the light reflections from its edges. Because of these reflections, the effective detection area of the scintillation crystal is smaller than its actual size. Best spatial resolution is achieved when the crystal cross-section is larger than the effective photocathode area and the shape of the photocathode is identical to the crystal. In addition, reflections from the crystal surface deteriorate the position resolution by providing wrong interaction sites at the surface of the PMT photocathode.

The use of thick crystals result in higher detection efficiency but on the other hand, it degrades the intrinsic spatial resolution because of parallax errors. This error is the wrong assignment of gamma ray interaction positions coming from the depth component. It can be corrected by measuring the depth of interaction as well as the two dimensional location of photon interaction.

Further, the photocathode surface has different electron emission efficiency at different

wavelengths. This is known as the quantum efficiency of the photocathode. Hamamatsu R2486 PMT used in the scanner has 23% maximum quantum efficiency at 400 nm.

4.2. Choice of the scintillation-crystal material

Scintillators are characterised by their stopping power, their light yield, the wavelength of the emitted light, and the time over which the light is produced. The factors are important in choosing a scintillator for particular applications. For our purpose, the scintillator must be a dense material that can stop a large fraction of the incident 511 keV photons. Dense, inorganic, solid scintillators are therefore the scintillators of choice. While stopping power is a major factor in the choice of a scintillator, other considerations are also important. The light output of the scintillator (the number of light photons produced per 511 keV interaction) is equally important. A major source of noise in the measurement is the statistical fluctuations in the number of scintillation photons detected. These fluctuations are governed by Poisson counting statistics and reduce as $1/\sqrt{N}$ where N is the number of scintillation photons that are detected. Each scintillating material is most sensitive in a certain range of the incident photon wavelength, which is represented by its spectral response. For an a priori known photon energy which inversely depends on its wavelength, a choice of scintillator can be made knowing its maximum sensitivity wavelength region. Figure 4.1 shows the spectrum of light emitted from some of the commonly used crystal scintillators, like, BGO, LSO, CsI(Tl) in the 400-700 nm wavelength range.

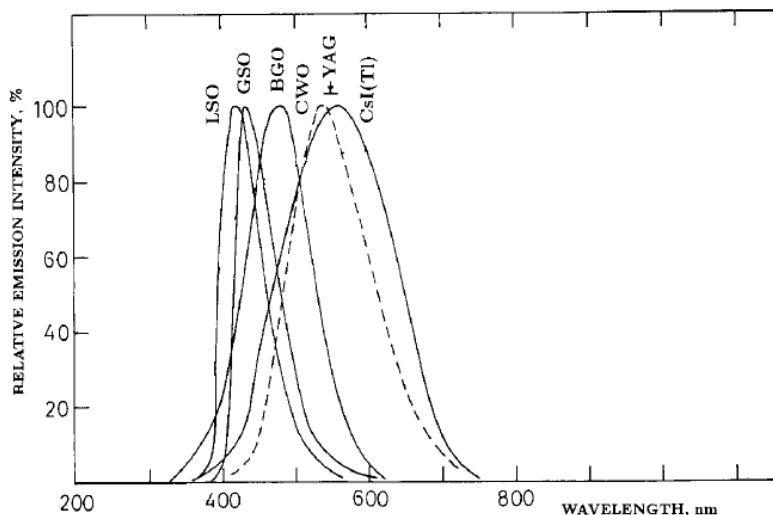


Figure 4.1.: Spectral response of various scintillators [41].

As the principle of the proposed scanner involves the coincident detection of the two

annihilation photons of 511 keV each, it is important to have an accurate assessment of exactly when a photon interacts in a detector. The accuracy of timing is determined in large part both by the decay time of the scintillator and its brightness. A fast, bright scintillator will produce a signal with less timing variation than a slow, dim scintillator. Finally, the index of refraction of the scintillator is also important as this determines how efficiently optical photons can be transmitted from the scintillator to the photo detector. Table 4.1 summarizes the properties of three commonly used scintillators, BGO, NaI(Tl), and LYSO, useful for gamma ray detection at 511 keV photon energy.

Table 4.1.: Properties of scintillator material useful for gamma ray detection at 511 keV.

Scintillator	Density (g/cm ³)	Light output (photons per 511 keV photons)	Decay time (ns)	index of refraction
Sodium iodide (NaI(Tl))	3.67	19400	230	1.85
Bismuth germanate (BGO)	7.13	4200	300	2.15
LYSO	7.4	≈13000	≈40	1.82

LYSO stands for Cerium doped Lutetium Yttrium Orthosilicate. It has a relative light yield of 75% compared with NaI(Tl). It is more than seven times as fast as BGO and more than five times as fast as NaI(Tl). It has the highest density among all three of them. For our application, where we want to detect 511 keV photons with the best possible efficiency and light yield in a short time, LYSO scintillating crystal is an ideal choice. The only disadvantage of using LYSO is that it has a self activity of ≈ 300 counts/s cm³ because of the ¹⁷⁶Lu radioactive component. But in the proposed system, the PSD will always be operated in coincidence with a HPGe detector. This reduces the background coming from self activity.

4.3. Position sensitive photomultiplier tube (PSPMT)

In ordinary photomultiplier tubes, the scintillation light is spread over the entire photocathode. The photoelectrons are amplified by a series of dynodes placed after the photocathode and the information about the point of interaction on the photocathode is lost. However, in some applications, it is important to know the point of origin of the scintillation light arriving at the photocathode. This led to the development of position sensitive photomultiplier tubes (PSPMTs). They have an electron multiplying structure that retain the spatial separation between the electron clouds created by photoelectrons generated at different positions on the photocathode.

Specialized dynode structures have been developed for this purpose. One of them consists of a mesh dynode structure with 12-20 multiplication stages. The charge is multiplied around the original position of the photon striking the photocathode. The output at the last dynode of the PMT is used to trigger the acquisition.

To retain the position information at the anode end, several structures can be used. The most common way to realise this is to use individual anodes or pixels, each with its own readout connection. An array of (8x8) anodes in Hamamatsu H8500 [42] is equivalent of using 64 separate photomultiplier tubes. An alternative method is to use a crossed wire anode configuration as used in the Hamamatsu R2486/3292 family of PSPMTs. Hamamatsu R2486 [43] consists of orthogonal layers of 16 anode wires in X direction and 16 anode wires in Y direction separated by a pitch of 3.75 mm, as shown in Fig. 4.2. In order to make the readout process simple, the wires within each layer are commonly connected via a resistive charge division network. This results in a system with only four signals at the corners making the system compact, simple and cost efficient for electronics. The electron shower arriving at such a resistive network, is shared among the anodes depending on its origin. Using the four distinct analog signals, the centroid of the electron cloud reaching the anodes is determined.

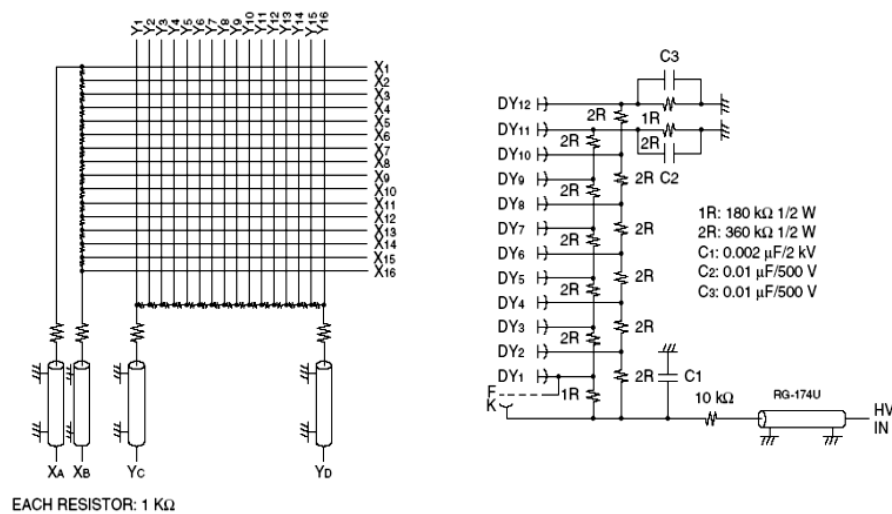


Figure 4.2.: Crossed anode wire structure of the Hamamatsu R2486 position sensitive photomultiplier tube.

The PMT behaves fairly linear in the central region of the crossed anode structure. However since only the centroid of the 4 anode signals is measured, it results in non-linearity in the position coordinates at the edges and hence a distorted image. For Hamamatsu R2486 PMT having a photocathode of 5 cm, it is linear for ≈ 4 cm, leading to a dead zone of ≈ 1 cm. As the individual anode gains are different, the detector system shows a reduced position resolution of $\approx 2 - 3$ mm. The solution to this problem is provided by reading out all the anodes separately, called individual mutlianode readout (IMAR) method. Instead of joining the adjacent anode wires via resistors, they are read out individually. Each anode is independently connected to an amplifier. This allows to measure the charge distribution arriving at each individual anode and hence an accurate determination of the the position of the electron cloud origin at the

photocathode. This approach was first investigated in 1D by A.J. Bird et al. [44] with a Hamamatsu R2487 PSPMT. It has a circular photocathode of 6 cm and an anode structure of orthogonal layers of 18 X and 17 Y wires. It is shown that by individually reading the X anodes, the device is linear for approximately the whole photocathode area and has a position resolution of ≈ 1.5 mm. We further improved this approach by reading all the X and Y anodes of Hamamatsu R2486 PSPMT individually [45] and implementing a more sophisticated position reconstruction approach. A spatial resolution of about 1 mm and a very large field of view of ≈ 28 cm² is measured with the new readout and reconstruction techniques.

4.4. Mechanics of the gamma camera

Our gamma camera is composed of a thin cylindrical LYSO crystal with 76 mm diameter and 3 mm thickness. The flat sides of the crystal are polished, while the lateral side has a rough finish. The lateral side is further covered with black tape to minimise light reflections from that surface. The crystal is optically glued to the surface of a Hamamatsu R2486 PSPMT using silicone glue. The top outer surface of the crystal is covered with enhanced specular reflector (ESR) film [46] to increase the photon collection efficiency. To protect the detector from external light, it is covered all around by black tape. Finally the whole assembly is placed in a cylindrical aluminium housing for better mechanical stability and shielding from external light sources.

4.5. Electronics and data acquisition system used for the performance tests of the Gamma camera

The Hamamatsu R2486 PMT has 32 anodes and a meshed dynode structure. We are using NIM and VME electronics to process the electrical signals from the PMT. The block diagram of the electronics is shown in Fig. 4.3.

The PMT is biased by -1000 V giving anode signals of ≈ 10 -15mV for fully absorbed 511 keV γ -rays in each wire. The raw PMT signals are amplified using two 16 channel fast amplifiers, N979 NIM modules [47] from CAEN. They have a gain of 10. The amplified anode signals are AC coupled into a 32 channel V792 Charge-to-Digital Conversion (QDC) [48] VME module from CAEN,(see Fig. 4.3). It has an input range of 0 to 400 pC and a digital resolution of 12 bit. To overcome the problem of background coming from self activity, the acquisition system is always run in coincidence with a reference detector (detector 2 in Fig. 4.3) like e.g. NaI, Plastic, BGO, HPGe detector. Placing the ²²Na source in between the two detectors, the QDC records the pulse height spectrum of the 32 anodes only for coincident events between the PSD and the reference detector. The dynode signal from the PSPMT is used to make these

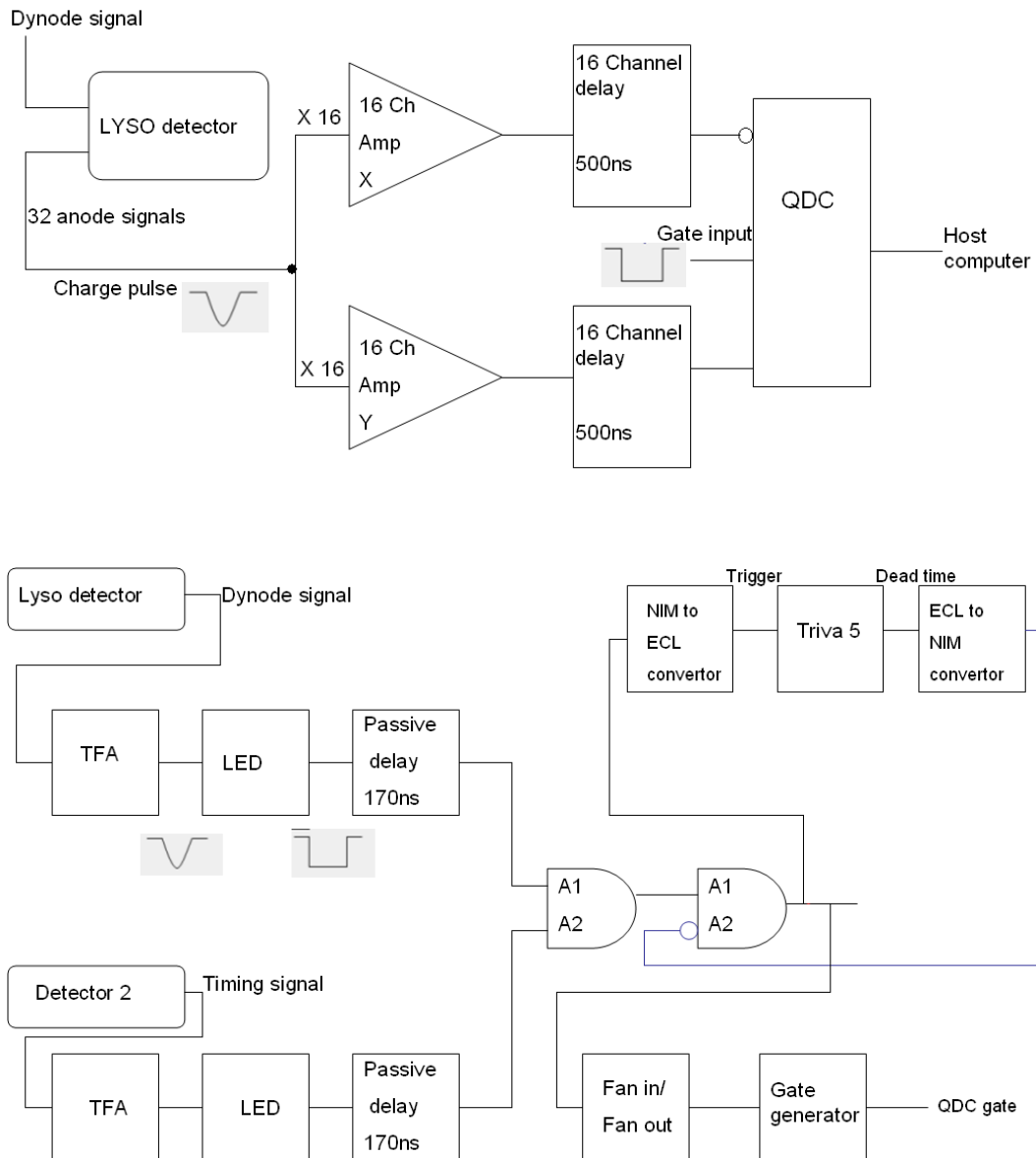


Figure 4.3.: (Top) Block diagram of the electronics employed for reading the 32 anodes of PSPMT. (Bottom) Electronics block diagram showing the trigger gate signal formation for the QDC.

coincidences. After shaping the dynode signal using an Ortec 454 timing filter amplifier, it is fed to a leading edge discriminator (LED) from LeCroy (model 623B). The fast reference detector is used as trigger detector. The signal from this detector is also given to a discriminator after being amplified. The two output NIM signals from the LEDs are fed into a coincidence unit manufactured by GSI. The logic output pulse from this coincidence unit had a width of about 400 ns. Before feeding this logic pulse to the QDC gate input, it is made sure that all the 32 anodes signals arrive within the

gate time window. The same logic output is used to trigger the acquisition system via a TRIVA module [49]. The TRIVA unit triggers the acquisition only when the logic pulse from the desired coincidences occurs in anti coincidence with system dead-time. The Multi Branch System (MBS) [50], which is the standard data acquisition system at GSI, was used to read out the QDC channels. The online analysis is done using the GSI object Oriented On-line off-line system (Go4) [51] which is based on the ROOT [52] package of CERN.

4.6. Anode gain calibration

The gain of each individual anode is different (Fig. 4.4 top) and therefore, a procedure is applied in order to calibrate them and obtain a homogeneous response.

To this aim, the PSD and reference detector are fully illuminated with a 300 kBq ^{22}Na source. The acquisition is run in coincidence with the reference detector. This eliminates the background due to LYSO self activity and reduces the false coincidences due to 1274 keV gammas. The pulse height spectra (PHS) of the individual anodes are recorded with good statistics. If the gain of all the anodes is the same then the PHS for all of them should be the same. However, the measured spectra showed gain variations as large as 40% (Fig. 4.4, top). If these anode pulse height spectra are used to reconstruct the (x,y) coordinates, the resulting image will be distorted and will considerably reduce the position resolution of the system. Since the anodes were read out individually, it is possible to do a gain calibration of all the 32 anodes. When a gate signal is applied to QDC, it produces a signal even when no input is present. This is called QDC pedestal and this value has to be first subtracted before doing the gain calibration. The high energy region of each resulting PHS is used to determine the corresponding calibration factor. The anode PHS with lowest gain is taken as reference and the rest 31 anode PHS are compared to it on the basis of a χ^2 minimisation test in the specified energy channel range. This region mostly corresponds to the fully absorbed 511 keV events. The calibrated PHS spectra for the 16 Y anodes are shown in the bottom panel of Fig. 4.4.

Although the gain calibration done for the 32 anodes is quite stable, it might change due to some fluctuations in the electronics. It is thus needed to be checked on a regular (monthly) basis. The position sensitive detector is completely operational. The performance of this calibrated position sensitive γ -ray scintillator detector (PSD) has been studied in detail and optimised. A variety of algorithms for reconstructing the energy and position of each event using the individual anode readout method are described in the following sections. The aim of these tests is to enhance the spatial resolution, linearity and field of view. It is important to optimise the PSD for these properties as the scanner performance is strongly dependent on the performance of the PSD.

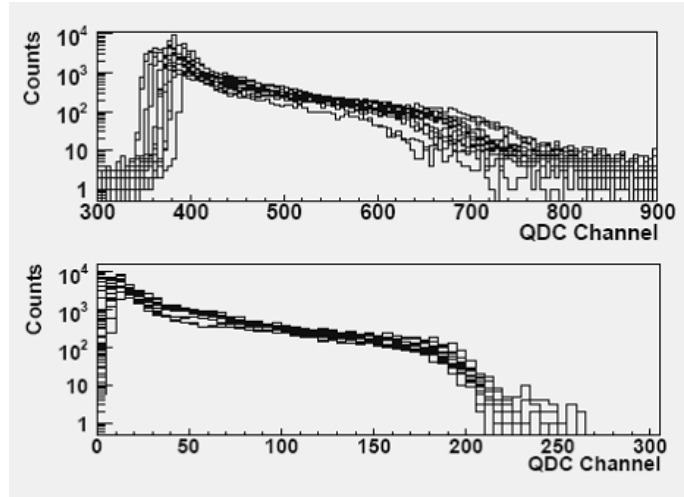


Figure 4.4.: (Top) raw QDC pulse height spectra from the 16 Y anodes. (Bottom) Calibrated pulse height spectra.

4.7. Experimental set up for position reconstruction studies

For position reconstruction studies, the ^{22}Na source is collimated using a lead block of 5 cm thickness, having a hole of 1 mm (Fig. 4.5). The surface of the photocathode $[\pm 30, \pm 30]$ mm is scanned in steps of 10 mm near the central region. Towards the border of the photocathode, the scanning step size is reduced to 5 mm. The various positions scanned are shown in Fig. 4.6. The scanned points shown outside the black circle are outside the active photocathode area. The scanned positions defined on the LYSO surface have some inherent uncertainty. This is because of the finite size of the collimator which is 1 mm and the projected divergence of the collimated beam. The crystal area which is exposed for a particular position of the collimator depends on the LYSO-collimator distance. In order to have a narrow beam spot, the collimator is placed very close to the crystal surface. The gamma rays that interact with the scintillation crystal will originate isotropic scintillation light, whose spatial distribution is projected on to the sensitive area of the photo cathode.

4.8. Measured light distribution

For each event, the QDC integrated anode currents, give the corresponding charge deposited at the anodes. Eventwise two 16 bin histograms are created for X and Y anodes, with each bin corresponding to one anode. After applying the gain calibration of all 32 anodes, these histograms are filled with the anode charge distribution on an

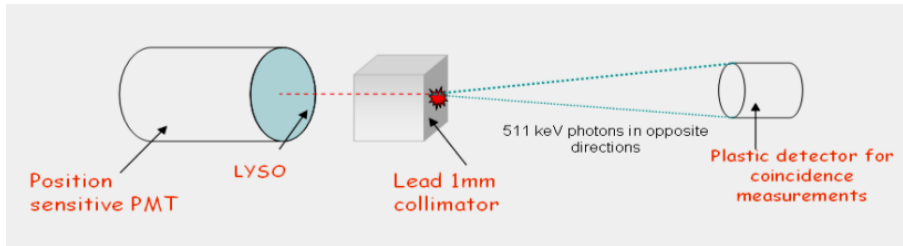


Figure 4.5.: Experimental setup for position reconstruction measurements.

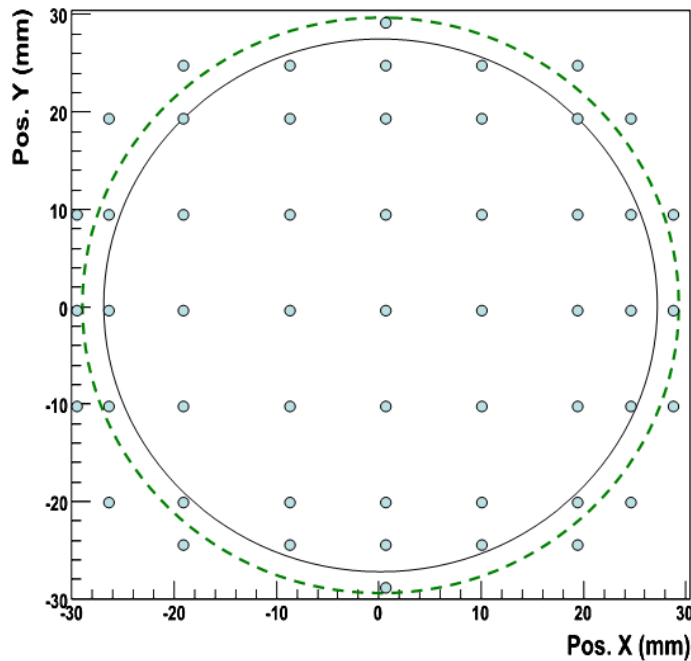


Figure 4.6.: Pattern of the positions where the measurement is done with the collimated source (observe the closer spacing at the edges). The Solid circle indicates the minimum size of photocathode and the dashed circle represents the extended anode grid.

event by event basis, each bin containing the charge deposited at that particular anode. Figure 4.7 illustrates some examples of anode charge distribution histograms for various collimated positions. Histogram (a) is for the collimated source position near the center of the photocathode. In this region the charge distribution is quite symmetric. However, for the source positions towards the border of the photocathode, the charge distribution is asymmetric. This is shown in Fig. 4.7(b). Only a part of the scintillation light is inside the active photocathode area for these positions. The shape and width of the measured charge distributions remains also approximately the same for the events at the central region of the photocathode. Towards the corners, the charge distributions are also a bit broader due to the reflections at the edges of

the scintillation crystal.

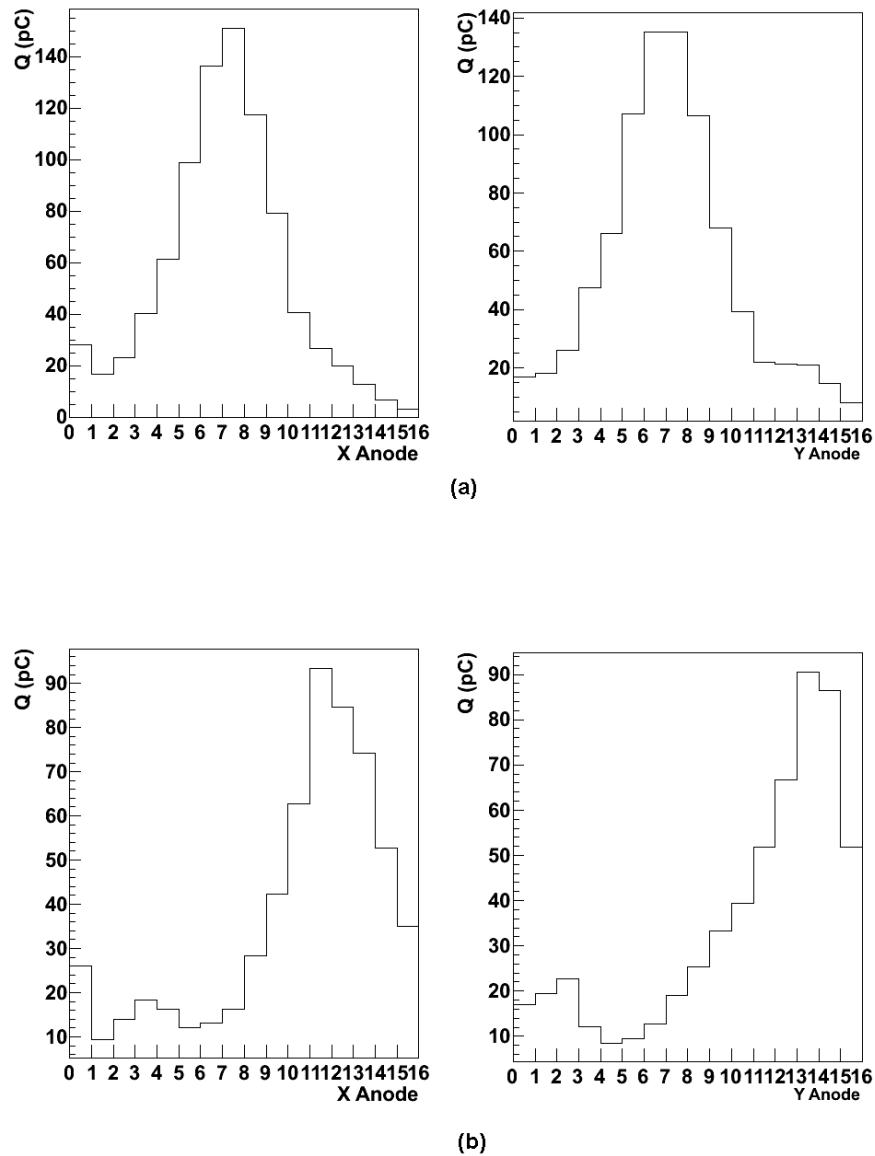


Figure 4.7.: The charge distribution profile for X and Y anodes for an interaction position close to the center (a) and a position close to the edges of the crystal (b).

4.9. Position determination

The readout method of the photomultiplier tube plays an important role in achieving good spatial resolution in a scintillator detector. In addition, the algorithm employed

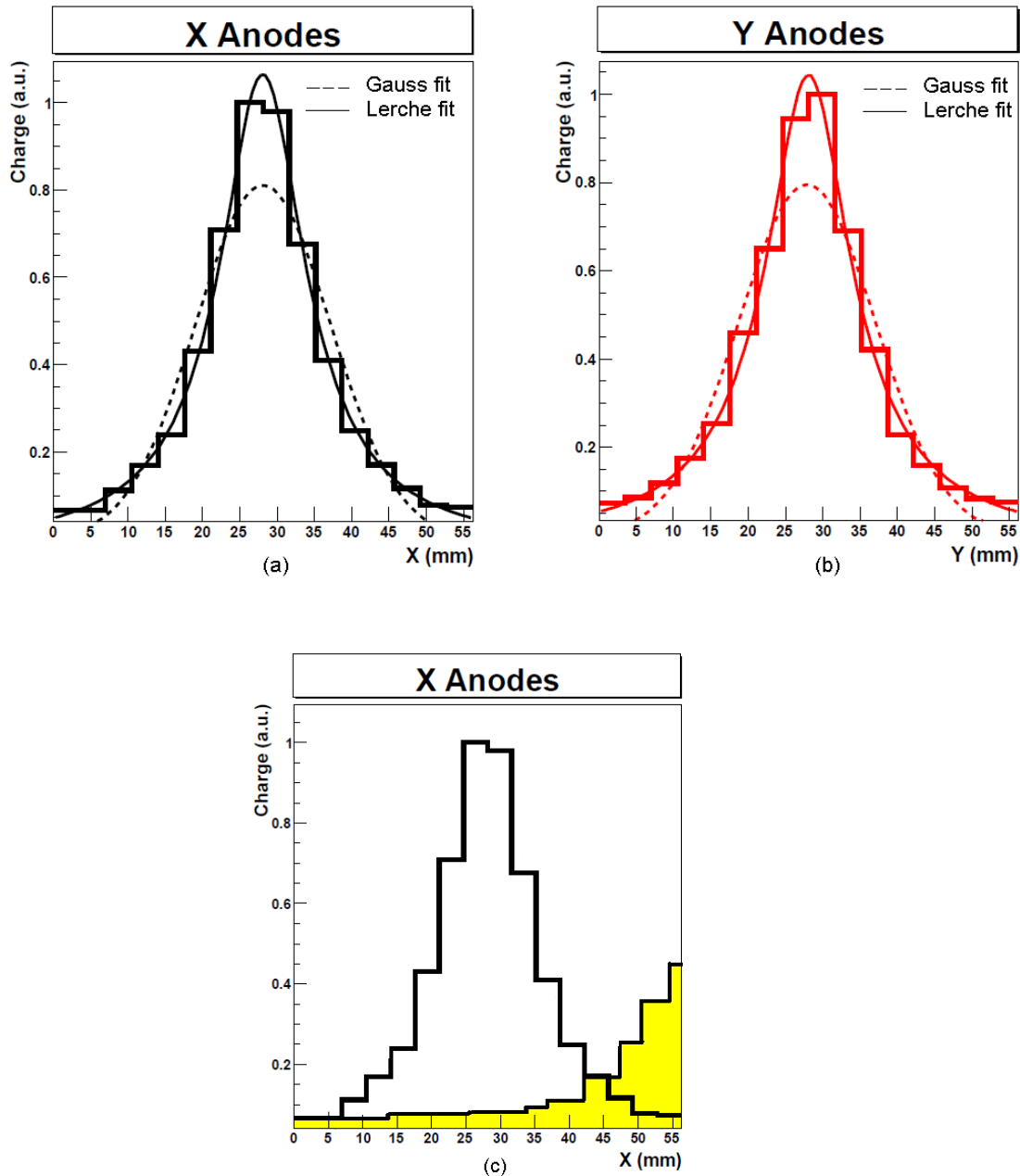


Figure 4.8.: Charge distribution of X anodes (a) and Y anodes (b) for an event at the centre of the photocathode. The shaded distribution in panel (c) represents an event occurring close to the edge of the photocathode. A fit of Gaussian function (dashed line) and the formula of Lerche (solid line) is shown.

to reconstruct the interaction position coordinates strongly effects the position resolution.

The charge profile for X and Y anodes for an event, when the collimated source is

placed in front of the center of the photocathode, is shown in Fig. 4.8 (a and b). As reported in Ref [45], three algorithms are investigated to get the position information from the charge distributions. The first is a simple centroiding method which is analogous to the conventional hardware system implemented in resistive network devices. It determines the centroid of the charge distribution to obtain the (x,y) coordinates of the interaction position. The second method employed is to fit the charge distributions with a symmetric function like a Gaussian. The peak position of the Gaussian fit for both X and Y anodes gives the position (x,y). The third algorithm is based on a pattern fitting approach. An average charge profile is created from the average of a large number of charge distributions at the centre of the photocathode. This average charge profile is then fitted using a realistic scintillation light distribution model reported by Lerche [53] and stored in a fine binned (0.05 mm) numerical pattern. The Lerche model precisely reproduces the light distribution which we measure as shown in Fig. 4.8 by the solid line. It assumes scintillation light emission from a point like source, which is distributed spherically and obeys geometrical optics as well as the inverse square law. An exponential factor is added to take into account the absorption and scattering along the light path. A constant τ is also included for the background caused by the photons scattered from the surface. Thus the spatial dependence of the light distribution at an observaion point \vec{r} goes as,

$$L(\vec{r}) = \frac{L_0}{(\vec{r} - \vec{r}_0)^2} \alpha e^{\alpha|\vec{r} - \vec{r}_0|} + \tau, \quad (4.1)$$

where $L(\vec{r})$ is the intensity at an observation point \vec{r} , α is the absorption coefficient for the scintillation light and L_0 is the intensity of the source, \vec{r}_0 is the coordinate for the photon interaction position inside the scintillator. Since the surface of the photocathode lies outside the scintillator at a fixed distance of few millimeters, \vec{r} is never equal to \vec{r}_0 . This avoids the singularity of the above equation at $\vec{r} = \vec{r}_0$. Further the formula given by equation (4.1) is integrated along one direction (x or y) in order to account for the detector response of crossed-wired PSPMT. The integration along one of the space directions gives the charge at a position x (or y) [54],

$$J(x) \approx J_0 \alpha \frac{e^{-\alpha\sqrt{(x-x_0)^2+d^2}}}{\sqrt{(x-x_0)^2+d^2}} x \quad (4.2)$$

$$\left[\tan^{-1} \left[\frac{\frac{b}{2} - y_0}{\sqrt{(x-x_0)^2+d^2}} \right] - \tan^{-1} \left[\frac{\frac{b}{2} - y_0}{\sqrt{(x-x_0)^2+d^2}} \right] \right] + T, d > 0$$

$$T = \int \tau dx \quad (4.3)$$

where, J_0 is the magnitude of the maximum charge at position (x_0, y_0) , b is the size of

the crystal and $d = (z - z_0)$ is the depth of interaction. Since in our case, the crystal is thin, the effect of this factor is negligible.

For each measured event, when charge distribution is measured for any location on the photocathode surface, it is compared with the stored numerical pattern. The relative position of the pattern is varied until it matches with the measured charge distribution using a χ^2 minimisation. This procedure is illustrated by an example in Fig. 4.9.

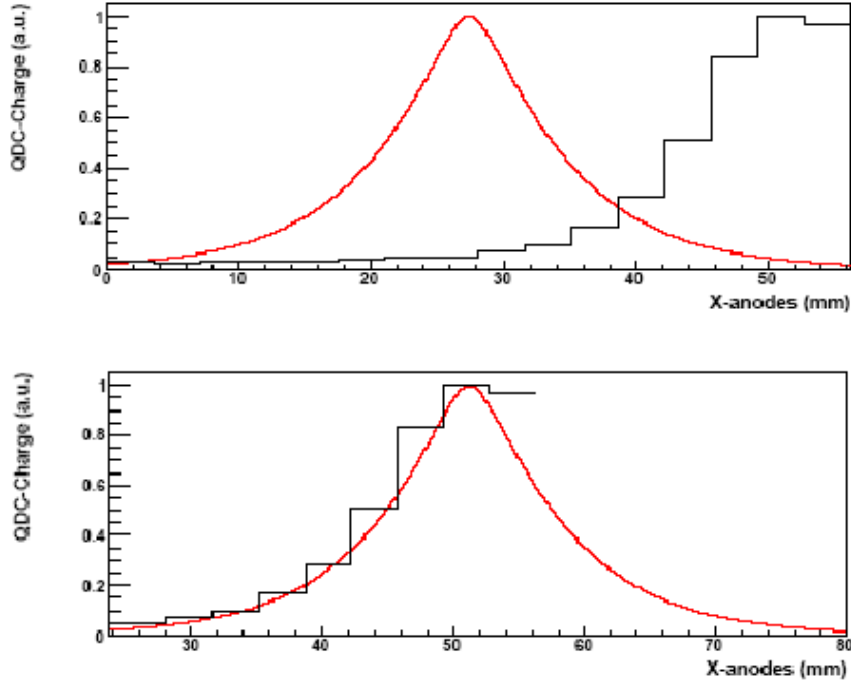


Figure 4.9.: An example showing the position determination using the pattern fitting approach. The measured charge profile is shown in black while the average pattern for the centre is shown in red. (Top) Charge profile for an event near the border of the photocathode. (Bottom) The relative position of the average pattern is varied till it matches the measured charge profile.

A comparison of the three methods applied for all the scanned positions of the LYSO crystal is shown in Fig. 4.10. The charge distributions near the center of the photocathode are symmetric, therefore the above mentioned algorithms in this region work quite well. However, towards the border of the photocathode, the scintillation charge profile is near the edge and we measure only a part of it (Fig. 4.7 (b) and (d)). Also the distribution is broadened because of light reflections from the crystal edges. The mean of the measured distribution in this case will be different from its maximum. The peak position of the Gaussian fit for the truncated charge distribution will also deviate from the real position. These two effects result in non-linearity in the position distribution near the edges of the PMT, which is evident in panel (a) and (b) of Fig. 4.10. The measured (x,y) coordinates deviate from the real (x,y) coordinates

considerably near the extreme anode wires at $[\pm 28.125, \pm 28.125]$ mm. These points correspond for example to reconstructed values of $[\pm 25, \pm 25]$ mm.

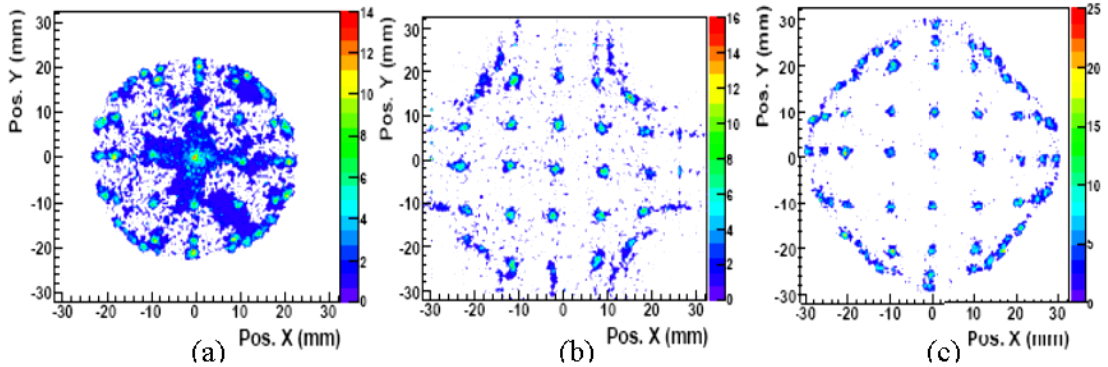


Figure 4.10.: Two dimensional histograms showing reconstructed position variables (x,y) for the scanned positions indicated in Fig. 24. (a) Centroiding approach (b) Gaussian fitting approach (c) Pattern position fitting approach.

With the pattern fitting approach, the interaction positions are determined with better accuracy, which is evident from panel (c) in Fig. 4.10. Also the system behaves linear for 50 mm along the photocathode, in both X and Y directions. The interactions at the last anode wire, which is at $[\pm 28.125, \pm 28.125]$ mm from the photocathode are also reconstructed by the fitting algorithm. Here the positions distribution is a bit wider as compared to the central region of the crystal because of reflections from the edges.

4.10. Enhanced Field of view

The Field of view (FoV) is the effective area of the position sensitive detector for which its behaviour is linear. An enhanced FoV, approximately equal to the photocathode area, is obtained by extracting the position information using the IMAR method in combination with the pattern fitting approach. The scintillation light cone after the crystal activation has spherical projection. Even when the interaction is outside the active photocathode surface, a part of the light cone illuminates the photocathode (Fig. 4.11). In these γ -ray interactions only the tail of the charge distribution is measured but this information is still sufficient for the pattern fitting algorithm to reconstruct the maximum of this charge distribution. It is assumed that the amplitude of the scintillation light distribution is constant throughout the crystal. This will in turn give the interaction positions even for the points which are not covered by the anode grid of the photomultiplier tube. The extreme points which are visible along the X and Y axes in panel (c) of Fig. 4.10 are 30 mm away from the centre of the photocathode, and about 2 mm beyond the last anode wire. So the effective field of view is $\approx 28 \text{ cm}^2$

for a circle of 60 mm diameter compared to $\approx 4 \text{ cm}^2$ for the centroiding approach. However for our purpose we restrict ourselves to the field of view of 20 cm^2 for 50 mm diameter circle, where the system is completely linear.

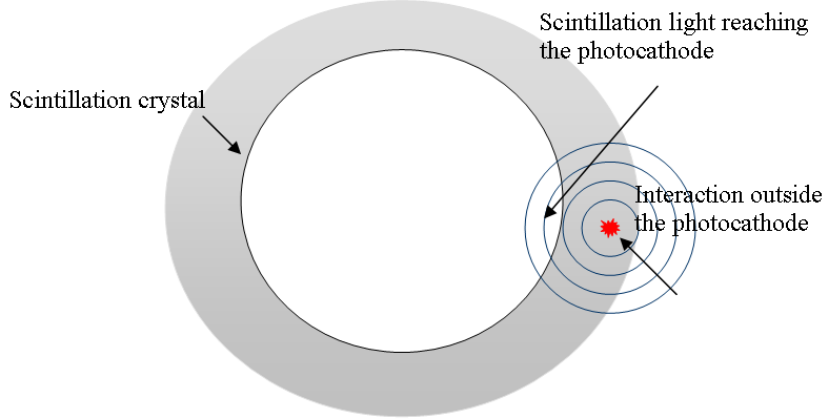


Figure 4.11.: Pictorial representation of an event occurring outside the photocathode surface. The light cone of scintillation still reaches partly the anode grid making it possible to reconstruct these events using the pattern position fitting approach.

4.11. Resolution and efficiency of the gamma camera

The same experimental set up as shown in Fig. 4.5 is used to determine the resolution of the position sensitive detector. The ^{22}Na source is collimated using a lead collimator with a hole of 1mm diameter. The positions are reconstructed using the IMAR pattern fitting approach and an example of the position distribution along x and y, when the source is placed in front of the centre of the photocathode, is shown in Fig. 4.12. The photocathode is scanned for points separated by 5 mm for two vertical lines in the range of -25 mm to 25 mm (Fig. 4.12). We measured an average FWHM = 0.91 ± 0.08 mm and 0.98 ± 0.08 mm along the X and Y axis of the PSPMT respectively (Fig. 4.12). The 1 mm collimator size contribution to the beam divergence has been unfolded while calculating the average FWHM values. The image resolution (IR) is a measure of the quality of an image. The IR of our detection system can be approximately quoted as $\text{IR} = \text{FoV}/\Delta r$, where Δr stands for the average spatial (FWHM) resolution in the linear region. With the large FoV and the excellent position resolution of our detector we obtain a value of $\text{IR} \approx 2000$ pixels, while a conventional RN-based system would yield an image resolution of $\text{IR} < 800$ pixels only.

The average efficiency of the PSD for 511 keV γ -rays is experimentally determined as $7.5 \pm 1.5\%$ for events which deposit their full energy inside the crystal. The total

γ -ray interaction efficiency for an energy threshold of 70 keV is measured to be $19 \pm 4\%$. The efficiency remains constant over the effective surface area of the PSD.

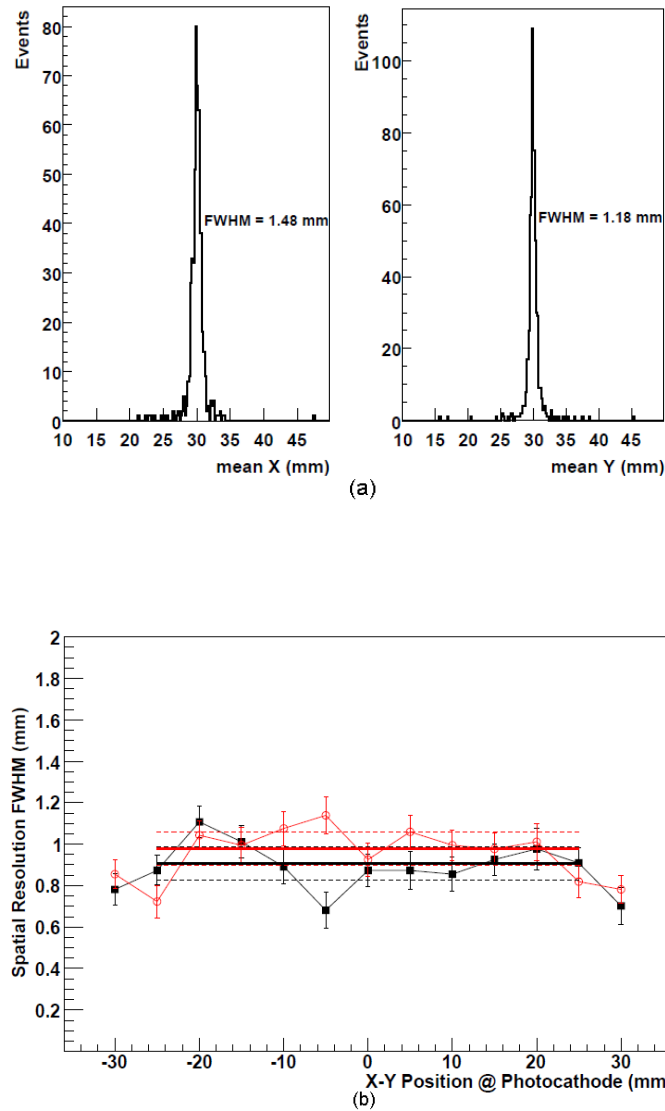


Figure 4.12.: (a) Position resolution on X and Y anodes for a 1mm collimated source placed at the center of the photocathode (b) Spatial resolution (FWHM) measured for X axis positions (black squares) and Y axis positions (red circles).

4.12. Position calibration using imaging techniques

The gamma camera shows a remarkable spatial resolution and a very large field of view using the IMAR method and the pattern position fitting approach [45]. After its

characterisation, the PSD is placed in the scanning system as shown in Fig. 4.13. The ^{22}Na source is at a fixed distance of (5.5 ± 0.5) cm from the surface of the PSD. The central axis of the scanning system is at a distance of (15 ± 1) cm from the source (black square plate in Fig. 3.8). The symmetry axis of the germanium detector to be scanned is usually not known precisely and will be placed to approximately coincide with the axis of the system. As explained before, the reason to choose this distance is to have approximately 20 kHz event rate in a large germanium detector for a 300 kBq ^{22}Na source. The image size of the detector to be scanned depends on its distance to the source and varies with the interaction depth due to the 3D spatial occupancy of the detector volume. In order to get an image as close as possible to the real object, a position calibration method has been developed [55].

4.12.1. Gamma ray imaging and position calibration

To perform the position calibration, a (11×11) cm² regular steel grid with 2 mm thick grid lines separated by 1.0 cm (see Fig. 4.14) is placed in front of the source and PSD detector assembly. It is made sure that the central axis of the grid coincides with the central axis of the scanning table. This grid serves as reference object and the aim now is to get an image of it in the PSD and hence to determine the correspondence between the real (x_r, y_r) and measured (x_m, y_m) positions of the grid crossing lines. To get the image of the steel grid, a γ -ray scattering technique [35, 36] is exploited. For 511 keV γ -rays from the ^{22}Na source, the dominant mode of interaction in steel is Compton scattering. For an event, two 511 keV photons are emitted by the ^{22}Na source in opposite directions. One of it is detected in the PSD and the other photon goes to the grid and gets Compton scattered off it. Two large NaI(Tl) detectors are placed on either side of the grid to register scattered gammas from the grid at sideward angles (see Fig. 4.15).

The acquisition system is triggered to register coincident gammas in the PSD and the NaI detectors. For a particular event only one of the NaI is activated depending on the direction where a photon gets scattered off the grid. An image is reconstructed using the coincidence events for this setup and applying the pattern fit position reconstruction algorithm described in section 4.3 (see Fig. 4.16).

For each real position coordinate (x_r, y_r) , there corresponds a measured position coordinate (x_m, y_m) on the image of the grid. For example, the measured position coordinates of the point marked in Fig. 4.17, are (4.31, 4.30) mm, which in real space correspond to (10.0, 10.0) mm. Such compression of the measured positions is ascribed to the optics of the system, where the grid-source distance is approximately 3 times the source-PSD distance.

A position calibration of the gamma camera is to be performed to obtain an image as close as possible to the real object. The exact functional relationship between the measured points and the real points is not known, but it depends on the linearity of the

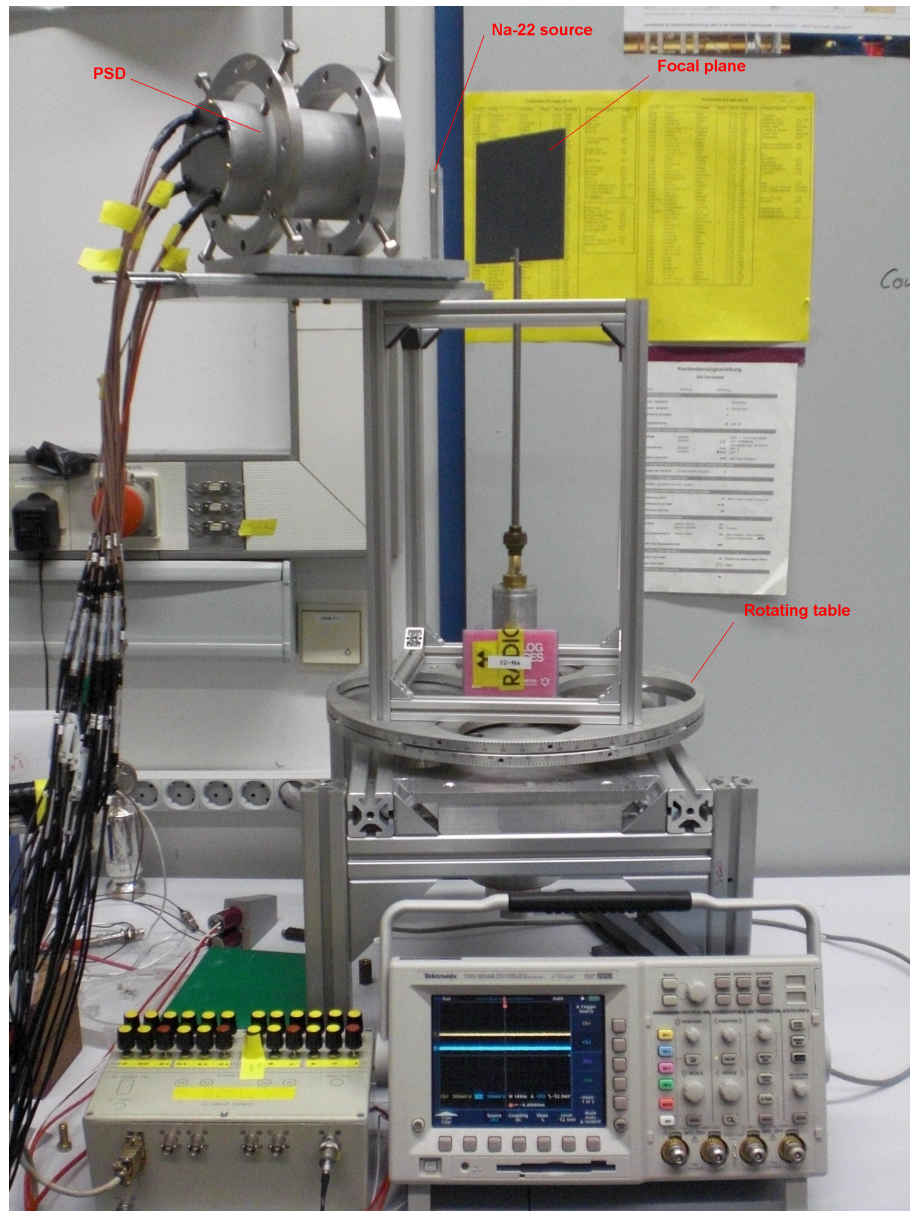


Figure 4.13.: The Gamma camera mounted on the scanning mechanics.

system and also on the source-PSD distance. One possible way of solving the problem is to find an expression which reliably approximates the dependence of the real position coordinates on the measured ones. The positions given by the crossing points of two orthogonal grid lines are used for the position calibration. For each measured position on the grid, the corresponding real coordinate is known. The behavior of the system can be described by two functions f and g of measured positions, which approximates them to the real ones,

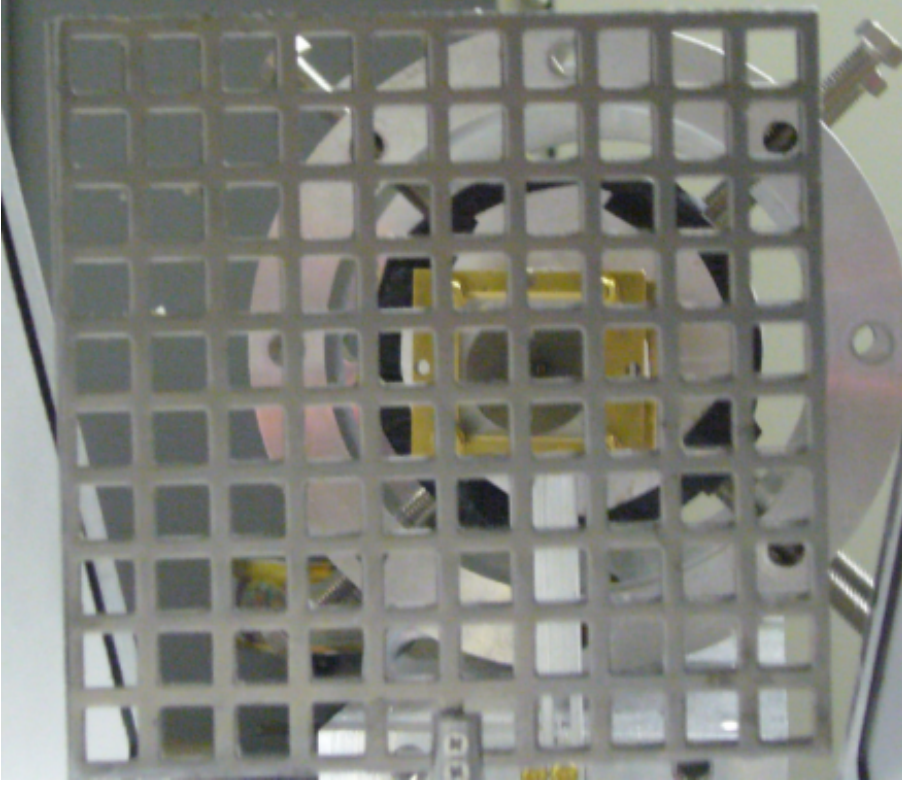


Figure 4.14.: (11 x 11) cm² steel grid in front of the ²²Na source.

$$f(x_{mi}, y_{mi}) = x_{ri} \quad (4.4)$$

$$f(x_{mi}, y_{mi}) = y_{ri} \quad (4.5)$$

where $i=1, \dots, S$, S is the number of measured points on the grid. We used a position reconstruction method based on a 2D polynomial functional fit to the measured data.

$$f(x_m, y_m) = \sum_{j=1}^M C_j x_m^{a_j} y_m^{b_j} \quad (4.6)$$

$$g(x_m, y_m) = \sum_{j=1}^N D_j x_m^{c_j} y_m^{d_j} \quad (4.7)$$

Where C_j , D_j , a_j , b_j , c_j and d_j are the coefficients. Different degrees (values of M and N) of the 2D polynomial fit are checked to obtain the best agreement between (x_r, y_r) and (x_m, y_m) . We used $M = 20$ and $N = 20$. The measured positions are fit using these

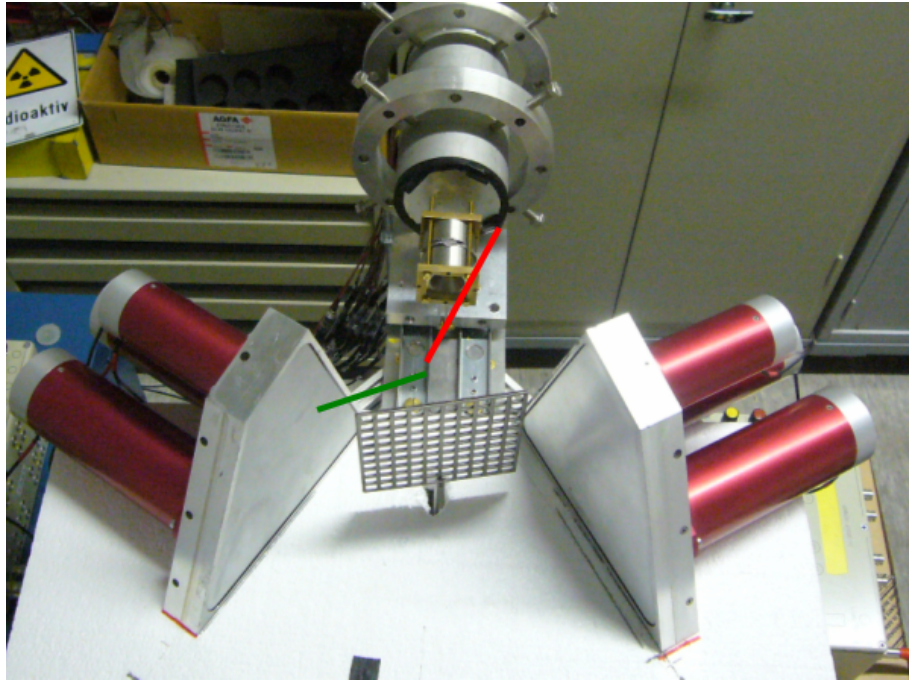


Figure 4.15.: Setup for the imaging of the grid. NaI(Tl) detectors are placed at sideward angles to register the gammas scattered off the steel grid.

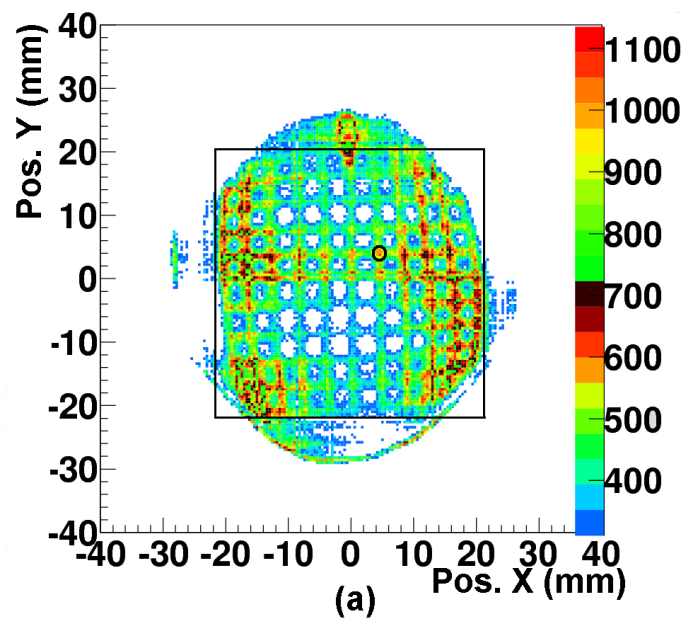


Figure 4.16.: Image of the grid obtained with the position sensitive detector using the pattern fit algorithm.

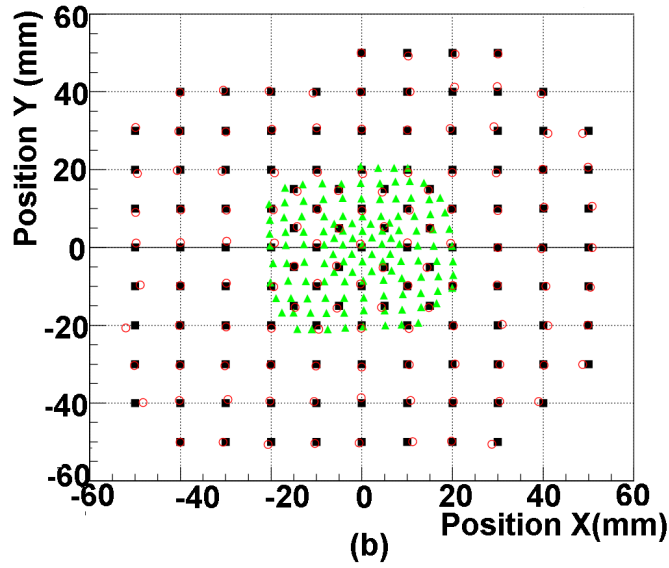


Figure 4.17.: Reconstruction of measured positions by applying two-dimensional functions.

two dimensional functions to get them match with the real position coordinates. To fit the data, the CERN ROOT class `TMultiDimFit` [52] is used. Figure 4.17 plots the reconstructed positions (red circles) when the analytical functions f and g are applied to all the measured points (green triangles).

4.12.2. Position Calibration for different points in space

The position calibration method explained above is first applied to the case when the steel grid is parallel to the surface of the PSD. The calibration done for this configuration is equivalent of doing a calibration for points along any plane as shown in Fig. 4.18 inside the germanium detector. In order to get more calibration points spaced between the points measured for first position, the grid is rotated in steps of 10 degrees for 4 angles and the same measurement (as demonstrated above) is done for each angular position of the grid.

When the grid is rotated by an angle θ , the position coordinates (x'_r, y'_r) in the rotated frame are given by:

$$x'_r = \frac{D_{SG}x_r \cos \theta}{D_{SG} - x_r \sin \theta} \quad (4.8)$$

$$y'_r = \frac{y_r D_{SG}}{D_{SG} - x_r \sin \theta} \quad (4.9)$$

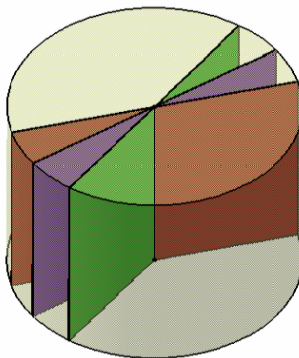


Figure 4.18.: Multiple planes inside the detector volume. Position calibration was done for several planes.

Where D_{SG} is the distance between the source and the grid, which in our case is 150 mm and (x_r, y_r) are the position coordinates before rotation. Figure 4.19 shows an image of the matrix when it is rotated by 40° . The two dimensional functions f' and g' obtained, gave good agreement between the reconstructed and real positions (calculated using equations 4.4 and 4.5) for this set of measurement positions (Fig. 4.20). The maximum deviation (in mm) of the reconstructed positions in X and Y directions are 1.18 mm and 1.03 mm respectively. The corresponding values for mean deviation in X and Y directions are 0.38 mm and 0.59 mm respectively.

Using the positions from all the data sets corresponding to measurements at 0° , 10° , 20° , 40° a global two dimensional reconstruction function is evaluated. This function is able to reconstruct the positions with a maximum deviation of 3.7 mm in X and 2.7 mm in Y direction in the peripheral regions. This concluded the position calibration of the gamma camera for a case when it will shine the germanium detector from the front side. According to the principle of operation of the scanning system (see section 3.1), the source and PSD assembly will be moved by 90° to shine the detector sideways. In principle, the same position calibration should be applicable to this configuration of the system. However, when the same position calibration parameters are applied for the data points measured for the 90° rotated position of the PSD, the reconstruction function is different to the 0° position of the PSD. This can be explained by the change in the mechanical alignment of the PSD when it is rotated by 90° . When the global reconstruction function obtained for the 90° position is applied to the measured data set of the 0° position, we get a maximum deviation of 5.9 mm in X and 2.9 mm in Y, which is greater than the deviations obtained before. So to correct for this inhomogeneity, separate reconstruction functions are used for different angular positions of the PSD at the scanning table.

However it is a temporal problem due to the mechanical inaccuracy of the system. In the upgraded version, it is foreseen to overcome this.

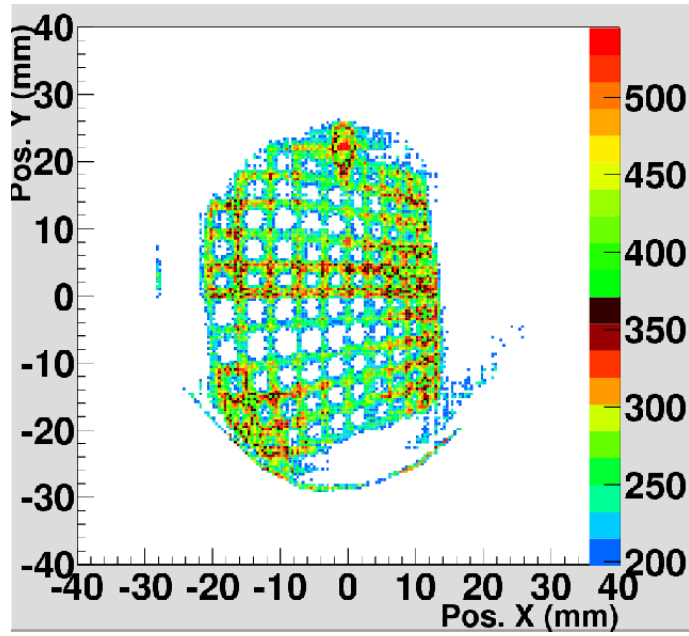


Figure 4.19.: Image of the grid when it is rotated by 40° , obtained with the position sensitive detector using the pattern fit algorithm.

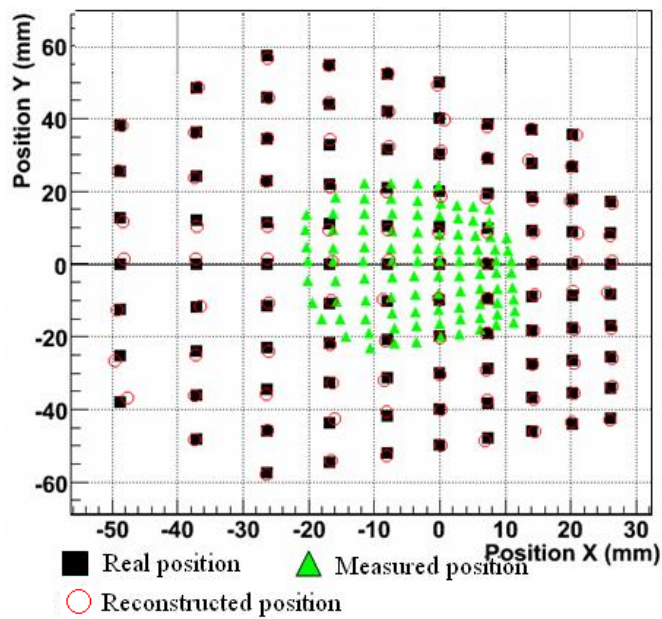


Figure 4.20.: Reconstruction of measured positions by applying two-dimensional functions.

5. Position response of a planar germanium detector

A simple and compact scanner has been designed for measuring HPGe detector pulse shapes as a function of the gamma-ray interaction position inside the detector volume. Since it is based on pulse shape comparison and positron annihilation correlation, it is expected to be much faster than any of the scanning systems presently available. The trajectories of gamma-rays entering the germanium volume are defined by a 2D position sensitive detector (PSD). The PSD system is built with a LYSO crystal and a large area PSPMT from Hamamatsu. It showed a remarkable spatial resolution of ≈ 1 mm (FWHM) and a very large field of view of 28 cm^2 . This is due to the individual multianode readout method and a pattern position fitting approach. The obtained image resolution of 2000 pixels and detection efficiency of 7-19% along with the excellent spatial resolution makes this system the best choice to be implemented in the scanning system. A complete position calibration of the PSD is performed using gamma imaging techniques. All the preliminary tests for the scanning system are finished and it is now ready to be used for scanning of a germanium detector. This chapter reports on the measurements performed on a non-segmented planar germanium detector.

5.1. Experimental setup and the concept of scanning

A 300 kBq ^{22}Na source is placed between the front surface of a planar detector and the position sensitive detector (PSD) as shown in Fig. 5.1(a). The germanium detector is placed at a distance of 15 cm from the source whereas the PSD is at 5 cm from it in order to cover the full surface area of the PSD. The layout of the scanning table is described in section 3.6. The acquisition is triggered by the 511 keV coincident events in the PSD and the germanium detector. In order to avoid any false coincidences because of the scattering from the surrounding matter, the source is shielded by conical tungsten collimators. They collimate the gamma-rays in the field of view of the PSD and in the HPGe detector.

The germanium detector used here, is an n-type cylindrical planar HPGe crystal with 2 cm thickness and 5 cm diameter manufactured by the company Canberra Eurisys [56]. The crystal is housed in an aluminium endcap of 70 mm diameter and 85 mm length. The p^+ contact is negatively biased at 3000 V. A PSC 821-CMS charge

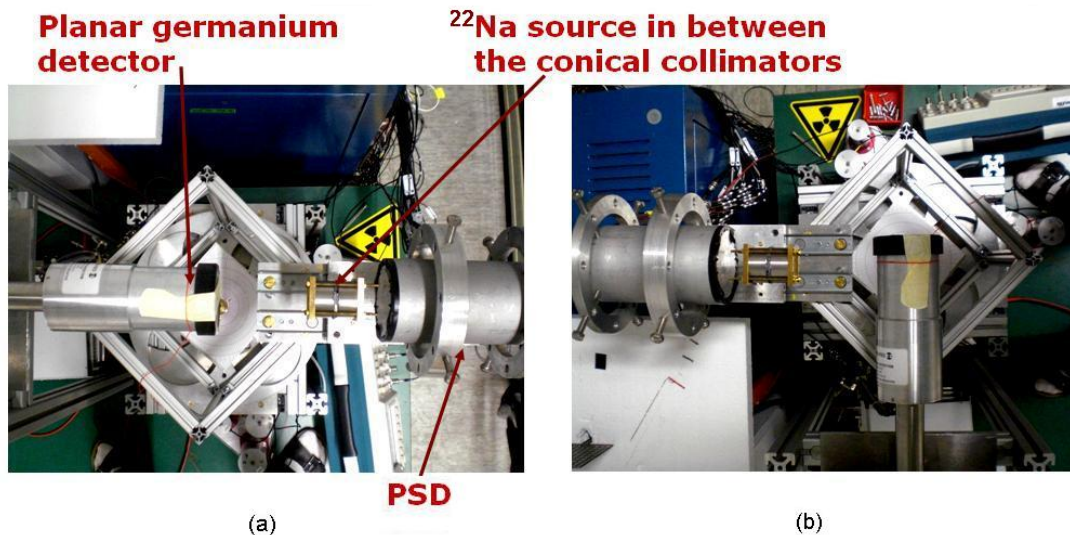


Figure 5.1.: (a) The charge pulses are recorded when the PSD and ^{22}Na source are placed facing the front surface of a planar germanium detector. (b) The measurement is repeated for orthogonal position of the PSD and ^{22}Na source, shining the germanium detector sideways.

sensitive preamplifier with an energy sensitivity of 540 mV/MeV is used. The charge signals from the preamplifier are amplified and shaped using an Ortec 672 spectroscopic amplifier [57]. A shaping time of $\approx 6 \mu\text{s}$ is used for the measurement of the energy resolution. For a ^{57}Co source, an energy resolution of 1.3 keV is obtained for 122 keV full energy events.

A flash ADC (FADC) manufactured by the SIS GmbH (mod. SIS3301) [58] digitises the preamplified charge pulses from the germanium detector. This module is a 8 channel digitiser board with a sampling rate of 100 MHz and 14 bit resolution. For each raw pulse from the preamplifier, 200 samples are recorded corresponding to a sampling window of $2 \mu\text{s}$. The Multi Branch System (MBS) [50] of GSI, is used to read out the FADC and the readout electronics of the PSD for data acquisition.

The pulse shape comparison (PSC) technique [34] is employed to investigate the spatial response of the germanium detector at specified positions inside its volume. After the installation of both the HPGe and the position sensitive detector, the pulses for all the trajectories which are inside the coincidence cone of two detectors are recorded. The (x,y) position coordinates of these trajectories are provided by the PSD. The source and PSD are then rotated by 90° to shine the planar detector sideways as shown in panel (b) of Fig. 5.1. The pulse shapes are again recorded for this configuration of the system. These two datasets are used to obtain the position coordinates of a specific interaction point inside the germanium detector volume as it is indicated below. For example, Fig. 3.4 shows the selection of two particular trajectories in the orthogonal configurations of the setup. At the intersection of the gamma-rays lines of sight, the pulse shapes have to be identical for the irradiation in both the configurations of the assembly. Therefore, the comparison of pulses along these two chosen trajectories

gives the pulse for the intersection point. In section 5.7, a more elaborate analysis method for the pulse shape characterisation of the HPGe detector is described.

The main advantage of using the PSD in our system is that it allows creating a collimation-free scanner, where many lines across the detector or even the whole detector can be scanned simultaneously. Implementation of the gamma camera in the scanning system not only yields to a faster scanning of germanium detectors but also to their imaging. The 2D projected images of the detector obtained in the PSD provided useful information regarding the detector specification and electric field deformations and are summarised in section 5.2 and 5.3 respectively. The expected spatial response of a planar HPGe detector is explained in section 2.3.2. The experimental pulses are obtained applying the PSC method to the orthogonal set of measurements recorded. The rise time behaviour of the pulses is compared over the volume of the planar detector using the T90 parameter (section 5.4). The latter describes the time a signal takes to rise from 10% to 90% of its final amplitude.

5.2. Gamma ray imaging

The germanium crystal is housed in a vacuum-tight cryostat/endcap made of aluminium to reduce the thermal conductivity between the crystal and the outside air. In addition it is cooled to liquid nitrogen temperature (77 K). This is achieved by installing a cold finger made of heat conducting material close to the crystal, which transfers the desired temperature from a storage tank containing nitrogen to the HPGe crystal. In order to avoid leakage currents from the non-contact surfaces of the crystal, they are often shielded by a guard ring. For the present planar HPGe detector, there is a thin beryllium entrance window at the front surface which is protected by a plastic cap. The presence of the cryostat, guard ring, plastic cap and in particular the cold finger contribute to the Compton scattering of the photons from them towards the detector sensitive volume.

The schematic diagram of the planar germanium detector is shown in Fig. 5.2. The pulse height spectrum (PHS) of the germanium detector obtained in coincidence with the PSD is shown in Fig. 5.3.

The 2D projected images of the planar detector obtained in the PSD are shown in Fig. 5.4 for the positions when the PSD is in front of the detector surface and at the side respectively. These images contain both the Compton scattered events and the photopeak events. They are expected to contain contributions from both, the sensitive volume and the surrounding matter around the crystal due to the Compton scattering contributions from the dead materials, which can be compared to the schematic diagram in Fig. 5.2.

The dominant part in these images is obviously the HPGe crystal itself. In the front view Fig. 5.4(a), one can see the end-cap of 70 mm diameter and also the guard ring

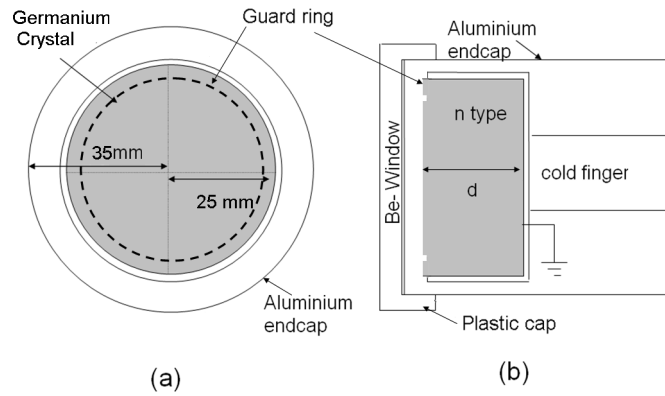


Figure 5.2.: Schematic diagram of an n-type planar germanium detector.

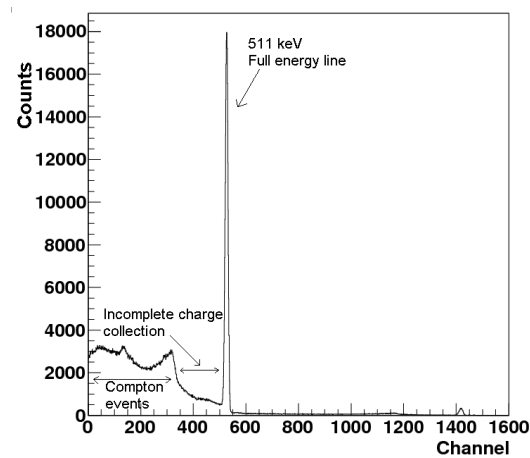


Figure 5.3.: Coincidence pulse height spectrum taken with the germanium detector and a ^{22}Na source.

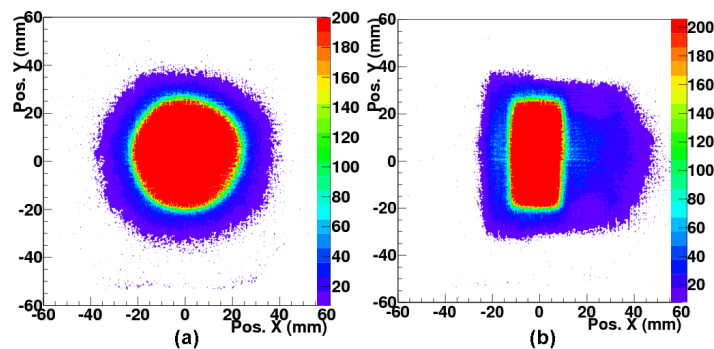


Figure 5.4.: (a) Image of the front view of the planar detector (b) Image of the side view of the planar detector. Both the images are reconstructed for Compton and photopeak events.

around the crystal. The presence of the plastic cap around the Beryllium window and the cold finger is evident in the side view, Fig. 5.4(b). The low intensity events on the rear side are contributed by the Compton scattering from the aluminium

housing which is of lower density than the copper cold finger. The sensitive volume of the detector is seen more clearly when the images are reconstructed only for the photopeak events of the pulse height spectrum (see Fig. 5.5). The deformations seen in this picture are discussed in detail in section 5.6.

5.3. Electric field inhomogeneity

Possible electric field distortions in the peripheral regions of the detector are revealed via the imaging capabilities of this scanning system. The pulse height spectrum (PHS) of the germanium detector shown in Fig. 5.3 shows events between the Compton edge and the photopeak. The electric field inhomogeneities and trapping effects, which lead to an incomplete charge collection can be a possible source of these events. To investigate this, the images of the front and side view of the detector are first reconstructed only for the photopeak events in the HPGe detector and then for the events with partial charge collection. The deformed front and side image of the detector in figures 5.5(a) and 5.5(b) demanding photopeak events shows its sensitive volume. It is expected to yield a circular front and a rectangular side image since the crystal is cylindrical in shape. This effect points towards distortions in the electric field lines and thus incomplete charge collection at the peripheral regions. The events which are missing along the borders in the image in figures 5.5(a) and 5.5(b) are clearly visible in figures 5.6(a) and 5.6(b) when the analysis is restricted to only those events with incomplete charge collection. The latter show the shape of the crystal. The effect is depicted more accurately by comparing the projections of the front view in Y direction for the Y range from -3.0 mm to -10.0 mm in figures 5.5(a) and 5.6(a). The projections are shown in figures 5.7(a) and 5.7(b) where it is seen that the number of counts in the case of photopeak events are higher in the central region of the projection as compared to the counts in the projection of the image for incomplete charge collection region.

5.4. T90 distribution plots

The projection of the front view of the planar detector in the PSD is shown in panel (a) of Fig. 5.5 and the panel (b) represents the corresponding projection in the side view. These images are reconstructed only for the 511 keV coincident full energy events inside the germanium. The color scale in both the position matrices shows the intensity of the registered photopeak events. The coordinates given by the image of the detector in the PSD has to be correlated to a specific gamma-ray trajectory penetrating inside the germanium volume. The coordinates of an intersection point $p(x,y,z)$ (Fig. 5.8) of two selected trajectories in the orthogonal views is uniquely determined by the $(x,y)_{front}$ and $(x,y)_{side}$ coordinates in the PSD-image for front and side views

respectively. Because the PSD provides an image which corresponds to the projection of the HPGe detector volume in the 2D-FoV of the PSD, a dedicated algorithm is needed in order to avoid parallax errors when determining the PSD coordinates for a certain gamma-ray trajectory or intersection point p inside the Ge volume. For this a geometry model was implemented in a C++/ROOT program. The position of the source and PSD is known precisely and the germanium detector is placed in the focal plane of the system. Since we can see the image of the detector, any shift or misalignment in the positioning of the detector can be taken into account. A particular point p inside the germanium volume is selected and the equations of two straight lines a and b are calculated from the chosen point p to the source position coordinates for two positions (A) and (B). The equations of two planes coinciding with the FoV of the PSD is calculated. Finally the position coordinates $(x,y)_{front}$ and $(x,y)_{side}$ on the PSD image are obtained by calculating the intersection of straight lines a and b with the planes F and S respectively. The setup is graphically shown in Fig. 5.9.

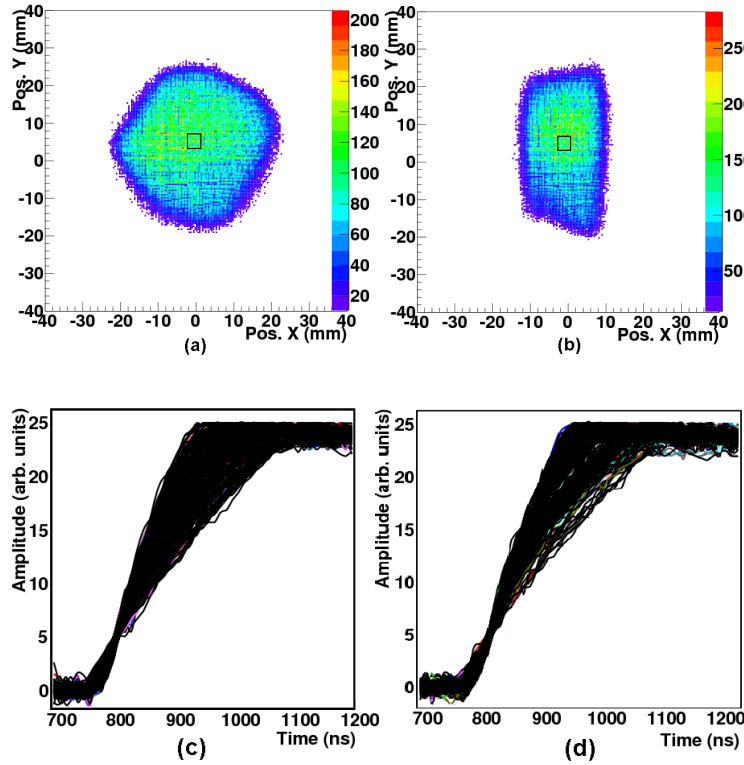


Figure 5.5.: (a) Image of the front view of the planar detector (b) Image of the side view of the planar detector. Both the images are reconstructed selecting only photopeak events (c) Charge pulses corresponding to the events which are inside the graphical cut in front view (d) Charge pulses corresponding to the events which are inside the graphical cut in the side view.

This section describes the extended analysis based on the principle of Pulse Shape Comparison Scan (PSCS). The pulses F_i ($i=1,\dots,n$) for the events inside a square graphical cut of (0.6×0.6) mm² of the front view in Fig. 5.5(a) are examined which

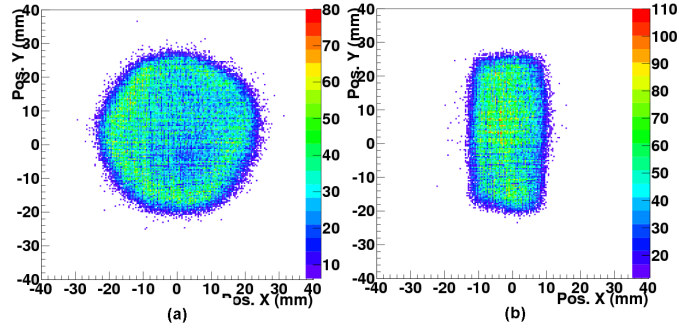


Figure 5.6.: (a) Image of the front view of the planar detector (b) Image of the side view of the planar detector. Both the images are reconstructed selecting only incomplete charge collection events.

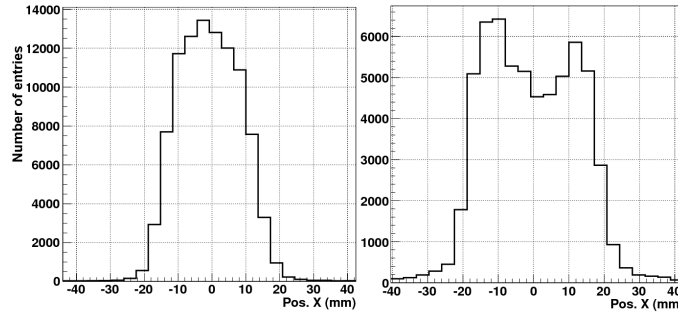


Figure 5.7.: (a) Projection of the 2D image of the detector reconstructed for photopeak events with Y coordinate from -3 mm to -10 mm (b) Projection of the 2D image of the detector reconstructed for incomplete charge collection events for the same region.

is equivalent of selecting pulses along a specific gamma-beam direction inside the volume of the germanium detector. The graphical cuts in Fig. 5.5 are drawn bigger for the sake of understanding. The pulses S_j ($j = 1, \dots, m$) along a trajectory in the orthogonal side view are also selected by using a similar graphical cut. Figures 5.5(c) and 5.5(d) show the time-aligned charge pulses for the selected trajectories in front and side views, respectively. These pulses are time aligned to 1/5th of their rise time. The interaction points are spatially distributed all along the chosen gamma-beam directions and many different signal shapes are visible. Each pulse F_i corresponding to the gamma-ray interaction position along the selected trajectory in front view is compared to all the pulses S_j along the trajectory in the orthogonal view on the basis of a Δ^2 test which is formulated as:

$$\Delta_{i,j}^2 = \frac{\sum_{k=k_0}^{k_{max}} (F_{i,k} - S_{j,k})^2}{k_{max} - k_0} \quad (5.1)$$

where k_0 is the bin number corresponding to the time where the pulses have been time aligned and k_{max} is the bin number for the time when the pulses reach their maximum amplitude. This is the time range in which the charge carriers are migrating towards

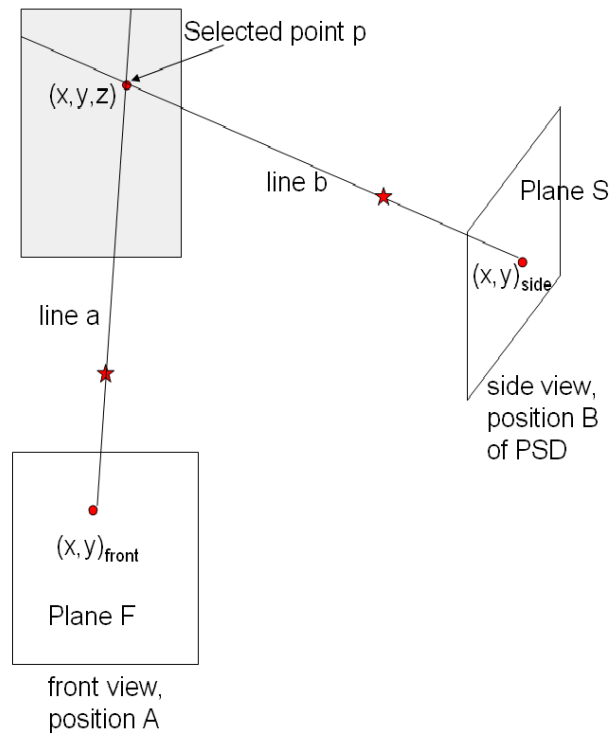


Figure 5.8.: Pictorial representation of the trajectory selection in the front and side view projections of the PSD for a particular interaction position inside the germanium volume .

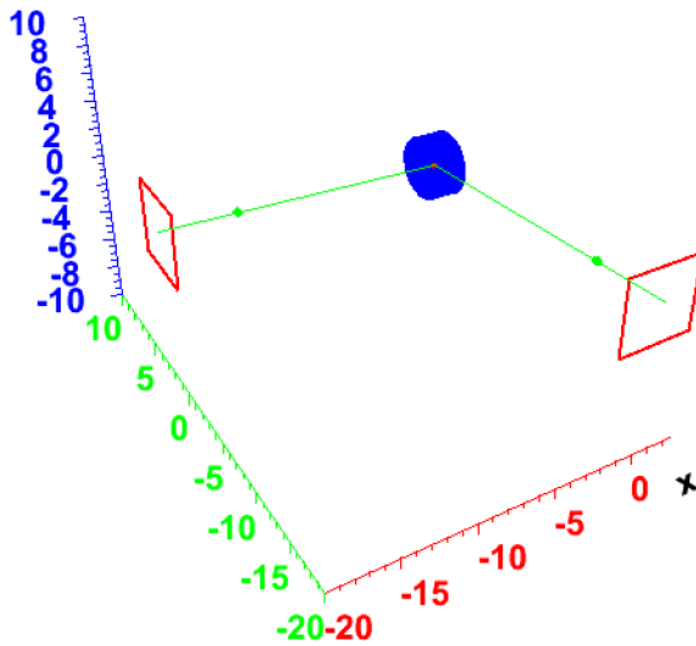


Figure 5.9.: Graphical representation of the trajectories passing through the germanium volume in two orthogonal directions.

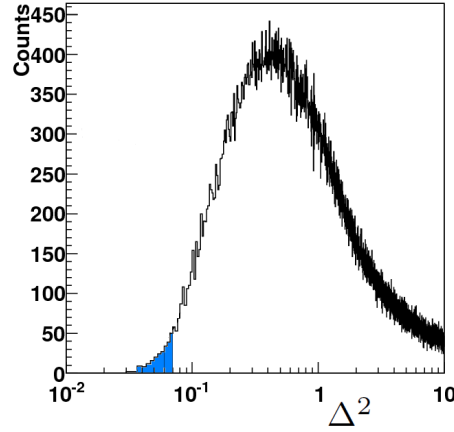


Figure 5.10.: The distribution of Δ^2 values for the comparison of pulses in the selected graphical cuts of side and front view.

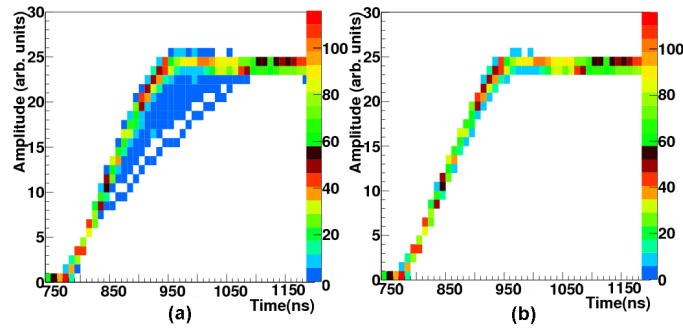


Figure 5.11.: (a) The 2D representation of pulses which are in the selected Δ^2 range (b) The pulses left after setting a threshold on the 2D plot.

the opposite contacts and this determines the slope of the pulse. The amplitudes of the pair of pulses are compared for each bin in the selected range.

The distribution of Δ^2 values for the comparison of all the pairs of pulses in the selected graphical cuts is shown in Fig. 5.10. The higher values of Δ^2 refer to the pairs of pulses which are farther from the crossing point of the selected gamma-beam directions. By finding a reasonable compromise between the statistics of full energy events and the confinement of the intersection point, the upper Δ^2 value is selected in order to discard the wrong pairs of pulses. The selected Δ^2 range is shown by the shaded region in Fig. 5.10. The analysis algorithm is refined further. Figure 5.11(a) shows the 2D representation of the pulses which are below the selected Δ^2 threshold. The color scale represents the number of pulses. The less frequent signal shapes are spurious pulses and can be removed by setting a threshold on this 2D plot of pulses. The remaining pulses correspond to the region around the interaction point, Fig. 5.11(b). The signal shape associated to the interaction position of interest is then obtained by taking the average of ≈ 100 pulses shapes, which are below the constrained Δ^2 threshold and over the threshold on the pulse frequency plot, out of a

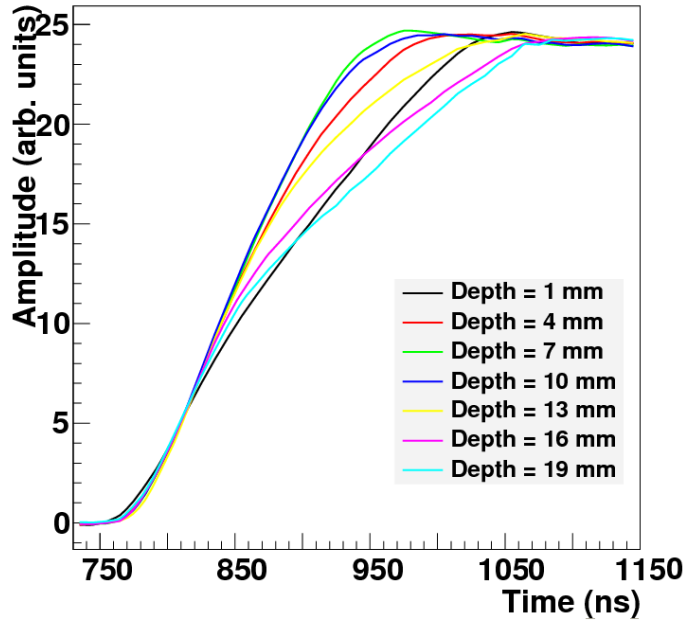


Figure 5.12.: Experimentally determined signal shapes inside a planar germanium detector at seven different interaction positions.

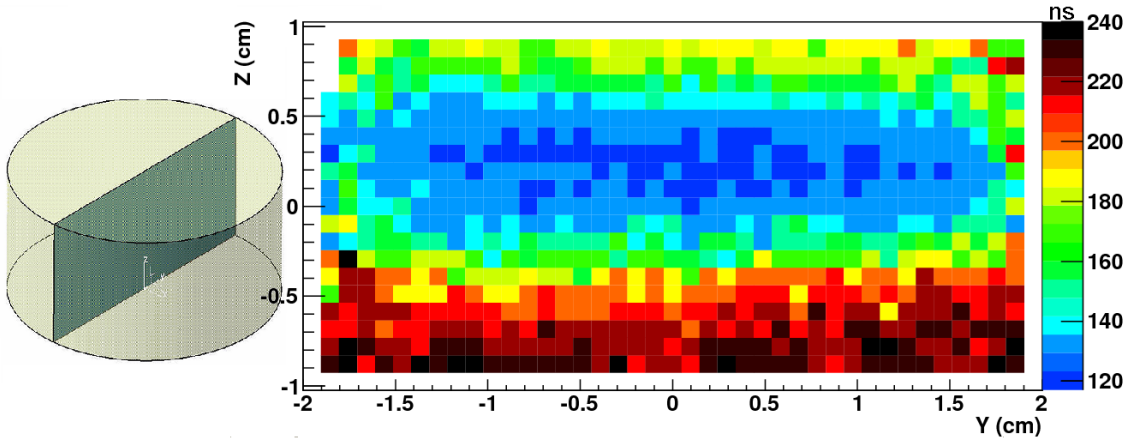


Figure 5.13.: T90 rise time distribution plot in ns for a slice at half thickness of the detector

total number of ≈ 2000 pulse shapes in each of the chosen graphical cuts. To obtain the signal shapes along a particular collimation line inside the detector, the graphical cut in the front view is kept constant and the cut corresponding to the side view of the planar detector is shifted to seven different positions, namely at 1, 4, 7, 10, 13, 16, 19 mm from the p^+ contact of the detector. The same analysis procedure is applied to obtain the signal shapes at these positions. The result is shown in Fig. 5.12.

The T90 (the time it takes for the pulse to rise from 10% to 90% of its amplitude) rise-time distribution plot for a slice along the center of the detector volume is shown in Fig. 5.13. The color scale represents the rise-time in ns. These distributions reflect

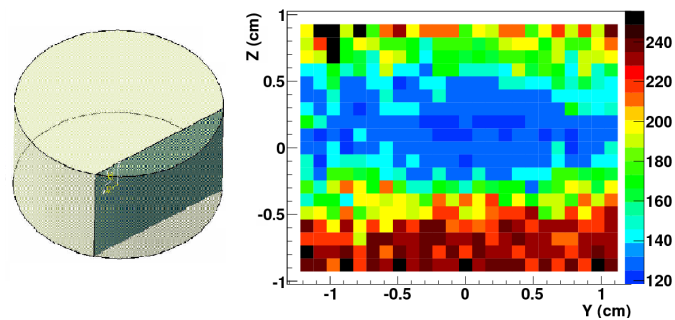


Figure 5.14.: T90 rise time distribution plot in ns for a slice at 1.6 cm away from the central axis of the detector.

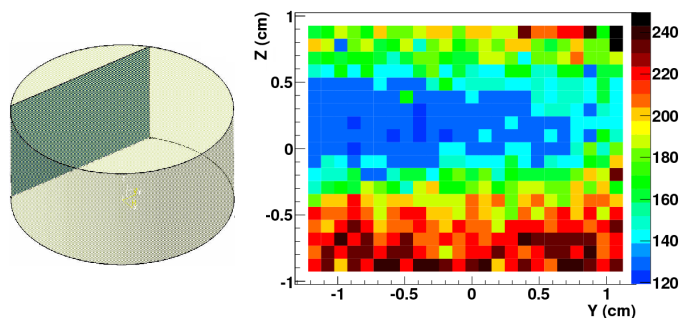


Figure 5.15.: T90 rise time distribution plot in ns for a slice at 1.6 cm away from the central axis of the detector in opposite direction as compared to the previous case.

the interplay of the motion of both, the electrons and holes, in the mechanism of signal generation. The rise-time varies between 120-240 ns which corresponds to the spatial distribution of interaction positions. The pulses are slow for the interactions close to the n^+ contact. As the positions of interaction are deeper inside the crystal, the pulses reach their maximum amplitude faster in contrast to the pulses near the p^+ and n^+ layers. The positions near the center of the crystal where the collection time of electrons and holes is similar have the minimal rise-time. However, towards the border of the detector, where the electric field lines are inhomogeneous, the charge collection times are long. One should be aware of the fact that to obtain the aforementioned T90 plots, the analysis is restricted only to the fully absorbed 511 keV photopeak events. In Fig. 5.5(b), the image of the side view is more deformed on the lower surface as compared to the upper surface. The T90 distribution plots are obtained for these two different regions at 1.6 cm away from the central axis of the detector, (figures 5.14 and 5.15). It is clearly seen that the plot corresponding to the slice 1.6 cm distant from the center towards the lower surface (Fig. 5.15) is more deformed towards the border as compared to the one corresponding to the upper surface (Fig. 5.14). The electric field is inhomogeneous in these regions leading to longer rise times.



Figure 5.16.: The scanning system at IPHC Strasbourg.

5.5. Validation measurements with a conventional scanning system

The charge pulses of the planar HPGe detector were also determined experimentally by means of a conventional scanning system at IPHC-Strasbourg. This system is based on a well established single coincidence technique. It consists of a 480 MBq collimated ^{137}Cs source (with a hole diameter of 1.5 mm and a length of 17 cm) placed on a horizontal XY moving table (see Fig. 5.16). The detector is placed vertically facing the collimator. The collimator position on the XY table defines the (x,y) coordinates of the gamma beam interaction positions inside the detector. The Z position is defined by a slit of 1.5 mm in 5 cm lead placed adjacent to the HPGe detector. The Compton scattered photons are detected in a BGO detector placed behind the lead collimator slits. This BGO detector is a 1 inch scintillator. The pulses are recorded and digitized using TNT2 digitisers with 14 bit resolution and a sampling rate of 100MHz.

During the analysis, only those events are selected which are Compton scattered at 90° from the HPGe volume to the BGO detector via the lead collimator slits. Energy windows of 288_{-80}^{+90} keV on the BGO and 374 ± 6 keV on the HPGe were applied to select the proper events. The pulses shapes are recorded for 6 different depths, at $z = 6, 9, 11, 14, 18, 19$ mm, by shifting the lead collimators vertically. The (X,Y) collimator is placed below the center of the crystal. For each position the average pulse is calculated by taking the average of about 150 traces.

The average traces obtained from the conventional scanning system are shown in the Fig. 5.17(a) and the traces obtained with the PSCS technique for the same positions

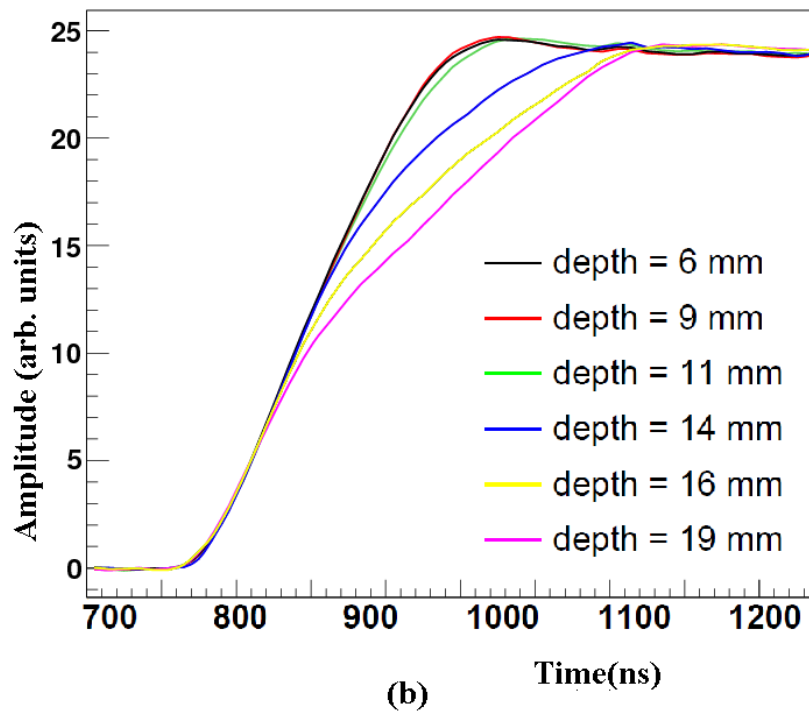
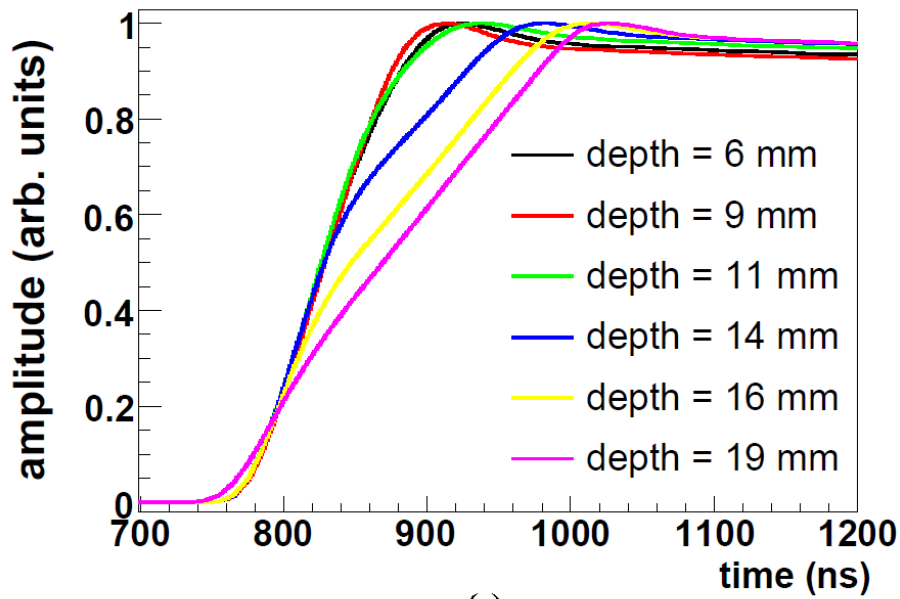


Figure 5.17.: (a) Average charge pulses obtained with the IPHC scanning facility based on the conventional approach with collimators, (b) Average charge pulses obtained with the GSI scanning system based on the pulse shape comparison scan.

are shown in Fig. 5.17(b). The pulse rise time behavior obtained with the conventional and PSCS scanning techniques is shown in Fig. 5.18 (a) and (b) respectively. They both have the similar trend of being faster close to one contact and having minimum

at ≈ 9 mm. The difference of about 30 ns in the absolute T90 values is at present ascribed to the differences in the electronics employed for the measurements with two setups.

The capabilities of the system are tested with the non segmented planar HPGe detector. However, to explore the full potential of the device and to validate the PSCS principle it is necessary to measure the spatial response of a highly segmented HPGe detector.

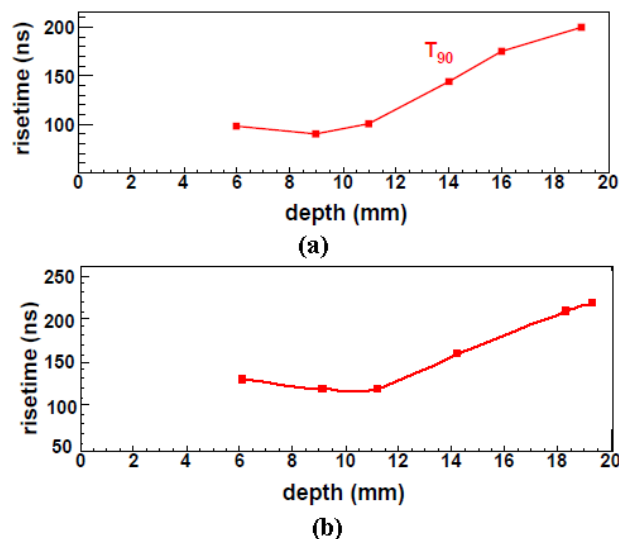


Figure 5.18.: The pulse rise time for six different positions measured with (a) conventional scanning system , (b) with the pulse shape comparison scan method.

5.6. Conclusions

A unique technique to measure the position response of HPGe detectors is presented. The rise time behaviour of the charge pulses is compared over the volume of a planar germanium detector using the T90 parameter. The latter describes the time a signal takes to rise from 10% to 90% of its final amplitude. The scanning of detectors is faster as compared to the conventional coincidence based systems because of the implementation of a gamma-ray position sensitive scintillator detector. In addition, deformations of the electric field inside the fully depleted crystal are observed via the image obtained in the PSD. The imaging capability of the system makes it possible to know the exact location of the germanium crystal inside the cryostat and the shape of the sensitive volume, which is critical to generate the pulse shape database for segmented HPGe detectors. The imaging aspect of the system is thus an added advantage as compared to the existing scanning systems. A conventional scanning system at IPHC Strasbourg is used to obtain the position response of the same detec-

tor. The results are compared and they agree with each other with some differences because of the difference in the electronics used for the measurements.

6. Position response of a segmented AGATA germanium detector

In this chapter, the position response of the AGATA S001 single crystal is reported. It was provided by the AGATA collaboration for its characterisation with the GSI scanning system in fall 2010. The risetime distribution plots for the gamma-ray interaction positions in coaxial and planar regions of the detector volume are presented. Furthermore, the Multi Geometry Simulation (MGS) [59, 60] code is used to generate the theoretical distribution plots for comparison. MGS is a code developed by IPHC Strassbourg for the simulation of the electric field in germanium detectors. The charge carrier transport behaviour as a function of the depth is studied for the region of the complex electric field around the front part.

6.1. Physical Details of AGATA

The aim of the AGATA array [17] is to do gamma ray tracking on a close packed configuration of germanium detectors with largest possible solid angle coverage around the target position. The array will be constructed from 180 hexaconical, large volume, encapsulated 36 fold electrically segmented HPGe crystals. They will be mounted in 60 identical triple cluster cryostats with a combination of three asymmetric crystals, see Fig. 6.1. This arrangement will provide 82% solid angle coverage with sufficient space for ancillary detectors and beam-pipe. The construction is like the filling of hexagons in a soccer ball, to have a spherical configuration in which the individual crystals are close to each other. These HPGe crystals are manufactured by the company Canberra Eurisys [56]. The details of the design are given in [17].

Although the final AGATA array will consist of asymmetric crystals, the first crystals delivered for testing are symmetric. The AGATA crystal used in this work for scanning measurements is the symmetric S001 crystal. Its schematic view is shown in Fig. 6.2(a) and Fig. 6.2(b) shows the picture of the encapsulated crystal. The detector is an n-type germanium crystal of coaxial geometry mounted in a single test cryostat [61] provided by the University of Köln. The front surface of the crystal is a regular hexagon of 61.1 x 52.9 mm dimension, Fig. 6.3. It is electrically segmented into 36 segments with 6 segments in both horizontal and vertical direction. The segmentation pattern is shown in Fig. 6.3. The length of the crystal is 90 mm and the hexagon extends from front towards backward until it reaches a diameter of 80 mm. Beyond

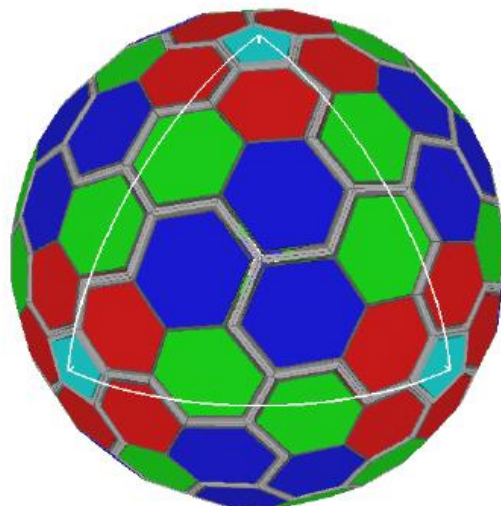


Figure 6.1.: AGATA array with 180 highly segmented germanium crystals encapsulated in 60 triple clusters [17].

that it has a cylindrical geometry. The central bore of 5 mm radius is drilled from the back along the axis of the cylinder till the depth of 13 mm from the front surface of the crystal. The cryostat has 37 cold FETs for the 36 segments and the central core signals and the corresponding preamplifiers [62, 63, 64].



Figure 6.2.: (a) The schematic diagram of symmetric prototype AGATA crystal [17] and (b) Picture of S001 encapsulated symmetric crystal.

As shown in Fig. 6.3, the horizontal segmentation divides the 90 mm long crystal in 6 rings of 8, 13, 15, 18, 18, 18 mm depths respectively. The vertical segmentation is done along the center of the 6 tapered sides of the hexagon. The 6 lateral sectors are labeled from A to F. In each sector, they are numbered from 1 to 6 starting from front towards the back, e.g. A1, A2, A3, A4, A5, A6. The segmentation pattern shown in Fig. 6.3 is ideal. In fact the effective segmentation is different as a consequence of the variant electric field lines.

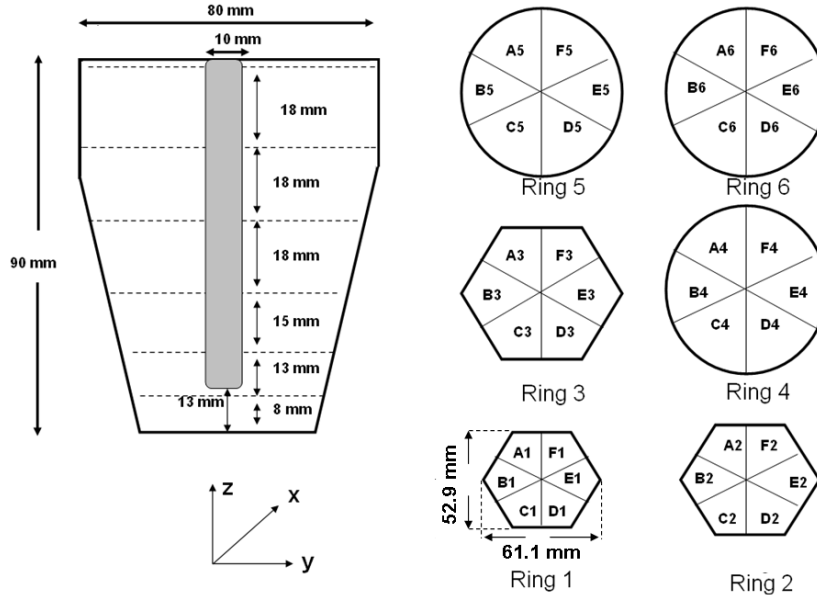


Figure 6.3.: The schematic representation of the front hexagonal surface, side projection showing the bore, segmentation pattern and the label convention.

6.2. Electrical details

In order to fully deplete the germanium detector, an operating voltage of +4000 volts is applied to its central contact via a NHQ 204M power supply unit from ETPS Ltd. [65]. 7 MDR cables take the preamplifier signals from the 36 contact outputs and the central core, to 4 differential to single end converter boxes. These boxes were designed by the University of Köln. The outputs of these converter boxes are then fed to SIS 3302 digitiser cards from Struck, using Lemo cables. Each digitiser has 8 channels, 100 MHz sampling rate and 16 bit resolution. Each channel provides 200 samples of 10 ns each for every event. The coincidence between the AGATA core signal and the PSD dynode signal for 511 keV photoevents is used as an external trigger for the SIS 3302 and also for the CAEN V792 QDC modules used for the digitisation of anode charge signals from the position sensitive detector. The AGATA-PSD coincidence data flow is $\approx 7\text{MB/s}$. The Multi Branch System (MBS) of GSI is used to read the digitised signals. The Go4 software is used as a graphical interface for the online analysis of the data.

6.3. Scan set-up

After the cooling and pumping of the detector, it was mounted in the upgraded version of the scanning table as shown in Fig. 6.4. The $300\text{ kBq }^{22}\text{Na}$ is placed in between

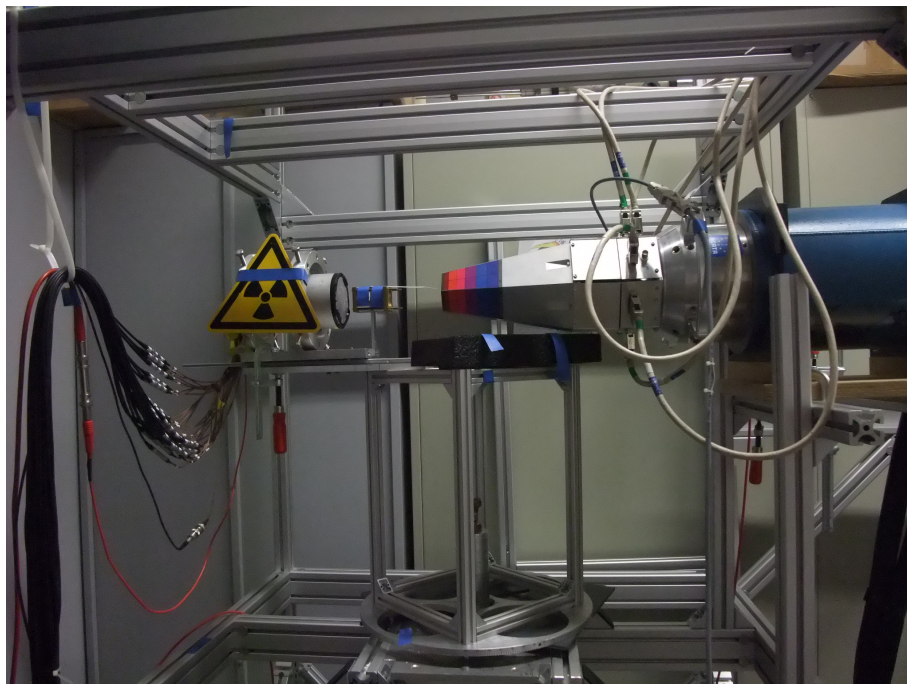


Figure 6.4.: Agata S001 detector mounted in the scanning system.

the hexagonal face of the germanium crystal and the position sensitive detector. The trigger electronics used for the scanning of AGATA is exactly the same as used for the planar HPGe detector (chapter 5). The only difference in this case is that, instead of using CAEN FADC to digitise the charge signals, SIS 3302 [66] modules from Struck [67] were used.

6.4. Intensity maps

The SIS 3302 modules yield the information of the energy deposited in individual segments for each event using a moving window deconvolution algorithm [68]. Using the pulse height spectra of the individual segments, it is possible to select an energy window on any desired region of the spectra to see the detector response. A 2D projected image of the HPGe detector is seen in the position sensitive detector (see Fig. 3.4).

This image is reconstructed for 511 keV coincident photpeak events in both the PSD and germanium. Figure 6.5 shows the distribution of the intensity of these events in the 6 rings of the detector. The preamplifier of segment E2 was broken, which accounts for the missing part in ring 2. The intensity pattern shows the segmentation lines and also the core hole from ring 2 onwards. The intensity in the back segments decreases because of attenuation of photopeak events along the depth of germanium. In all the rings and in particular in ring one, one can see the lower intensity of photopeak events

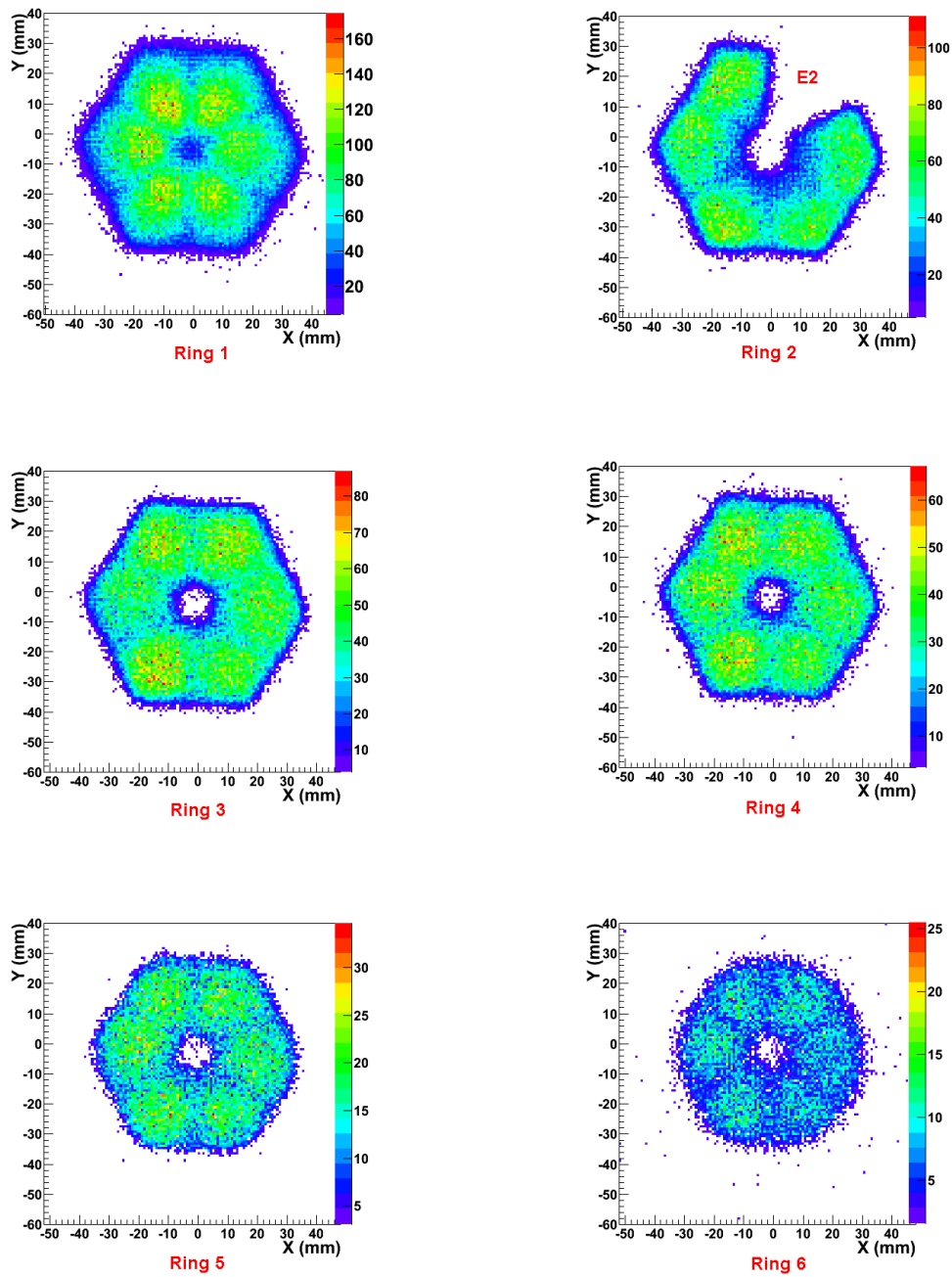


Figure 6.5.: Intensity maps for different rings for full energy photopeak events in individual segments. The increase in the image size from ring 1 to ring 6 is due to the difference in the distance of these rings from the PSD. Since ring 1 is closer, its projected image is larger and the contrary explanation applies to ring 6.

towards the borders. Since scattering out of the segments (multiple interactions) is more probable in those regions, it results in decreased full energy events. The size of the projected images depend on the detector to PSD distance. The larger

size of first ring as compared to the last ring is a consequence of this effect.

6.5. Pre-processing of data

Each event in the AGATA crystal gives 37 charge signal shapes from the digitiser card. One of them is from the central contact (core) and the remaining 36 are from the outer segment contacts. The following discussion assumes the full energy (511 keV) deposition in any one segment.

Figure 6.6 shows an example, where the net charge is deposited in segment C4. The shape of this pulse is a function of the motion of both the electrons and the holes. In addition in a segmented germanium detector, there is a transient/image charge signal seen in the neighbouring segments. As the name says, these signals are present only for the time when the charge carriers are drifting in the net charge collecting segment. For an interaction in segment C4, the prominent transient charge signals are seen in the top and down (B3, B4, B5, D3, D4, D5) and left and right (C3 and C5) segments. In order to achieve a position resolution better than the size of the segments, an analysis of both the hit and neighbouring segment signals is required.

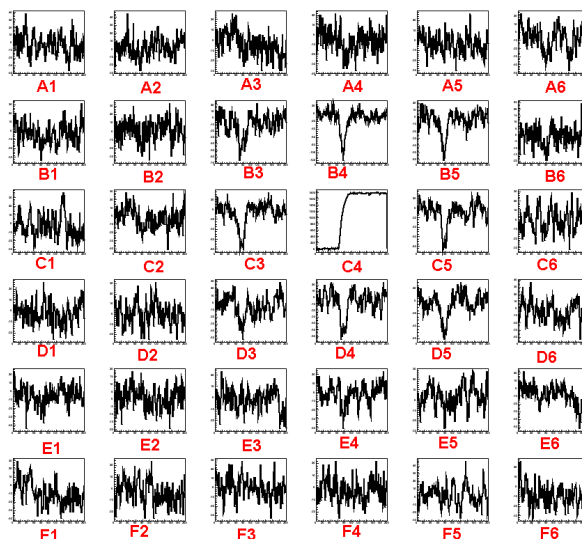


Figure 6.6.: Signals of all the 36 segments for a full energy event in segment C4. The columns represents the signals from the segments in a ring. The transient charge signals in the neighbouring segments are also visible. The largest amplitude of mirror charges is for the direct and diagonal neighbours. The signal from segment E2 is only the pre-amplifier noise.

The pulse from each segment has 200 samples of 10 ns each. Variations of the preamplifiers and the digital electronics for each channel yield slightly different baseline shifts and amplitude gains. The following steps are done on the pulse shapes on an event by event basis before doing any further analysis.

1. Baseline subtraction: The average of the first 30 samples for each pulse is subtracted to reset the baseline to zero.
2. Normalisation: The maximum amplitude of the hit segment pulse is averaged for the last 50 samples and then normalised to 1000.
3. Time alignment: In order to do proper time alignment of the pulses, for each event the signal from the net charge collecting segment is first linearly interpolated from 10 ns per sample to 1 ns per sample. The T10 (time taken by the pulse to reach 10% of its maximum amplitude) of the pulse is then shifted to a pre determined sample number. The remaining 35 pulses are shifted by the same factor.

An example of time aligned pulses in a hit segment is shown in Fig. 6.7, where all the traces are time aligned to 400 ns.

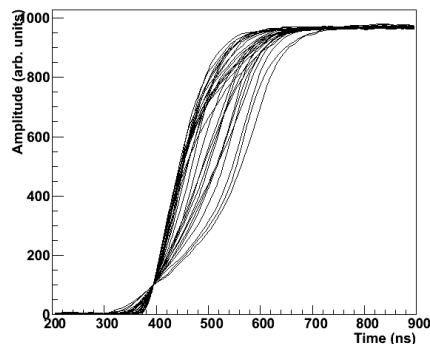


Figure 6.7.: Normalised time aligned traces for full energy 511 keV events in a segment.

6.6. Supertrace

A super trace is a trace containing the samples from all the 36 segments. For full energy events in a particular segment, the most significant transient charge signals are from the adjacent segments (see Fig. 6.6). For an event, a truncated supertrace of 1000 samples is constructed. The first 200 samples are from the hit segment and the following contain the samples from the four adjacent neighbours, up, down, left and right. Figure 6.8 shows one such trace, for an interaction in segment F3. The neighbours considered are F1 (down), F4 (up), E3 (right), A3 (left).

6.7. Radial distribution of pulses

A) Side Scan:

The Agata detector in the scanning system is shown in Fig. 6.4. It is first shined

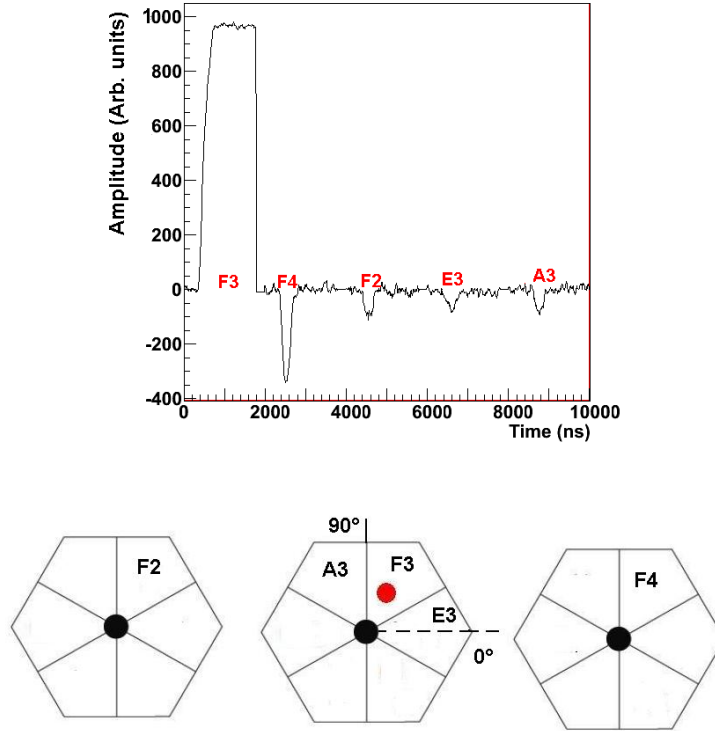


Figure 6.8.: Truncated supertrace for an interaction in segment F3 shown by the red dot.

with ^{22}Na source from the front and then the source and PSD are moved by 90° to shine the detector from sideways. A particular trajectory in the second configuration is chosen such that it passes through the middle of segment A2. This is done by using the information from the position sensitive detector. The details of the trajectory selection are given in chapter 5. Since the detector has coaxial geometry, the pulses of segment A2 for interactions along this trajectory show the distribution along the radius of the detector (Fig. 6.9) at a certain depth. As the pulse shape comparison scan is still not applied, at this stage we only know that these pulse shapes are distributed along the radius, but their exact position is still not known. For segment A2, the adjacent neighbours are A1, A3, B2, F2. A truncated supertrace is formed with these neighbours. The amplitude and the polarity of the transient charge signal

depends on the radial and azimuthal interaction position in the hit segment. When the interaction positions are close to the core, the transient charge signal has maximum positive amplitude. As the positions are farther from the core towards the border, the maximum amplitude decreases. It finally goes negative, changing the polarity and increases in opposite direction. The traces are grouped according to the transient charge pulse amplitude range in segment A1. An average trace is calculated for each of the amplitude selected group of traces. For the chosen trajectory in segment A2, in Fig. 6.10, the behaviour of the average hit segment pulse shape corresponding to a

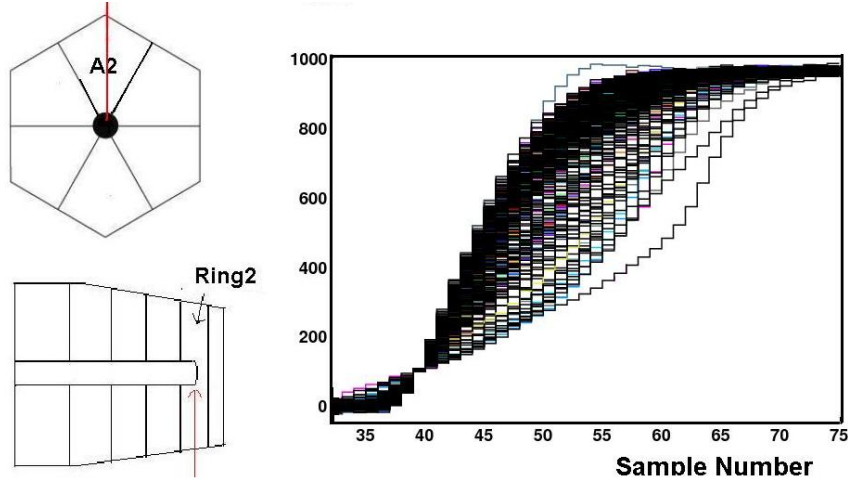


Figure 6.9.: Traces for interaction points radially distributed along a trajectory in segment A2.

transient charge signal of particular amplitude is presented. This gives an estimate of the radial distribution of pulse shapes in ring 2. Along a radius of 32 mm, 25 different pulse shapes can be seen, which implies a position resolution of at least 2 mm. In order to know the exact position response, the pulse shape comparison scan technique is employed and is described in the next section.

6.8. Pulse shape comparison scan

To find the pulse for an interaction position, two trajectories are selected for the front and side view measurements respectively (see Fig. 3.4). The interaction points are spatially distributed all along the chosen γ beam directions and many different signal shapes are present. Each pulse along the selected trajectory is compared to all the pulses of the orthogonal view on the basis of a Δ^2 test [69]. The average of pulses with very low value of Δ^2 is assigned to the intersection point of the two selected trajectories. Ideally an average of ≈ 100 pulses should be taken for each interaction position. This gives an average pulse with minimal statistical noise. However in the present measurement, the accumulated statistics was not enough to reach this number. Nevertheless with the amount of data for each set, having ≈ 400 pulses for each trajectory, it is possible to do an analysis to validate the scanner principle with a segmented germanium detector. A voxel size of 1 mm^3 is chosen around each interaction position. The number of events in each cubic volume goes down exponentially from borders towards the core at any particular depth. The average of the first six pairs of pulses having lowest value of Δ^2 is taken to correspond to the signal shape for a particular position. This gives a dynamical upper limit of the Δ^2 distribution and no lower limit. One should bare of the fact that the outer contact signals are used to do the pulse shape comparison scan.

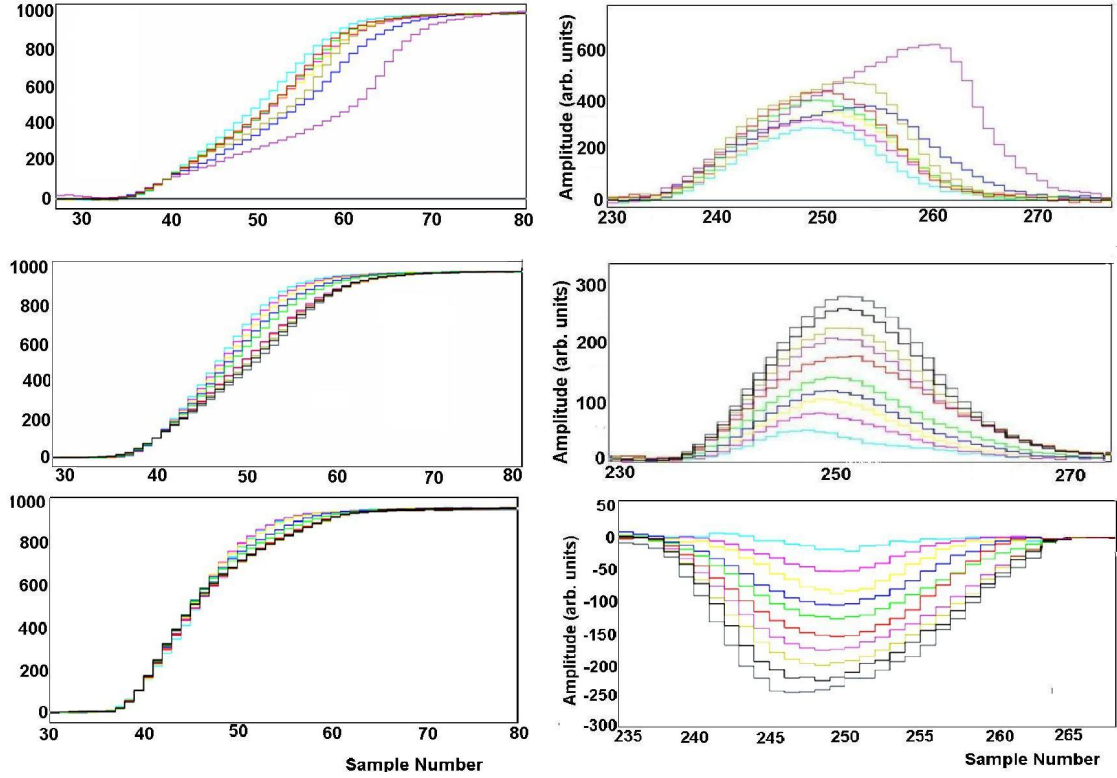


Figure 6.10.: Average pulse shapes of the hit segment and a nearest neighbour by demanding different amplitudes of the transient charge signal.

The radial interaction position is provided to some extent by the selection of the trajectory in the front view and also by the polarity of the image charges. Either polarity is possible dependent on the different contributions of the motion of electrons and holes. This increases the position sensitivity, since only by looking at the polarity of image charges, one can distinguish between the large and small radii interactions. This effect is demonstrated in Fig. 6.11 for two interactions at radii 12 and 30 mm at azimuthal angle 60° in segment F3. The vertical adjacent segments give information on the depth of interaction and the horizontal adjacent segments provide the azimuthal interaction position. The amplitude of the transient signal in either of these neighbours increases as the interaction is closer to the segment boundary of any of them (see Fig. 6.12). In the present case of a segmented detector, it would thus be sufficient to compare only the transient signals of the truncated supertrace for the two trajectories. Each pulse F_i corresponding to a trajectory in front view is compared to all the pulses S_j along the trajectory in the orthogonal view on the basis of the Δ^2 test which is formulated as,

$$\Delta_{i,j}^2 = \sum_{m=seg} \frac{\sum_{t=t_0}^{t_{max}} (F_{i,t}^m - S_{j,t}^m)^2}{t_{max} - t_0}, \quad (6.1)$$

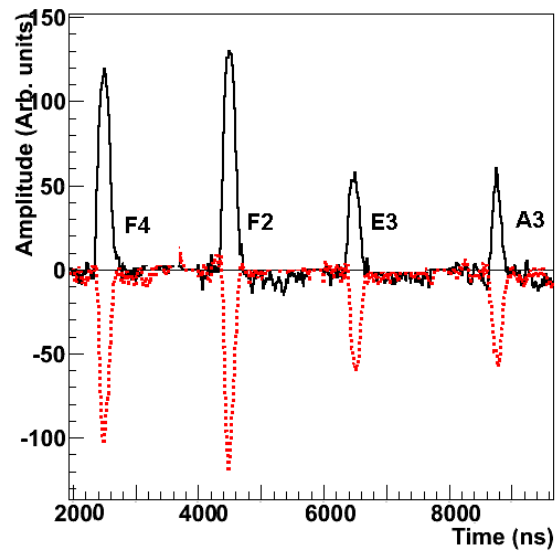


Figure 6.11.: Truncated supertrace shown by the black line for an interaction in segment F3 at radius 12 mm and angle 60° . The mirror charges in up and down segments are of positive polarity. Whereas for an interaction in segment F3 at radius 30 mm and angle 60° (shown by the red line), the mirror charges in up and down segments are of negative polarity. The z value is 28.5 mm in both the cases.

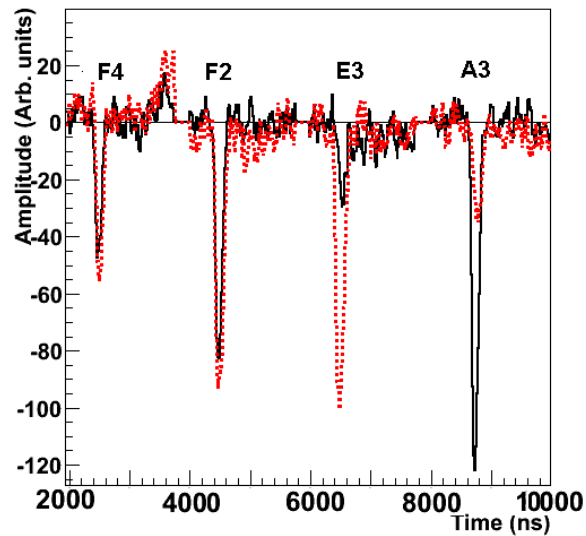


Figure 6.12.: Truncated supertrace for an interaction in segment F3 at radius 28 mm for azimuthal angle 30° (red) and 90° (black), the mirror charge in segment E3 has higher amplitude as compared to the amplitude in segment A3. On the contrary, for an interaction in segment F3 at radius 30 mm and angle 90° (black), the mirror charges in segment A3 are of higher amplitude. The z is 28.5 mm in both the cases.

where index m refers to the nearest neighbours and index t refers to the samples of the signal. Comparing only the transient charge signals for interaction positions distributed along a particular radial line, a position resolution of 2 mm is achieved.

6.9. Image charge asymmetry

The amplitude of the mirror charge signals in the horizontal adjacent segments depends on the azimuthal interaction position. An asymmetry parameter is introduced to provide a direct measure of angular positions at fixed radius. For the segment F3, it is defined by equation 1.

$$Asymmetry = \frac{Amplitude(A3) - Amplitude(E3)}{Amplitude(A3) + Amplitude(E3)} \quad (6.2)$$

where $Amplitude(A3)$ and $Amplitude(E3)$ are the amplitudes of the image charges in segment A3 and E3. The variation of this parameter as a function of angular position between the segment A3 and E3 is represented in Fig. 6.13. The maximum difference in the transient signal magnitudes is at the segment boundaries. If the interaction is close to the segment boundary with A3, the magnitude of image charge in A3 is higher than in E3, giving large positive value for asymmetry. The large negative values are for the positions close to the segment E3.

The amplitude of the mirror charge in a segment falls off linearly as the angular distance from the hit segment increases. The linear behaviour of asymmetry parameter is in agreement with it as expected.

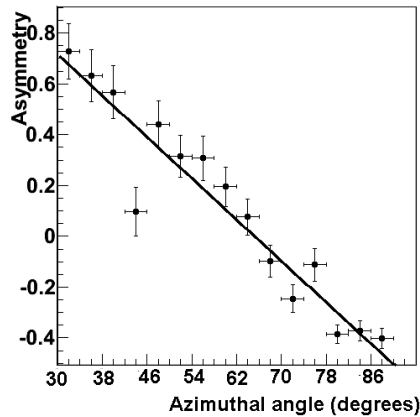


Figure 6.13.: Asymmetry between segment A3 and E3 plotted as a function of azimuthal interaction position at 30 mm radius in segment F3.

6.10. Multi Geometry Simulation, MGS

In order to find a theoretical data set of pulse shapes to compare with the experimental measurements, a detailed calculation was made utilizing the Multi-Geometry Simulation code [59, 60].

The Multi-Geometry Simulation (MGS) code is a tool to do the characterisation of HPGe detectors. The calculations are performed in MATLAB matrix environment. For a defined geometry and physical parameters like voltage, temperature, impurity concentration, it first calculates the potential distribution by solving the Poisson equation. The electric field at each position on a 1 mm grid is calculated using the potential gradient. The drift velocity of electrons and holes is determined using the electric field values. The pulse shapes at a specific electrode for different interaction positions are generated by applying the information of charge carrier trajectories and the weighting field of that electrode. The latter is defined as the electric field calculated by solving the Poisson equation, taking a potential of 1 Volt on the considered electrode and zero on all the other electrodes. The input parameters used for the S001 AGATA geometry are tabulated in Table 6.1. The distance between the crystal and the encapsulation is referred as spacing. In order to eliminate the artifact of strong electric field at $z = 90$ mm, the back spacing parameter is increased from 22 to 50 mm.

Table 6.1.: Parameters used for the S001 AGATA geometry for the MGS simulation.

Parameter	Value
Grid Size	1 mm
Inner contact voltage	+4000 V
Outer contact voltage	0 V
Impurity concentration (front)	$1.8 \times 10^{10} \text{ cm}^3$
Impurity concentration (back)	$5.1 \times 10^9 \text{ cm}^3$
Temperature	86 K
Forward spacing	1.0 mm
Backward spacing	50.0 mm
Distance to cathode	13 mm from front surface
Anode radius	5 mm

The simulated electric field strength in Volts/cm is shown in Fig. 6.14(a) for the xz plane at $y = 0$ mm. The drift velocity of electrons calculated for the full volume is shown in Fig. 6.14(b) for the xz plane. The color scale displays the velocity in cm/sec. The arrows represents the electric field vectors which determine the trajectories of electrons and holes. The strong electric field near the core results in saturated drift velocities in that region. Based on the field distribution, the detector volume can be categorized in three regions (Fig. 6.15(a)). The zone near the bottom of the core has planar electric field. Near ring 2, it has semiplanar field and coaxial field from ring 2 onwards. Examples of trajectories of electrons to the central contact are shown for these three regions in Fig. 6.15(b), (c), (d) by the solid line.

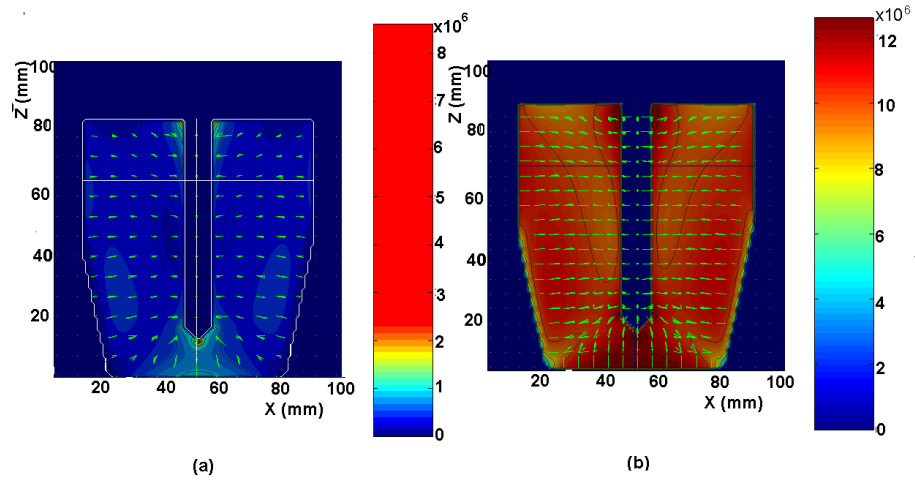


Figure 6.14.: (a) Electric field distribution in the xz plane at $y = 0$ calculated using MGS. The color represents the field strength in volts/cm. (b) The distribution of the drift velocity of the electrons in cm/sec. The arrows represent the electric field vectors.

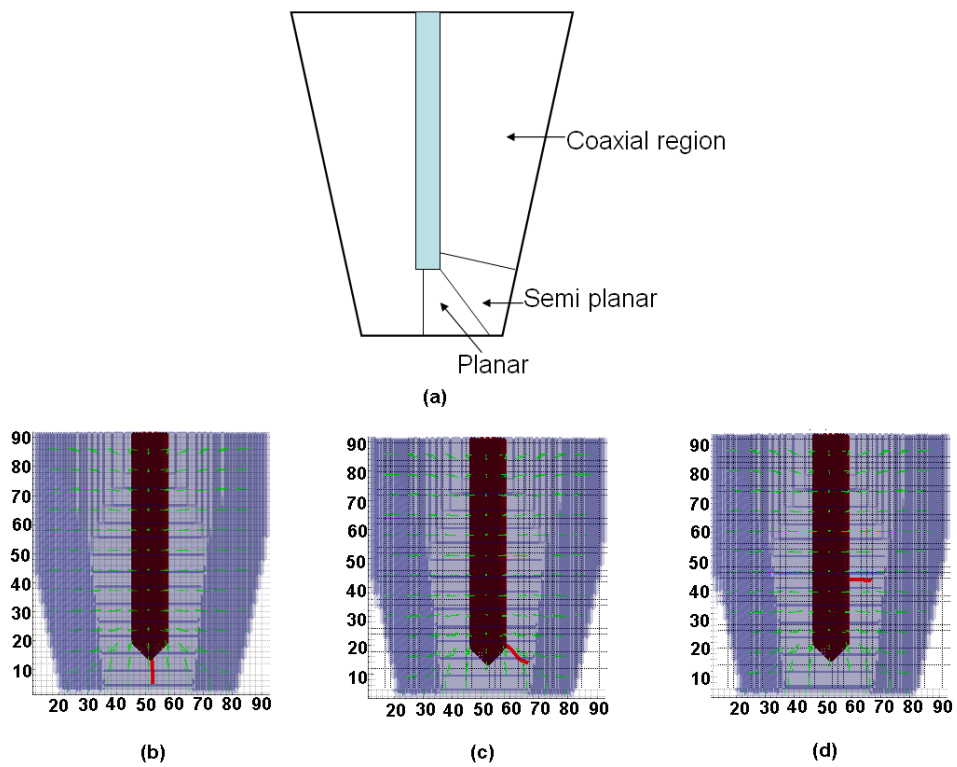


Figure 6.15.: (a) The division of germanium volume in three regions of electric field and (b), (c), (d) electron trajectories shown by the solid red lines in these zones.

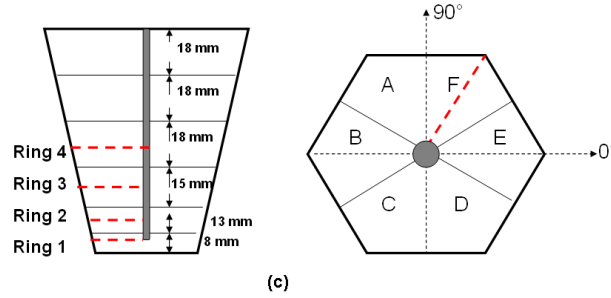


Figure 6.16.: The schematic distribution of the selected interaction points in ring 1, 2, 3 and 4.

6.11. Risetime distribution plots

The hit segment pulse shape strongly depends on the radial interaction position. The time taken to reach various percentage of maximum pulse amplitude, reflects its shape. T30 (time to 30% of the maximum pulse amplitude) and T90 (time to 90% of the maximum pulse amplitude) are the parameters typically chosen to represent spatial distribution of the charge signals. These values are measured from the time where all the pulses are aligned.

Figure 6.17 and 6.18 show the T30 and T90 distributions (solid circles) as a function of the radial interaction position for 4 segments in section F (F1, F2, F3, F4) corresponding to the rings 1, 2, 3 and 4 respectively. The radius range is from 8 mm to 38 mm. The points are along the middle of each segment in depth ($z = 4, 14.5, 28.5, 45$ mm) and at an azimuthal angle of 60° . To aid the reader, Fig. 6.16 also shows by dotted lines, how the positions are distributed in each segment.

The leading part of each signal is a function of the motion of electrons as they are the faster charge carriers and in fact determine the T30 values. The interaction positions in segment F1 are close to each other because of its smallest size and the difference in the distances which electrons have to travel to the core is small, which accounts for a comparatively flat T30 distribution in Fig. 6.17(a). However in the other rings, a large variation in the T30 distribution, from ≈ 120 ns for smaller radii to 30 ns for larger radii is seen.

The T90 distribution is determined by the motion of both electrons and holes. The positions where both the electrons and holes have to travel the same distance to the opposite contacts give rise to the minimum in the T90 plots. Whether the interaction is at smaller or larger radii, either of the charge carrier has to travel a longer distance yielding larger risetimes for both of these regions. For ring 3, segment F3, the maximum T90 at 8 mm radius is 250 ns compared to 270 ns for ring 4, segment F4, which has larger radii.

The risetime distribution plots for the same positions as in Fig 6.16 are also calculated using MGS and they are shown in Fig. 6.17 and 6.18 with stars for comparison. The preliminary analysis shows quite good agreement with MGS. The average maximum and minimum deviations in the T90 values are 38 ns and 2.5 ns respectively. The

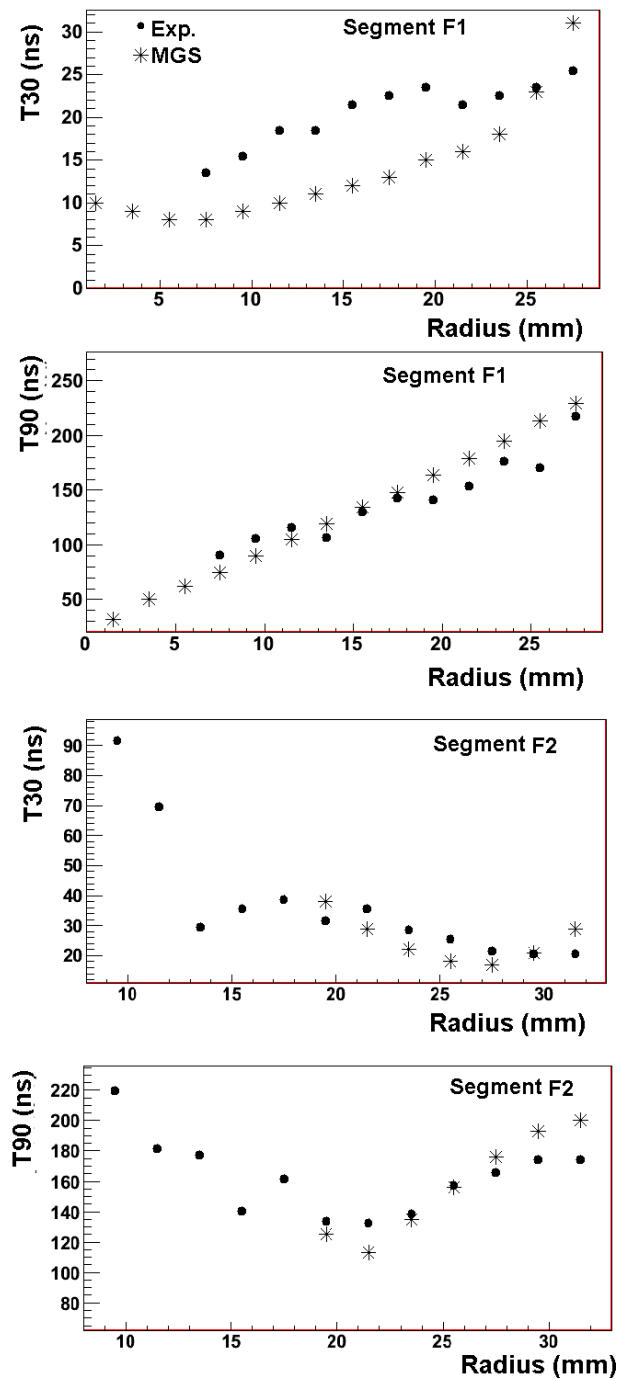


Figure 6.17.: T30 and T90 distributions for two segments in section F, corresponding to ring 1 and 2. The values are for radial interaction positions distributed at 60° azimuthal angle and half depth of each segment. The experimental values are shown by solid circles and the values calculated with MGS simulations are represented by stars (see text for details).

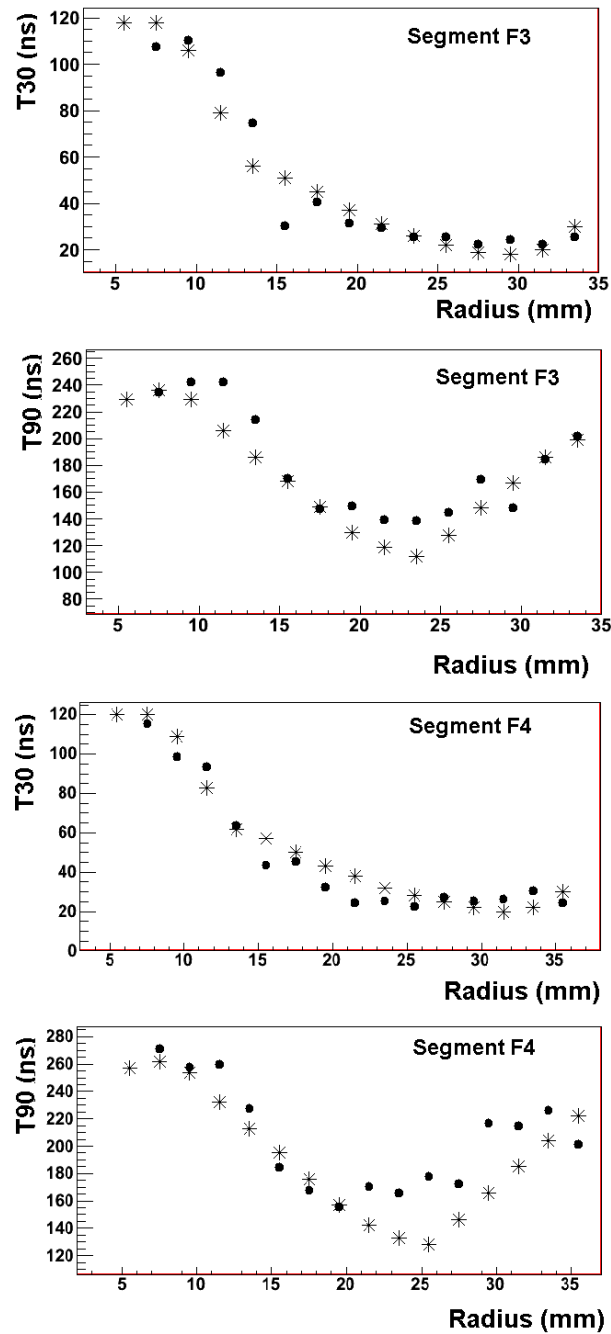


Figure 6.18.: Experimentally determined T30 and T90 distributions for two segments F3 and F4 corresponding to ring 3 and 4. The values are for radial interaction positions distributed at 60° azimuthal angle and half depth of each segment. The simulated T30 and T90 values for the same positions are shown by stars.

corresponding values for T30 are 13 ns and 0.6 ns respectively. The deviation in the position determined experimentally and by MGS is in the range from 1 - 7 mm. The largest discrepancy in the rise-time values and the deviation in the positions are seen

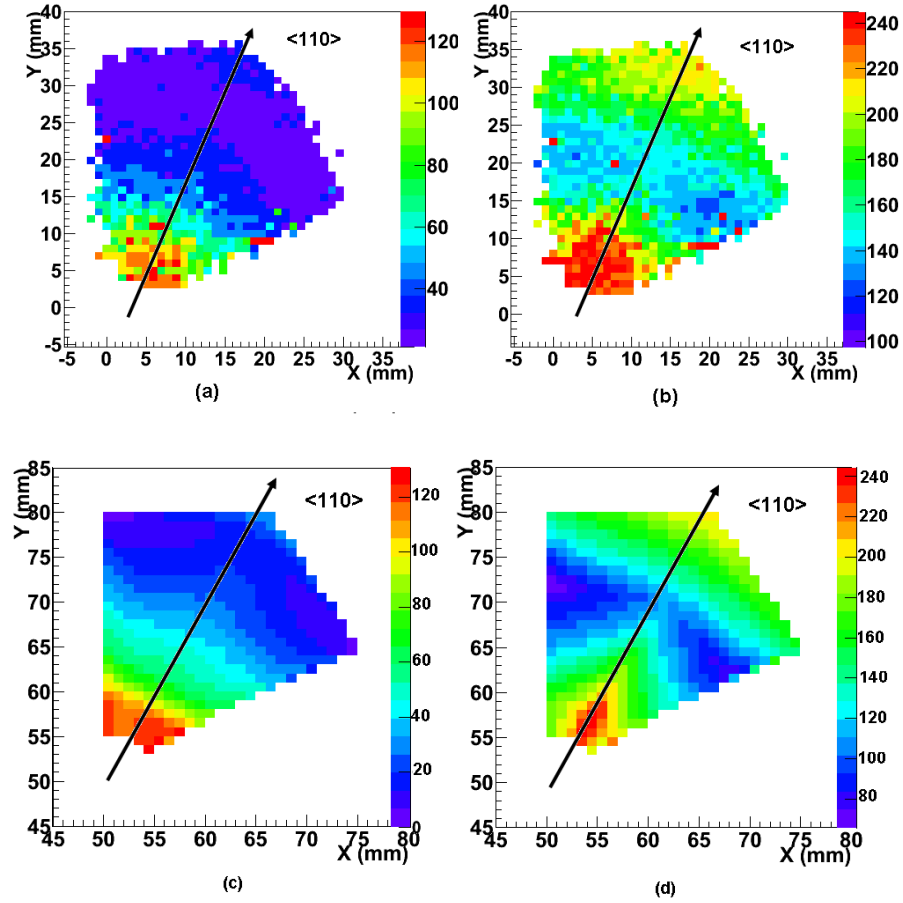


Figure 6.19.: T30 and T90 distribution for segment F3 in ring 3. (a) and (b): Experimentally measured risetime distributions, (c) and (d): simulated risetime distributions. The color scale represents the risetime in nanoseconds. The crystallographic axes are marked by arrows and the extension of longer risetimes along the $\langle 110 \rangle$ direction is due to the slow drift velocity of charge carriers in the direction.

in ring 1. This is attributed to the complex electric field in zone 1 and the uncertainty in defining the end of the cylindrical bore. The absence of the simulated values at smaller radii for ring 2 is due to the semiplanar electric field in that region and is explained in section 6.12.

Figure 6.19(a) and (b) show the two dimensional T30 and T90 distribution plots for the complete horizontal slice of segment F3, at $z = 28.5$ mm (middle of the segment) respectively. The color scale represents the value of T90 and T30 rise times in nano seconds. The average risetime behaviour along the slice is same as for a single azimuthal angle radial distribution explained above. Additionally the visibility of crystallographic orientation effects can also be appreciated. In a Ge crystal the drift velocity of electrons and holes is different along different axes depending on their orientation with respect to the applied electric field. The crystallographic axes are marked in Fig. 6.19 by solid black lines. The drift velocity of charge carriers is fastest along the $\langle 100 \rangle$ direction which is confirmed by the extension of short rise times to

larger radii. On the contrary, along the $\langle 110 \rangle$ direction, the slower drift velocity of charge carriers lead to longer risetime. The contour plots for T30 and T90 risetimes calculated applying MGS electric field simulation are also shown in Fig. 6.19(c) and (d).

6.12. Effective segmentation

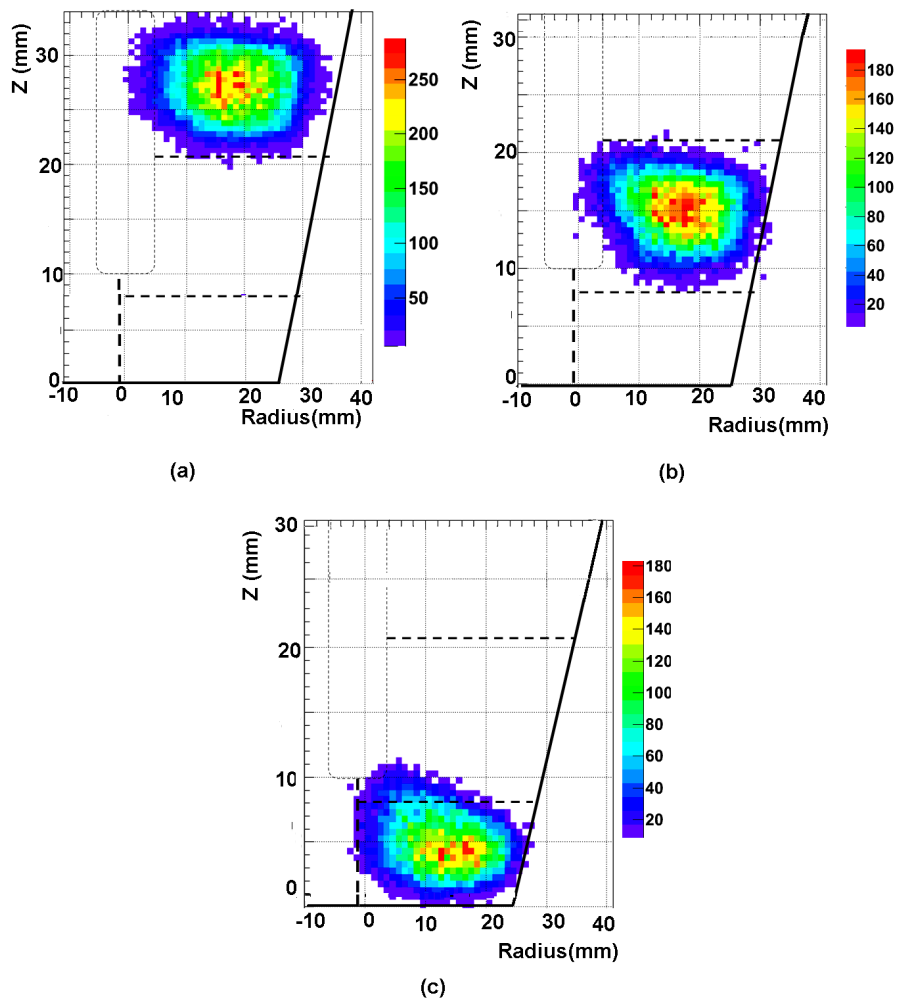


Figure 6.20.: The intensity distribution plots of segment F3 (a), F2 (b) and F1 (c) for full absorption 511 keV events. These plots indicate the departure from the ideal segmentation pattern. The color scale (ns) has a threshold for low statistics events at the edges of the segments.

The absence of simulated T30 and T90 values at smaller radii for ring 2 (segment F2) in Fig. 6.17(c) and (d) at $z = 14.5$ mm is explained by the semi planar electric field in that regions (see Fig. 6.14(a)). For interaction points in ring 2 approximately below

the middle depth, the charges are collected by the outer contacts of ring 1 instead of ring 2. Since the calculations with MGS is based on outer contact signals, no pulse shape is obtained for smaller radii in ring 2.

The same effect is also seen experimentally, but is less severe as predicted by the simulations. This is justified by examining the intensity distribution plots of segment F2 and F1, Fig. 6.20 (b) and (c) respectively for 511 keV full absorption events. These plots are the two dimensional projected images in the position sensitive detector when the detector is shined from sideways. The extension of photopeak events of segment F1 in segment F2 is an indication of departure from the ideal segmentation pattern. However, these events do not extend till the half depth of segment F2. The intensity plots measured for segments F3 and F2, Fig. 6.20(a) and (b) are almost in agreement with the pattern given by the simulation.

The measured and calculated segmentation lines between segments F1, F2 and F3 is shown in Fig. 6.21. Panel (b) shows the distribution of hit segment as a function of depth (z) starting from the front of the detector till the end of the segment F3 (ring 3). The interaction positions are spatially distributed along the radius for each depth. The color indicates the effective segmentation pattern which is different from the ideal segmentation pattern seen in Fig. 6.3.

One should bare of the fact that the probability of multiple interactions increases at the segment boundaries, resulting in low statistics of photopeak events, as shown in Fig. 6.21(a).

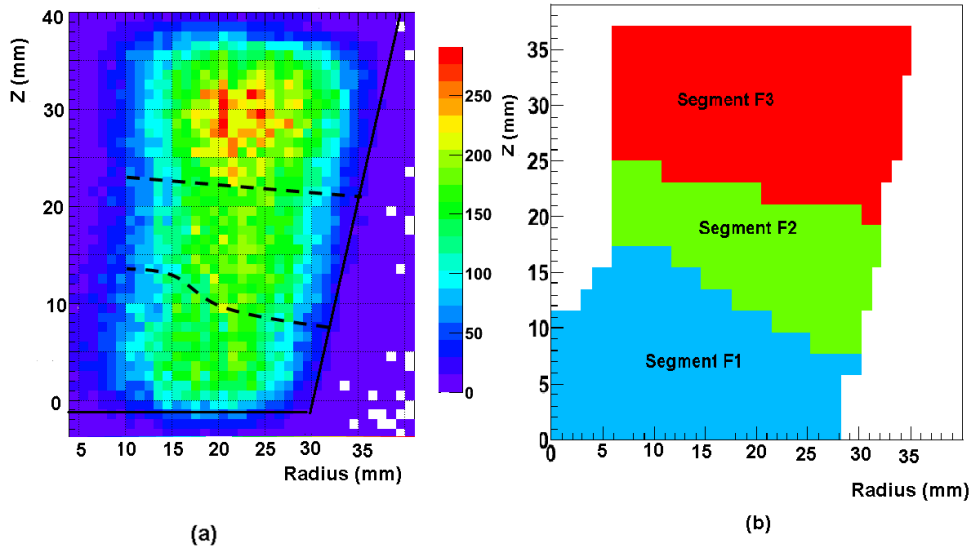


Figure 6.21.: (a) The experimentally measured intensity distribution plot of segment F3, F2 and F1 for full absorption 511 keV events. This plot indicates the segmentation pattern between the segments, (b) The segmentation pattern given by MGS. A discrepancy between the pattern given by MGS and scanning measurements is seen.

The explanation for the difference in the effective segmentation seen experimentally

and via simulation is provided by the assumption used in the simulation that the impurity gradient is linear throughout the depth of the crystal. In addition, the variation along the radius at a certain depth is not considered in the calculations. The values provided by the manufacturer are only for the front and back surfaces. It is therefore important to include these factors more accurately in the future cycles of the simulations.

The determination of pulses with pulse shape comparison scan (PSCS) is based on the comparison of traces along two orthogonal trajectories. Even though there is no charge collection at the outer contacts at small radii in ring 2, the comparison will still give traces with minimum value of Δ^2 . However these Δ^2 values are 2 orders of magnitude higher than the values for the positions where there is charge collection at the respective segment electrode. This effect is demonstrated in Fig. 6.22, where the Δ^2 values (in logarithmic color scale) are plotted for the radial interaction positions in segment F2 at an azimuthal angle of 60° for the complete depth (z). To select the correct pulses for these positions, the PSCS is carried out using the photopeak events in segment F2 and also in segment F1. The events with the charge collection in the electrode of segment F1 are then recovered. This gives two Δ^2 values for the same position. Lower value among them then correspond to the correct pulse.

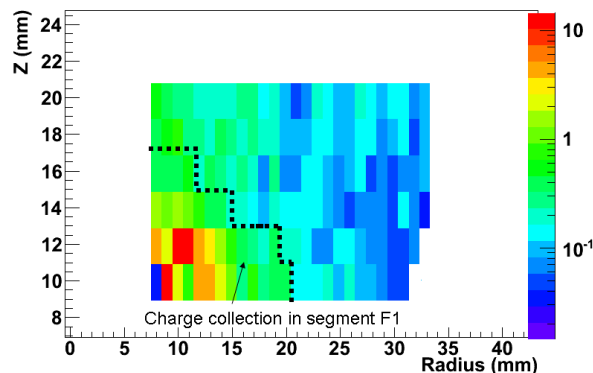


Figure 6.22.: The Δ^2 values (in logarithmic color scale) are plotted for the radial interaction positions in segment F2 at an azimuthal angle of 60° for the complete depth (z). The higher values of Δ^2 in some regions (separated by the dotted line) indicates that the charges are not collected at the respective electrode.

6.13. Rise-time behaviour as a function of depth

It is interesting to see how the transition in risetime behaviour occurs as the depth (z) changes. The inherent advantage of our system is that all the detector is scanned in a single measurement and hence the study of the depth dependent pulse shape behaviour can be done without any additional measurement.

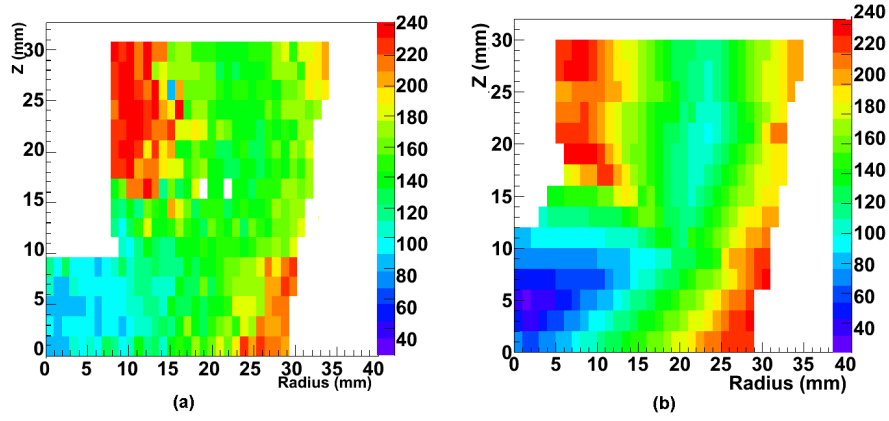


Figure 6.23.: (a) Experimental and (b) simulated T90 risetime distribution plots for the section F from the front of the detector $z = 0$ mm till $z = 30$ mm as a function of the radial interaction position. The azimuthal angle is 60° . The color scale represents the risetime in nanoseconds.

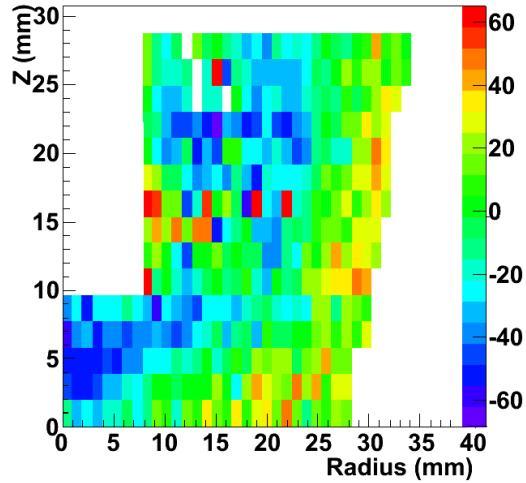


Figure 6.24.: (a) The difference (in ns) between the theoretical and experimental T90 values for the first values of impurity charge concentration in table 6.2.

The 2D T90 risetime distribution plot as a function of the depth and radius, from ring 1 to ring 3 for section F is shown in Fig. 6.23(a) and (b). The depth z varies from (0 - 30) mm and the radius starts from 8 mm from ring 1 onwards. The average behaviour along the radius is same as is seen in Figs. 6.17 and 6.18. The distribution plot for the same positions is also calculated with MGS (Fig. 6.23(b)). Figure 6.24 represents the difference between the theoretical and experimental T90 values which shows the discrepancy between them near the core in ring 1 of ≈ 50 ns and also in ring 3 of $\approx \pm 30$ ns.

One of the possible reasons for the disagreement between the numbers obtained from simulation and scanned data could be the effect of the response function of the pream-

plifier. Signal shapes including the pre-amplifier response are obtained by using a recurrence relation depending on the cutoff frequency, f_c of the pre-amplifier.

$$q(t) = aq_0(t) + (1 - a)q(t - 1) \quad (6.3)$$

where, $q(t)$ is the charge after including the pre-amplifier response and $q_0(t)$ is the original value of the charge at time t . a is called the smoothing factor and is given as,

$$a = \frac{2\pi f_c}{2\pi f_c + 1}. \quad (6.4)$$

When this is included in the calculations, the disagreement still remains (see Fig. 6.25(a)).

Table 6.2.: Two different sets of impurity charge concentration parameters used for S001 AGATA geometry for MGS simulation.

Parameter	First Value	Second value
Impurity concentration (front)	$1.8 \times 10^{10} \text{ cm}^3$	$1.0 \times 10^{10} \text{ cm}^3$
Impurity concentration (back)	$5.1 \times 10^9 \text{ cm}^3$	$2.5 \times 10^9 \text{ cm}^3$

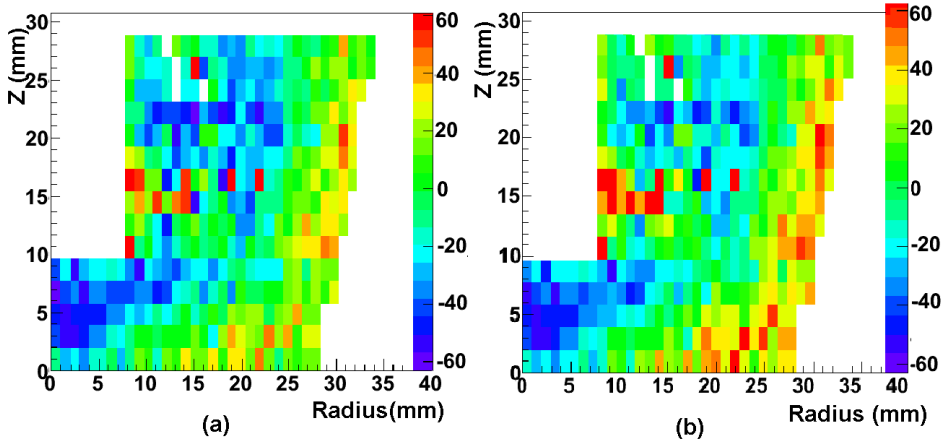


Figure 6.25.: (a) The difference between the theoretical and experimental T90 values after including the bandwidth of the preamplifier and (b) for the values of impurity charge concentration decreased by a factor of 2 (second values in table 6.2).

Another reason could be the value of the impurity charge concentration. The simulation is performed again by keeping all the other parameters same and decreasing only the impurity charge concentration by a factor 2 for both front and the back part of the detector. The values of the impurity concentration parameters are tabulated in table 6.2. Fig. 6.25(b) represents the difference between the theoretical and experimental T90 values for the decreased value of the charge concentration parameter. Although

the differences has smaller value in ring 3, near the core in ring 1 the discrepancy is almost the same as before.

At the moment, the data which is provided by the manufacturer is only for the front and back part of the AGATA detector. It is assumed that the impurity concentration falls linearly with depth. Moreover at a fixed depth, the radial dependence is not included. One way to investigate this effect is to perform capacitance-voltage measurements. The impurity concentration is related to the change in capacitance with voltage for planar and cylindrical approximations [85] as

$$N(d) = -\frac{C^3}{\epsilon\epsilon_0 A^2} \left(\frac{dC}{dV}\right)^{-1} \quad (6.5)$$

and

$$N(r_d) = -\frac{Cr_d^3}{4\pi^2\epsilon\epsilon_0 r_d^2 H^2} \left(\frac{dC}{dV_b}\right)^{-1}. \quad (6.6)$$

where, d is the depletion depth, A is the surface area, C is the capacitance at the applied voltage V for planar geometry approximation. In the case of cylindrical approximation, r_d is the depletion radius, H is the height of the cylindrical segment. The planar approximation underestimates the impurity concentration at the front part of the detector and the cylindrical approximation holds good only for the upper four rings of the AGATA detector which have cylindrical coaxial geometry. It is difficult to test the reliability of the simulations in this zone where the simple geometry consideration does not hold good. Even though different parameters were used, the assumption that the gradient of concentration varies linearly is still kept. This shows that even though the impurity concentration is changed by a factor of 2, a simple approximation of impurity charge gradient cannot provide a agreement with the scanned data. Even if the capacitance is measured as a function of voltage for the whole detector, it is not trivial to find the impurity charge concentration applying only the assumption of cylindrical or planar geometry. This makes it extremely important to have an experimental pulse shape basis for PSA to be applied to the complicated geometries. Low energy gamma rays are typically stopped in the front part of the detector which makes the region near the core in ring 1 and ring 2, to be the most crucial part to be scanned experimentally.

7. Conclusion and Outlook

New radioactive ion beam facilities like FAIR [71], SPIRAL-2 [72, 73], SPES [74], will become available in the next few years. Even though they will provide superior beam intensities as compared to existing facilities, the nuclei in the most exotic regions will still be produced with low rates. Gamma ray spectroscopy in those regions will be a big challenge because of these low rates and considerable Doppler broadening of the lines due to high recoil velocities. To explore unknown territories of the nuclear chart with the future beam facilities, it is required to develop improved gamma detector arrays for gamma ray spectroscopy. A lot of instrumentation and developmental work is going on for two major projects in this direction, AGATA [30, 75, 76] in Europe and GRETA [77] in the USA. These arrays are based on electrically segmented large volume HPGe detectors and digital electronics. The aim is to determine the interaction positions and the corresponding energies deposited at the sub-segment level with a precision of a few mms using pulse shape analysis [26, 27, 78] and then to do gamma ray tracking [28, 79, 80]. Before installing the segmented germanium detectors in tracking spectrometers, a detailed investigation of the pulse shapes for each interaction position inside the detector is needed.

A simple and compact scanner has been designed for measuring the spatial response of HPGe detectors. It is based on the principle of pulse shape comparison scan (PSCS) and positron annihilation correlation. The determination of the pulse shape for a particular position is based on the comparison of two orthogonal sets of pulse shapes. The key feature of the device is the implementation of a position sensitive detector (PSD). It not only makes the device 100 times faster than conventional scanners, but also provides the additional advantage of imaging capability. The PSD is based on a LYSO scintillating crystal coupled to a crossed-wire anode position sensitive photomultiplier tube. The remarkable spatial resolution of ≈ 1 mm (FWHM) and a very large field of view of 28 cm^2 of the PSD is achieved using the individual multianode readout (IMAR) method and the pattern position fitting approach [45].

The scanning system is first applied to obtain the spatial response of a planar HPGe detector. The deformations of the electric field inside the fully depleted crystal are observed via the image obtained in the PSD. The imaging capability of the system makes it possible to know the exact location of the germanium crystal inside the cryostat and the shape of the sensitive volume, which is critical for generating the pulse shape database for segmented HPGe detectors. The imaging aspect of the system is thus an added advantage as compared to the existing scanning systems. The rise time behaviour of the charge pulses is compared over the volume of a planar germanium detector using the T90 parameter. The latter describes the time a signal takes to rise from 10% to 90% of its final amplitude. A conventional scanning system at IPHC

Strasbourg is used to obtain the position response of the same detector. The results are compared and they agree with each other with small differences because of the difference in the electronics used for the two measurements.

The principle of the system is validated through the test of a 36 fold segmented AGATA crystal. The risetime distribution curves are compared with the theoretical curves extracted applying the MGS electric field simulation code. The average behaviour of the simulated data is similar to the experimental data points. The scanning of the AGATA crystal with a conventional scanning system for ≈ 1200 positions takes ≈ 90 days as compared to ≈ 8 days needed in our case. Even if we would like to take twice longer measurements to have more statistics, it will still be considerably faster than other existing systems. In addition, one can scan the complete triple cluster containing three AGATA crystals at the same time. Since for that case, the distance between the germanium and PSD detector has to be increased to achieve a larger field of view, a stronger activity source has to be used.

Although the scanner is primarily intended to be used for the position characterisation of germanium detectors, it can also be used for scintillators. It is in fact a multi-purpose imaging device and can be applied for the imaging of any passive object. It is also possible to explore the benefits of the device in medical physics. We have achieved a position resolution of 1 mm with the PSD in two dimensions. The efficiency can be further improved by using thicker scintillation crystal. In that case, one has to correct for the parallax error caused by the finite uncertainty in the depth of interaction in the crystal. After applying such correction, 3D spatial sensitivity can be reached.

Nevertheless there are still a number of factors that can be improved. The statistics acquired with the small planar germanium detector was enough but with AGATA, it was not sufficient to make a database yet. Because of the limited availability of the detector, it was not possible to take longer measurements. In order to have ≈ 100 traces for each position, we will need approximately ≈ 3000 signals for the chosen trajectory. In addition, the analysis has to be adapted to include the effect of effective segmentation in the segmented detectors. The experimental database has also to be tested for the pulse shape analysis with real events.

The calculations performed with MGS depend on a number of crystal properties. The first is the distribution of the electric field and the potentials for a defined geometry. In order to find the orientation of the crystal with respect to the symmetry axis, the measurement of the rise-time is performed at some angular positions at the same radius from the core of a coaxial detector. This influences the electron and hole mobility parameters. It is also necessary to include the response function of the electronics employed and the cross talk properties due to the capacitive coupling between the core and the segments. One of the important parameters is the impurity charge concentration. Even if one can make capacitance voltage measurements for all the segments, simple cylindrical or planar geometrical approximations to calculate the impurity charge concentration do not hold good for complex geometries. This influences the electric field strength and hence the risetime of the charge signals.

Even with the best possible approximations and models for simulations, it is necessary

to test how realistic the pulse shapes obtained from them are. This can be achieved only by scanning the detectors. In fact the simulations and experimental determination of pulse shapes are complimentary to each other. One is needed to prove the accuracy of the other.

The scanning system shown in this work is a prototype model. The rotating table employed had a precision of 1° . The detector could be placed at the focal plane of the device with an accuracy of ≈ 3 mm. The good results obtained with it gives motivation for the design of new mechanical setup. The precision of the rotating table and the mechanical stability of the whole apparatus are crucial for reliable results. It has to be assured that the detector lies exactly at the focal plane of the system so that a direct correlation can be made between the interaction position coordinates with respect to the scanning table reference frame and the detector frame of reference. Triangulation laser systems are available in the market for this purpose and it is planned to be implemented for the upgraded version of the scanner. The Δ^2 comparison method used to find the pulse shapes for a particular position can also be improved. The comparison of the pair of pulses from the orthogonal set of measurement is done at the moment using the following formula (see section 5.4),

$$\Delta_{i,j}^2 = \frac{\sum_{k=k_0}^{k_{max}} (F_{i,k} - S_{j,k})^p}{k_{max} - k_0}, \quad (7.1)$$

summed over the samples of the waveform and a value of 2 was used for p. There are several possibilities that can be tried. For segmented detectors, the comparison can be done by giving different weights to the segments depending on their distances from the hit segment. Various values of the exponent p can be tested. With higher statistics, one has to investigate, if it is possible to use a universal lower and higher limit of Δ^2 to select the pulses.

A. Appendix

The value of potential $\phi(\vec{r})$ at any point inside a detector of defined geometry is found by solving the Poisson equation

$$\nabla^2\phi(\vec{r}) = -\frac{\rho(\vec{r})}{\epsilon}, \quad (\text{A.1})$$

where $\rho(\vec{r}) = en(\vec{r})$, is the space charge density, e is the electron charge and $\epsilon = \epsilon_0\epsilon_r$ is the dielectric constant with $\epsilon_r = 16$ for a germanium detector. $n(\vec{r})$ is the impurity concentration defined as the difference between the density of donors N_D and the density of acceptors N_A .

After calculating the potential map in the detector, the electrostatic field for both the planar and coaxial geometry can then be found using

$$E(r) = -\nabla\phi(r) \quad (\text{A.2})$$

A.1. Electric field in a planar germanium detector

Since the potential is symmetric in y and z directions in the case of a planar detector, the Poisson equation reduces to

$$\frac{d^2\phi(x)}{dx^2} = -\frac{\rho}{\epsilon}. \quad (\text{A.3})$$

To solve this equation, one can use the ansatz

$$\phi(x) = ax^m + \alpha f(x), \quad (\text{A.4})$$

where $\alpha f(x)$ corresponds to the solution of the homogenous part of equation (A.3), such that

$$\frac{d^2f(x)}{dx^2} = 0 \quad (\text{A.5})$$

which is true for

$$f(x) = x \quad (\text{A.6})$$

Substituting the ansatz of $\phi(x)$ (equation A.4) in the Poisson equation (A.3) one gets

$$am(m-1)x^{m-2} = -\frac{\rho}{\epsilon}. \quad (\text{A.7})$$

For the above equation to be true for all the values of x , $m=2$ and

$$a = -\frac{\rho}{2\epsilon}. \quad (\text{A.8})$$

The general solution for the potential $\phi(x)$ is thus given by,

$$\phi(x) = -\frac{\rho}{2\epsilon}x^2 + \alpha x. \quad (\text{A.9})$$

One has to find α to fit to the boundary conditions. The boundary condition for an applied voltage V and depletion thickness d is,

$$\phi(d) - \phi(0) = V \quad (\text{A.10})$$

$$\Rightarrow \phi(d) - \phi(0) = -\frac{\rho}{2\epsilon}(d^2 - 0) + \alpha d \quad (\text{A.11})$$

$$\Rightarrow V = -\frac{\rho}{2\epsilon}d^2 + \alpha d \quad (\text{A.12})$$

$$\Rightarrow V + \frac{\rho}{2\epsilon}d^2 = \alpha d \quad (\text{A.13})$$

$$\Rightarrow \left[\frac{V + \frac{\rho}{2\epsilon}(d^2)}{d} \right] = \alpha \quad (\text{A.14})$$

The general solution for $\phi(x)$ satisfying the boundary conditions is

$$\phi(x) = -\frac{\rho}{2\epsilon}x^2 + \frac{V + \frac{\rho}{2\epsilon}(d^2)}{d}x. \quad (\text{A.15})$$

A.2. Electric field in a coaxial germanium detector

The radial part of the Poisson equation in cylindrical coordinates is given as

$$\frac{d^2\phi(r)}{dr^2} + \frac{1}{r} \frac{d\phi}{dr} = -\frac{\rho}{\epsilon}. \quad (\text{A.16})$$

This representation is under the assumption that $\phi(r)$ has no angular dependence and for the region where it is independent of the height z of the cylinder.

To solve this equation one can use the ansatz

$$\phi(r) = ar^m + \alpha f(r), \quad (\text{A.17})$$

where $\alpha f(r)$ corresponds to the solution of the homogenous part of equation (A.16)

$$\frac{d^2f(r)}{dr^2} + \frac{1}{r} \frac{df(r)}{dr} = 0 \quad (\text{A.18})$$

which is true for

$$\frac{df}{dr} = \frac{1}{r}. \quad (\text{A.19})$$

Substituting the ansatz of $\phi(r)$ (equation A.17) in the Poisson equation (A.16) one gets

$$am(m-1)r^{m-2} + amr^{m-2} = -\frac{\rho}{\epsilon} \quad (\text{A.20})$$

$$\Rightarrow am(m-1)r^{m-2} + amr^{m-2} + \frac{\rho}{\epsilon} = 0 \quad (\text{A.21})$$

$$\Rightarrow am^2r^{m-2} + \frac{\rho}{\epsilon} = 0 \quad (\text{A.22})$$

For this equation to be true for all values of r , $m=2$ and

$$a = -\frac{\rho}{4\epsilon}. \quad (\text{A.23})$$

The potential $\phi(r)$ is thus given by

$$\phi(r) = -\frac{\rho}{4\epsilon}r^2 + \alpha f(r). \quad (\text{A.24})$$

For a true coaxial detector of outer and inner radii r_2 and r_1 , the boundary condition is that the potential difference between these radii is equal to the applied potential V :

$$\phi(r_2) - \phi(r_1) = V \quad (\text{A.25})$$

$$\Rightarrow \phi(r_2) - \phi(r_1) = -\frac{\rho}{4\epsilon}(r_2^2 - r_1^2) + \alpha(f(r_2) - f(r_1)) \quad (\text{A.26})$$

$$\Rightarrow V = -\frac{\rho}{4\epsilon}(r_2^2 - r_1^2) + \alpha(f(r_2) - f(r_1)) \quad (\text{A.27})$$

$$\Rightarrow V + \frac{\rho}{4\epsilon}(r_2^2 - r_1^2) = \alpha(f(r_2) - f(r_1)) \quad (\text{A.28})$$

When applying the boundary conditions to the integral of equation (A.19), one gets

$$f(r_2) - f(r_1) = \ln \frac{r_2}{r_1}. \quad (\text{A.29})$$

Using this condition,

$$V + \frac{\rho}{4\epsilon}(r_2^2 - r_1^2) = \alpha \ln \frac{r_2}{r_1} \quad (\text{A.30})$$

$$\Rightarrow \left[\frac{V + \frac{\rho}{4\epsilon}(r_2^2 - r_1^2)}{\ln \frac{r_2}{r_1}} \right] = \alpha \quad (\text{A.31})$$

The general solution for $\phi(r)$ satisfying the boundary conditions is

$$\phi(r) = -\frac{\rho}{4\epsilon}r^2 + \left[\frac{V + \frac{\rho}{4\epsilon}(r_2^2 - r_1^2)}{\ln \frac{r_2}{r_1}} \right] \frac{1}{r}. \quad (\text{A.32})$$

Bibliography

- [1] H. J. Wollersheim et. al., “Rare ISotopes INvestigation at GSI (RISING) using gamma-ray spectroscopy at relativistic energies”, *Nuclear Instruments and Methods in Physics Research A*, Vol. 537, pp. 637, 2005.
- [2] G. de France, “Gamma-ray spectroscopy studies at GANIL: Status and perspectives”, *The European Physical Journal A*, Vol. 20, pp. 59, 2004.
- [3] M. Ishihara, “In-beam gamma-ray spectroscopy with RI beams on neutron-rich nuclei”, *Acta Physica Polonica B*, Vol. 40, 2009.
- [4] James L. Matteson, “Gamma-ray spectroscopy: Requirements and prospects”, *Adv. Space Res.*, Vol. 11, No.8, pp. (8)397(8)406, 1991.
- [5] A. J. Tavendale, “Semiconductor Lithium-Ion Drift Diodes as High-Resolution Gamma-Ray Pair Spectrometers”, *IEEE Transactions on Nuclear Science*, Vol. 11, pp. 191, 1964.
- [6] J. F. Sharpey-Schafer and J. Simpson, “Escape Suppressed Spectrometer Arrays: A Revolution in γ -ray Spectroscopy”, *Progress in Particle and Nuclear Physics*, Science Direct, Vol. 21, pp. 293, 1988.
- [7] I. Y. Lee et. al., “Developments in large gamma-ray detector arrays”, *Institute of Physics Publishing, Rep. Prog. Phys.*, Vol. 66, pp. 1095, 2003.
- [8] J. Simpson et. al., “The performance of a special geometry bismuth germanate escape suppressed spectrometer”, *Nuclear Instruments and Methods in Physics Research A*, Vol. 269, pp. 209, 1988.
- [9] I. Y. Lee, “The Gammasphere”, *Nuclear Physics A*, Vol. 520, pp. c641, 1990.
- [10] C. W. Beausang and J. Simpson, “Large arrays of escape suppressed spectrometers for nuclear structure experiments”, *Journal of Physics G: Nucl. Part. Phys.*, Vol. 22, pp. 527, 1996.
- [11] Z. Janout, S. Pospisil, M. Vobecky, “Observation of a Doppler broadening observation of the 4438 keV gamma-line of ^{12}C in processes $^{12}\text{C}(n,n'\gamma)^{12}\text{C}$ and $^9\text{Be}(\alpha,n\gamma)^{12}\text{C}$ ”, *Journal of Radioanalytical Chemistry*, Vol. 56, pp. 71, 1980.
- [12] J. Simpson, “The Euroball Spectrometer”, *Zeitschrift fuer Physik A*, Vol. 358, pp. 139, 1997.

-
- [13] F. Azaiez, "EXOAM: a γ -ray spectrometer for radioactive beams", Nuclear Physics A, Vol. 654, pp. 1003c, 1999.
- [14] C. E. Svensson, "TIGRESS: TRIUMF-ISAC gamma-ray escape-suppressed spectrometer", Journal of physics G: Nuclear and particle physics, Vol. 31, pp. S1663, 2005.
- [15] P. Reiter et. al., "The MINIBALL array", Nuclear Physics A, Vol. 701, pp. 209c, 2002.
- [16] I. Y. Lee et al., "GRETINA: A gamma ray energy tracking array", Nuclear Physics A, Vol. 520, pp. 255, Nov 2004.
- [17] J. Gerl and W. Korten, "AGATA technical proposal for an Advanced Gamma Tracking Array for the European Gamma Spectroscopy community", 2001.
- [18] F. Recchia, "In-beam test of the Agata prototype triple cluster", Acta Physica Polonica B, Vol. 38, 2007.
- [19] G. F. Knoll, "Radiation detection and measurement", John Wiley & sons, Third edition 1999.
- [20] A. Perez-Andujara, L. Pibidab et. al., "Performance of CdTe, HPGe and NaI(Tl) detectors for radioactivity measurements", Science Direct, Applied Radiation and Isotopes, Vol. 60, pp. 41, 2004.
- [21] HAMAMATSU, Multi-anode photomultiplier tube assembly, H3292 Series.
- [22] G. Ottaviani, C. Canali, F. Nava, and J. W. Mayer, J. Appl. Phys. 44, Vol. 6, pp. 2917, 1973.
- [23] M. Ali Omar and Lino Reggiani, "Drift velocity and diffusivity of hot carriers in germanium: MOdel calculations", Solid state electronics, Vol. 30, No. 12, pp. 1351, 1987.
- [24] M. B. Prince, "Drift Mobilities in Semiconductor. I. Germanium", Physical Review, Vol. 92, No. 3, 1953.
- [25] M. Descovich et. al., "The position response of a large volume segmented germanium detector", Nuclear Instruments and Methods in Physics Research A, Vol. 553, pp. 512, July 2005.
- [26] F. C. L Crespi, "A pulse shape analysis algorithm for segmented HPGe detectors", Acta Physica Polonica B, Vol. 38, 2007.
- [27] F. C. L Crespi et. al. , "Application of the Recursive Subtraction Pulse Shape Analysis algorithm to in-beam HPGe signals", Nuclear Instruments and Methods in Physics Research A, Vol. 604, pp. 604, 2009.
- [28] S. Tashenov and J. Gerl , "TANGO New Tracking Algorithm for Gamma-Rays", Nuclear Instruments and Methods in Physics Research A, Vol. 622, pp. 592, 2010.

- [29] A. Olariu et. al. ,“Pulse Shape Analysis for the location of the γ -Interactions in AGATA”, IEEE Transaction on Nuclear Science, Vol. 53, No. 3, June 2006.
- [30] D. Bazzacco, “The Advanced Gamma Ray Tracking Array AGATA”, Nuclear Physics A, Vol. 746, pp. 248c, 2004.
- [31] K. Vetter, “Gamma-ray tracking: Utilizing new concepts in the detection of gamma radiation”, European Physics Journal A, Vol. 15, pp. 265, 2002.
- [32] Anton Khaplanov, “Applications of pulse shape analysis techniques for segmented planar germanium detectors”, PhD thesis, KTH Stockholm, 2007.
- [33] Matthew Richard Dimmock et. al., “Characterisation results from an AGATA prototype detector”, IEEE Transactions on nuclear science, Vol. 56, No.3, June 2009.
- [34] F. C. L. Crespi et.al., “A novel technique for the characterization of a HPGe detector response based on pulse shape comparison” Nuclear Instruments and Methods in Physics Research A, Vol. 593, pp. 440, Aug 2008.
- [35] J. Gerl, “Gamma-ray imaging exploiting the Compton effect”, Nuclear Physics A, Vol. 752, pp. 688c, 2005.
- [36] J. Gerl, et al., “High-resolution gamma backscatter imaging for technical applications”, Nuclear Instruments and Methods in Physics Research A, Vol. 525, pp. 328, 2004.
- [37] C. J. Hailey et. al., “An inexpensive, hard x-ray imaging spectrometer for use in x-ray astronomy and atomic physics”, Nuclear Instruments and Methods in Physics Research A, Vol. 276, pp. 340, Mar. 1989
- [38] G. Tzanakos et. al., “Design considerations and construction of a small animal PET prototype”, Nuclear Instruments and Methods in Physics Research A, Vol. 569, pp. 235, Dec. 2006.
- [39] G. Tzanakos et. al., “Development of a small animal PET prototype”, IEEE Transactions on Nuclear Science, Vol. 3, pp. 21/53, 2000.
- [40] J. M. Benlloch et. al., “Scanner calibration of a small animal PET camera based on continuous LSO crystals and flat panel PSPMTs”, Nuclear Instruments and Methods in Physics Research A, Vol. 571, pp. 26, Nov. 2006.
- [41] V. V. Avdeichikov et. al., “Light output and energy resolution of CsI, YAG, GSO, BGO and LSO scintillators for light ions”, Nuclear Instruments and Methods in Physics Research A, Vol. 349, pp. 216, 1994.
- [42] HAMAMATSU, Multi-anode photomultiplier tube assembly, H8500 Series.
- [43] HAMAMATSU, Position-sensitive photomultiplier tubes with crossed wire anodes, R2486 Series.

-
- [44] A. J. Bird et. al., “Multi-channel readout of crossed-wire anode photomultipliers”, Nuclear Instruments and Methods in Physics Research A, Vol. 348, pp. 668, Sept. 1994.
- [45] C. Domingo-Pardo et. al. “A position sensitive γ -ray scintillator detector with enhanced resolution, linearity and field of view”, IEEE Transactions on Medical Imaging, Vol. 28, Dec 2009.
- [46] VikuitiTM Enhanced Specular Reflector (ESR), 3M, Optical Systems Division, 3m Center, Building 235-1E-54, St.paul, MN55144-1000, 1-800-553-9215.
- [47] Technical Information Manual MOD, N979 16 CHANNEL FAST AMPLIFIER Manual Rev.4, CAEN, October 2008, available at <http://www.caen.it/nuclear/index.php>.
- [48] Technical Information Manual MOD, N792 series 32/16 CH QDCs Manual Rev.15, CAEN, July 2008, available at <http://www.caen.it/nuclear/index.php>.
- [49] J. Hoffmann, N. Kurz, and M. Richter, TRIVA, VME Trigger Module, GSI Helmholtzzentrum für Schwerionenforschung GmbH, February 2007.
- [50] R. Barth et. al., GSI Multi-Branch System User Manual, GSI Helmholtzzentrum für Schwerionenforschung GmbH, January 2000, available at <https://www.win.gsi.de/daq/>.
- [51] J. Adamczewski et. al., The Go4 Analysis framework Reference Manual v4.0, GSI Helmholtzzentrum für Schwerionenforschung GmbH, February 2008, available at <http://www-linux.gsi.de/go4>
- [52] R. Brun and F. Rademakers, “ROOT- An object oriented data analysis framework” , Nuclear Instruments and Methods in Physics Research A, Vol. 389, pp. 21, Feb. 1997.
- [53] C. W. Lerche et. al., “Depth of interaction detection with enhanced position-sensitive proportional resistor network” , Nuclear Instruments and Methods in Physics Research A, Vol. 537, pp. 326, Jan. 2005.
- [54] C. W. Lerche et. al., “Depth of γ -ray interaction within continuous crystals from the width of its scintillation light-distribution”, IEEE Transactions on Nuclear Science, Vol. 52, No. 3, June 2005.
- [55] N. Goel, C. Domingo-Pardo, T. Engert, J. Gerl, I .Kojouharov and H. Schaffner, “Spatial calibration via imaging techniques of a novel scanning system for the pulse shape characterisation of position sensitive HPGe detectors”, Nuclear Instruments and Methods in Physics Research A, Jan 2011, doi:10.1016/j.nima.2011.01.146.
- [56] <http://www.canberra.com/>.
- [57] <http://www.ortec-online.com/>.
- [58] <http://www.struck.de/sis3301.htm>.

- [59] P. Medina et. al., “A simple method for the characterisation of HPGe detectors”, IEEE Instrumentation and Measurement Technology Conference, Vol 3, pp. 1828, 2004.
- [60] <http://mgs2005.in2p3.fr/download/MgsV5userguide.pdf>
- [61] A. Wiens et. al., “The AGATA triple cluster detector”, Nuclear Instruments and Methods in Physics Research A, Vol. 618, pp. 223, 2010
- [62] G. Pascovici et. al., “Low noise dual gain preamplifier with built in spectroscopic pulser for highly segmented high-purity germanium detectors” , WSEAS Transactions on Circuits and Systems, Vol. 7, no. 6, pp. 470, June 2008.
- [63] F. Zocca, A. Pullia, G. Pascovici, “Design and Optimization of Low-Noise Wide-Bandwidth Charge Preamplifiers for High Purity Germanium Detectors” , IEEE Transactions on Nuclear Science, Vol. 55, no. 2, pp. 695, 2008.
- [64] A. Pullia, F. Zocca, G. Pascovici, “An Advanced Preamplifier for Highly Segmented Germanium Detectors” , IEEE Transactions on Nuclear Science, Vol. 53 no. 5, pp. 2869, Oct. 2006.
- [65] <http://www.etps.co.uk/products/high-voltage-power-supply/productinfo.aspx?ProdID=NHQ>.
- [66] <http://www.struck.de/sis3302.htm>.
- [67] <http://www.struck.de/>
- [68] A. Georgiev, W. Gast, R.M Lieder, “An analog-to-digital conversion based on a moving window deconvolution”, IEEE transactions of Nuclear Science, Vol. 41, pp. 1116, 1994.
- [69] N. Goel, C. Domingo-Pardo, T. Engert, J. Gerl, I. Kojouharov, N. Pietralla and H. Schaffner, “Study of planar germanium detector response using the γ -ray imaging techniques”, submitted to NIM A, December 2010.
- [70] C. Domingo-Pardo et. al. “A novel method for the pulse-shape depiction of position sensitive semiconductor γ -ray detectors Part I: Characterization tests with a non-segmented planar detector”, submitted to NIM A, November 2010.
- [71] An International Accelerator Facility for Beams of Ions and Antiprotons, FAIR conceptual design report, <http://www.gsi.de/GSI-Future/cdr>, 2004.
- [72] Technical proposal for the SPIRAL 2 instrumentation, Dec. 2008, <http://pro.ganil-spiral2.eu/spiral2/instrumentation/desir/desir-technical-report>.
- [73] The scientific objectives of the SPIRAL 2 project, GANIL, Grand Accélérateur National d'Ions Lourds BP 55027 14076 Caen cedex 5 - France, June 2006.
- [74] G. Prete et. al. , “The SPES project: an ISOL facility for exotic beams”, Journal of Physics, Conference Series 168, 2009.

-
- [75] E. Farnea et. al. , “Conceptual design and Monte Carlo simulations of the AGATA array”, *Nuclear Instruments and Methods in Physics Research A*, Vol. 621, pp. 331-343, 2010.
- [76] C. Rossi Alvarez, “ The Advanced Gamma Ray Tracking Array AGATA”, *Brazilian Journal of Physics*, Vol. 34, 2004.
- [77] I. Y. Lee , “Gamma-ray tracking detectors: physics opportunities and status of GRETINA”, *Nuclear Physics A*, Vol. 834, pp. 743c, 2010.
- [78] A. Olariu et. al. , “Pulse Shape Analysis for the location of the γ -Interactions in AGATA”, *IEEE Transaction on Nuclear Science*, Vol. 53, No. 3, June 2006.
- [79] A. Lopez-Martens et. al. , “ γ -ray tracking algorithms: a comparison”, *Nuclear Instruments and Methods in Physics Research A*, Vol. 533, pp. 454, 2004.
- [80] Th. Kroll and Dino Bazzacco, “A genetic algorithm for the decomposition of multiple hit events in the γ -ray tracking detector MARS´´”, *Nuclear Instruments and Methods in Physics Research A*, Vol. 565, pp. 691, 2006.
- [81] Jianming Chen et.al., “Large size LSO and LYSO crystal scintillators for future high energy physics and nuclear physics experiments”, *Nuclear Instruments and Methods in Physics Research A*, Vol. 572, pp. 218, Nov. 2006.
- [82] Rocio A. Ramirez et. al., “A comparison of BGO, GSO, MLS, LGSO, LYSO and LSO scintillation materials for high-spatial-resolution animal PET detectors”, *IEEE Nuclear Science Symposium Conference Record*, 2005.
- [83] Matthew R. Dimmock et. al., “Characterisation results from an AGATA prototype detector”, *IEEE Transaction on Nuclear Science*, Vol. 56, No. 3, June 2009.
- [84] M. M. Fernandez et. al., “A flat-panel-based mini gamma camera for lymph nodes studies”, *Nuclear Instruments and Methods in Physics Research A*, Vol. 527, pp. 92, 2004.
- [85] B. Birkenbach, B. Bruyneel, et. al. “Determination of space charge distributions in highly segmented large volume HPGe detectors from capacitance-voltage measurements”, doi:10.1016/j.nima.2011.02.109, Reference. NIMA53413.

Erklärung zur Eigenständigkeit

Hiermit versichere ich die vorliegende Dissertation ohne Hilfe Dritter nur mit den angegebenen Quellen und Hilfsmitteln angefertigt zu haben. Alle Stellen, die aus Quellen entnommen wurden, sind als solche kenntlich gemacht. Diese Arbeit hat in gleicher oder ähnlicher Form noch keiner Prüfungsbehörde vorgelegen.

Darmstadt, April 10, 2011.

Namita Goel

Planckstrasse 1
Darmstadt, Germany 64291
☎ (+49) 1777 25 33 92
☎ (+49) 6159 71 1695
✉ n.goel@gsi.de

Namita Goel

Persönliche Daten

Geburtsdatum November 23, 1984
Geburtsort Delhi, Indien
Staatsangehörigkeit Indisch
Familienstand Ledig

Schulbildung

2000 **Central Board of Secondary Examination, Hans Raj Public School, Delhi, Indien.**
2002 **All India Senior School Certificate Examination (allg. Hochschulreife), D.A.V Public School, Delhi, Indien.**

Studium

2002-2005 **Bachelor in Physik an der Universität zu Delhi, Hans Raj College, Delhi, Indien.**
2005-2007 **Master in Experimenteller Kernphysik an der Universität zu Delhi, Institute of Physics and Astrophysics, Delhi, Indien.**

Berufliche Tätigkeiten

2007-2011 **Beschäftigung als Doktorandin im Bereich Experimentelle Kernstrukturphysik, GSI Helmholtzzentrum für Schwerionenforschung GmbH, Darmstadt, Germany.**

08.04.2011 Darmstadt